

Université de Neuchâtel
Institut de Physique



Photoemission of Switchable Mirrors and Quantum Wells

Travail de thèse présenté à l'Institut de Physique de l'Université de Neuchâtel
pour l'obtention du grade de Docteur ès Sciences

Christian Koitzsch

Neuchâtel, 2004

IMPRIMATUR POUR LA THESE

Photoemission of Switchable Mirrors and Quantum Wells

M. Christian KOITZSCH

UNIVERSITE DE NEUCHATEL

FACULTE DES SCIENCES

La Faculté des sciences de l'Université de
Neuchâtel, sur le rapport des membres du jury

MM. P. Aebi (directeur de thèse),
H. Beck, L. Schlapbach (Fribourg)
et J.A. Martin Gago (Madrid E)

autorise l'impression de la présente thèse.

Neuchâtel, le 16 août 2004

La doyenne:



Prof. M. Rahier

Science may be described as the art of systematic over-simplification.
(Karl Popper)

Contents

I	Introduction	7
1	Introduction to ARPES and DFT	8
1.1	The Y-Si system	9
1.2	Experimental Approach ARPES	10
1.3	Theoretical Approach DFT	16
1.4	3D Representation of Constant Energy Surfaces	21
1.5	The projected Band Structure	23
1.6	Susceptibility	24
2	Use of Angle-resolved Photoemission and Density Functional Theory for Surface Structural Analysis of YSi₂	28
2.1	Introduction	29
2.2	Experimental and Computational Details	31
2.3	Results	32
2.4	Discussion	35
2.5	Conclusion	36
3	The Transition between YSi₂ 1x1 and YSi_{1.7} $\sqrt{3}$ x $\sqrt{3}$ R30°	38
3.1	Introduction	39
3.2	Experimental and Computational Details	41
3.3	Experimental and Computational Results	41
3.3.1	X-Ray Photoelectron Diffraction and Multiple Scattering Calculations	41
3.3.2	UV Photoemission and DFT	43
3.4	Discussion	48
3.5	Conclusion	49

II	Electronic Structure of Rare Earth Hydrides	53
4	Introduction	54
4.1	General Remarks	54
4.2	Theoretical Models	55
4.3	This Work	61
5	Ab-initio Investigation of the Hydrogenation of Y	65
5.1	Introduction	66
5.2	Computational Details	67
5.3	Results	67
5.4	Discussion	69
5.5	Conclusion	70
6	Fermi Surface Topology of Rare Earth Dihydrides	74
6.1	Introduction	75
6.2	Experiment and Calculation Details	76
6.3	Experimental and Theoretical Results	78
6.3.1	General electronic properties of (Sc,Y,Gd,La) - dihydrides	78
6.3.2	Experimental Data and Calculation	81
6.4	Discussion	92
6.5	Conclusions	95
7	Electronic Structure of the YH₃ Phase from Angle-Resolved Photoemission	100
7.1	Introduction	101
7.2	Experimental Details	102
7.3	Results and discussion	104
7.4	Conclusion	109
III	Quantum Wells	112
8	Introduction to Quantum Well States	113
8.1	General Remarks	113
8.2	This Work	114
8.3	Experimental Details	114
8.4	Evolution of QWS with thickness	116

8.5	Results for normal emission	122
9	Photoemission of a Quantum Cavity with non-magnetic Spin Seperator	126
9.1	Introduction	127
9.2	Results	128
9.3	Discussion and Conclusion	133
IV	Appendix	139
10	Growth of thin Bi films on W(110)	140
10.1	Introduction	141
10.2	Experimental Details	141
10.3	Results and discussion	142
10.4	Conclusions	147
	Acknowledgements	153
	Curriculum vitae	155

Preface

This thesis is based on research carried out at the physics departments of the universities of Fribourg and Neuchâtel in Switzerland.

It consists of three main sections and an appendix. The sections comprise several publications, which stand completely on their own and can be read independently. This independence leads inevitably to some redundancy in terms of the description of experimental and computational details, the bibliography at the end of each chapter etc.

The first section gives an introduction to photoemission and Density Functional Theory exemplified for rare earth silicides. It shows, that photoemission results can be directly correlated to computational results from Density Functional Theory. The applicability of model electronic structure calculations serve hopefully as a motivation for experimentalists to perform their own model calculations to understand photoemission data from other systems. The availability of user-friendly electronic structure codes and the low costs of computational power enables us to do so. The degree of agreement even allows for the determination of surface structures by comparing theoretical results from different structural models to photoemission data. The application of this method made the extraction of a structural parameter for YSi_2 (1x1) possible, which had not been accessible with normal incidence low energy electron diffraction. The second part in this section deals with superstructure effects on the surface band structure. It is shown, that new periodicities do not only influence the dispersion of surface bands via backfolding but that the degree of surface localization might be influenced as well due to a backfolded substrate band structure.

The second section is dedicated to the electronic properties of rare earth hydrides or in a more popular term to switchable mirrors. These studies have been initiated by recent experimental developments, which allow the in-situ preparation of single crystalline hydride films and of course by the strong theoretical interest regarding the discrepancy between experimental results and theoretical predictions. An introduction into the field of electronic properties of switchable mirrors is given, which outlines how theory struggled to explain experimental findings. The second chapter in this section shows, how the theoretical band-

structure of yttrium is changed within the local density approximation upon hydrogenation. The third and the fourth chapter demonstrate, how theoretical results compare to experimental results for the metallic dihydride phase and the insulating trihydride phase. The description of rare earth hydrides poses a strong challenge for calculations involving the local density approximation. The comparison between experimental and theoretical results show a less convincing agreement compared to the rare earth silicides. However those effects can provide a direct fingerprint of electron correlations at play in these materials. In summary, we have established the role of the dihydride phase as a common electronic precursor phase for the insulating trihydride phase. The failure of the local density approximation to yield an insulating ground state for the trihydride phase is traced to a set of hydrogen derived flat bands, which are theoretically not adequately described.

The third section deals with quantum effects in nano-scale thin films. We succeeded in the preparation of very uniform Mg films on tungsten, which allow the direct observation of quantum-confined electronic states. A short introduction shows how these states derive from the familiar particle in the box model. A separate article reports on the influence of the confining barrier on the electronic properties of quantum well states. The spin-degree of freedom for the scattering of magnesium quantum-well states on W(110) is the main focus of this paper. The results show that a spin-splitting at a confining barrier is possible even without permanent magnetic moments due to relativistic effects. The described experiment shows for the first time the influence of the Rashba effect in metallic heteroepitaxial systems, which is very promising for the study of spin dependant scattering with photoemission.

In the Appendix we report on the growth of thin Bismuth films on W(110), where structural aspects of thin film growth are investigated with low energy electron diffraction and X-ray photoelectron diffraction. It exemplifies the structural work, which was the prerequisite for all electronic structure discussions and as such was the starting point for all UV photoemission studies in this thesis.

The articles included in this thesis are:

Use of Angle Resolved Photoemission and Density Functional Theory for Surface Structural Analysis of YSi₂

C. Koitzsch, C. Rogero, J. A. Martín-Gago, M. Bovet, M. G. Garnier and P. Aebi

Surf. Sci. **566-568**, 1047 (2004). 28

The Transition between YSi₂ 1x1 and YSi_{1.7} $\sqrt{3}$ x $\sqrt{3}$ R30°

C. Koitzsch, C. Rogero, L. Despont J. A. Martín-Gago, F. Clerc, C. Battaglia, M. G. Garnier and P. Aebi

to be submitted 38

Ab-initio Investigation of the Hydrogenation of Y

Christian Koitzsch, Michael Gunnar Garnier and Philipp Aebi

Physica Scripta, Vol. T109, 163 (2004). 65

Fermi Surface Topology of Rare Earth Dihydrides

C. Koitzsch, J. Hayoz, M. Bovet, F. Clerc, L. Despont, C. Ambrosch-Draxl, and P. Aebi

Phys. Rev. B **70**, 165114 (2004). 74

Electronic Structure of the YH₃ Phase from Angle-Resolved Photoemission

J. Hayoz, C. Koitzsch, M. Bovet, D. Naumović, L. Schlapbach and P. Aebi

Phys. Rev. Lett. **90**, 196804 (2003). 100

Photoemission of a Quantum Cavity with non-magnetic Spin Separator

C. Koitzsch, C. Battaglia, F. Clerc, L. Despont, G. Garnier and P. Aebi

accepted for publication in Phys. Rev. Lett.. 126

Growth of thin Bi films on W(110)

C. Koitzsch, M. Bovet, F. Clerc, D. Naumović, L. Schlapbach and P. Aebi

Surf. Science **527**, 51 (2003). 140

Part I

Introduction

Chapter 1

Introduction to ARPES and DFT

This thesis focuses on the electronic properties of materials, which were explored with angle resolved photoemission (ARPES) and Density Functional Theory (DFT). This chapter provides a short introduction to both methods. The introduction is exemplified for the model system YSi_x , which will be employed to discuss the experimental aspects of photoemission and the theoretical basis of DFT and their mutual correspondence. The basic notations and concepts will be introduced in this chapter and then applied to YSi_x . These same approaches are then used in later chapters to discuss the electronic properties of switchable mirrors and quantum well states.

The natural fingerprint of electronic phenomena in crystalline solids, e.g. in this thesis the hydrogen-induced metal-insulator transition and the formation of standing electron waves in quantum wells, is the k -resolved band structure or in short the $E(k)$ relation in the solid. The **experimental** technique to explore the occupied band structure in a k -resolved fashion is angle-resolved photoemission (ARPES). We will emphasize in this work the importance of extensive angle-scanning (equivalent to extensive k -space sampling, see below) to analyze the complex band structure of solids. The full-hemispherical approach of photoemission has been proven its success mainly in conjunction with high-temperature superconductivity, where it has been shown that an experimental restriction to high symmetry directions might lead to a restricted understanding of materials properties [1].

The attempt to explore experimentally the complex band structure of the

materials calls for an equivalent **theoretical** approach. The performed calculations are based on density functional theory, namely the Wien2k code [2]. The basic theory of DFT will be shortly presented in this introduction. The comparison of DFT results and experimental measurements requires the adaptation of DFT to full-hemispherical photoemission. In this respect, the experimental sampling of the Brillouin zone has to be taken into account for the computation of suitable DFT eigenvalues. Some helpful routines have been developed to improve the understanding of the complex band structure, e.g. three dimensional plotting and surface projections and integration along certain directions (see below).

1.1 The Y-Si system

The Y-Si system is employed as an example system in this introduction on certain aspects of DFT and ARPES for a variety of reasons.

First of all, single crystalline surfaces can be prepared in-situ in a controlled fashion. The preparation of well ordered thin films proceeds via in-situ electron beam deposition of Y onto a clean Si(111) 7x7 surface and a subsequent anneal to 550 °C. Depending on the initial amount of deposited Y, a sandwich-type AlB_2 structure of finite thickness is obtained via self-organized solid state diffusion at these elevated temperatures. The structure is schematically shown in Fig. 1.1 and consists of alternating hexagonal Y and Si planes resting on the Si(111) crystal substrate. The surface is silicon terminated and slightly buckled. An interesting effect is the formation of an ordered vacancy (V) network for coverages exceeding one monolayer. These vacancies occur in the graphitic unbuckled silicon sheets and are denoted with a V in Fig. 1.1.

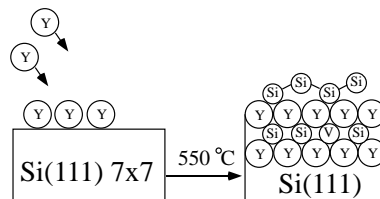


Figure 1.1: Schematic formation of a self-organized sandwich structure consisting of Y, Si and vacancies due to solid state diffusion at 550°C

The vacancy network gives rise to a $\sqrt{3} \times \sqrt{3}$ superstructure, which is indeed observed in diffraction experiments. In the following the reconstructed

thicker silicide will be denoted as **bulk silicide**, while the unreconstructed one monolayer thick structure will be referred to as **surface silicide**. The preparation of these layered structures is not restricted to Y-Si, but it was shown that Er, Ho and Gd behave in a similar way.

Beside the straightforward fabrication, the system offers additional advantages. It is a "true" surface system with well defined surface states and hence provides the possibility to study electronic states, which are localized at the surface and do not disperse in the perpendicular direction. Due to possible applications as a metallization layer in silicon device technology, the corresponding structures are well studied, which provides reference structure data from different techniques ranging from low energy electron diffraction [3] to X-ray and medium energy ion scattering[4] to local probe measurements [5]. The intermixing between Y and Si can be conveniently studied with X-ray photoelectron diffraction (XPD), which allows for an element-specific investigation of the atomic environment around Y atoms and is in this case particularly surface sensitive.

YSi_x surfaces offer a possibility to perform realistic band structure calculations. The limited number of metallization layers on the initial Si(111) surface provides the opportunity to perform realistic DFT calculations since the number of atoms in the interface vicinity can be treated with moderate computational effort in a super cell approach.

1.2 Experimental Approach ARPES

ARPES has been the subject of numerous review articles and books. We will emphasize here especially the peculiarities of the full hemispherical approach and its advantages.

On a superficial level, the experiment is based on the excitation of a bound electron by electromagnetic radiation. The photoelectron is promoted into an excited state in the conduction band and is able to overcome the surface barrier and is emitted into vacuum. There the photoelectron is analyzed in terms of emission angle and kinetic energy. The photoemission process defines the experimental setup and the principal experimental ingredients consist of a radiation source, a sample stage and an electron analyzer. However compared to early photoemission studies the experimental equipment has become increasingly sophisticated (Fig. 1.2). The preparation and measurement of clean and well-ordered surfaces is limited by residual gases, present in the measurement

setup. All experiments were therefore performed *in-situ* in a ultra-high vacuum environment with a base pressure of $p \approx 6 \cdot 10^{-11}$ mbar.

The light source is a monochromatized discharge lamp, which can be operated with different gases. For the presented measurements mainly H Ly α and He I α radiation are employed. The spectrometer is equipped with a 150 mm hemispherical analyzer, which determines the electron energy for a given sample-detector orientation. The energy and angle resolution of the detector with the employed settings is 50 meV and 2° , respectively.

The conservation of energy and momentum permits a translation of the measured $E_{kin}^{vac}(\theta^{vac})$ relation to the desired $E(\mathbf{k})_{solid}$ relation in the following way. Energy is conserved for the transition between the initial state $|\mathbf{k}_i\rangle$ and the final state $|\mathbf{k}_{final}\rangle$ via the incoming photon energy $h\nu$.

$$E_f(\mathbf{k}_{final}) = E_i(\mathbf{k}_i) + h\nu \quad (1.1)$$

The optical excitation in the crystal similarly conserves crystal momentum within a reciprocal lattice vector.

$$\mathbf{k}_{final} = \mathbf{k}_i + \mathbf{k}_{photon} + \mathbf{G}^{hkl} \quad (1.2)$$

For the employed photon energy range between 10.2 eV (H Ly α) and 21.2 eV (He I α), the momentum of the incoming photon can be neglected in equation (1.2), since in this case it is negligible with respect to the dimensions of a typical Brillouin zone. This, in turn leads to k-conserving, vertical transitions.

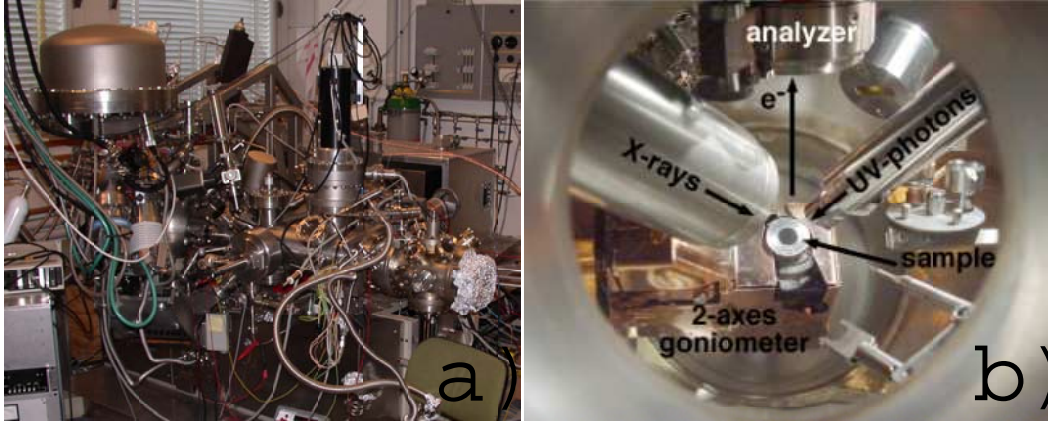


Figure 1.2: a) Photoelectron spectrometer at the University of Neuchâtel, in a typical laboratory atmosphere. b) Look into the analysis chamber.

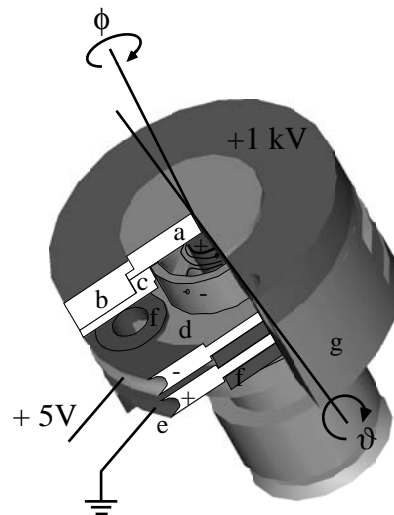


Figure 1.3: Sample holder with principal rotational axis. The sampleholder includes a setup for electron beam heating with (a) crystal (f) fixture plate and (c) support plate. The filament connectors (d),(e) are isolated from the main body (g) and from each other with ceramic spacers (f) and shaped such that the electron beam is directed towards the sample with minimal stray currents. Special care was taken to design most of the parts rotationally symmetric in order to simplify the mechanical work. With the displayed sampleholder it is possible to shortly heat single crystals to 2000°C with an acceptable pressure increase to $1 \cdot 10^{-9}$ mbar. The heating is achieved by accelerating (+600 V) electrons from a resistively heated Ta filament ($d=0.2$ mm)

The free electron final state (FEFS) assumption approximates for $|\mathbf{k}_{final}\rangle$ a free electron with the corresponding parabolic dispersion relation.

$$E_{final}(\mathbf{k}_{final}) = \frac{\hbar^2 \cdot \mathbf{k}_{final}^2}{2m} \quad (1.3)$$

The kinetic energy outside the crystal E_{kin}^{vac} is related to the energy of the final state $|\mathbf{k}_{final}\rangle$ via equation 1.4

$$E_{final}(\mathbf{k}_{final}) = E_{kin}^{vac} + V_0. \quad (1.4)$$

V_0 denotes the inner potential. The potential step at the surface leads to a refraction-like process of the photoelectron, while passing the surface barrier. The in-plane periodicity however results in the conservation of the parallel wave vector component k_{\parallel} . In consequence, it is the parallel wave vector component, which can be unambiguously determined in a photoemission experiment within a reciprocal lattice vector $\mathbf{G}_{\parallel}^{hkl}$ as the projection of the photo electron momentum onto the surface plane

$$k_{\parallel} = \frac{\sqrt{2m(h\nu - \phi - E_B)}}{\hbar} \cdot \sin(\theta_{vac}) \quad (1.5)$$

,where E_B is the binding energy with respect to the Fermi energy. The corresponding perpendicular wave vector component within the FEFS model is equivalently the projection of the outgoing photoelectron wave onto the surface normal.

$$k_{\perp} = \frac{\sqrt{2m(h\nu - \phi + V_0 - E_B)}}{\hbar} \cdot \cos(\theta) \quad (1.6)$$

The angular dependence of the photoemission signal can be determined by rotation of the sample with respect to the analyzer (and the lightsource), which stay fixed in space. The rotation stage is mounted on a standard x-y-z manipulator and offers two additional rotational degrees of freedom, which permit a scanning of the photoemission signal over the complete hemisphere above the sample. A sample holder with the rotational axis is shown in Fig. 1.3. The polar and azimuthal angles θ and ϕ can be varied between 0 and 90° and 0 and 360°, respectively. The crystal surface should terminate slightly above the sample holder fixtures in order not to perturb the photoemission signal at very high polar angles. The preceding equations already pointed to

the fact, that a change of θ or the measured kinetic energy leads to a change of the sampled k_{\perp} values, which means in practice, that the sampled k -values are not situated on a straight line in k -space for a polar scan. Instead they are found on a curved line. This k -space sampling has to be taken into account for bulk photoemission.

The situation is tremendously simplified, if two-dimensional systems are investigated, which do not exhibit a dispersion with k_{\perp} . This is the case for surface systems, where k_{\perp} is ill-defined. In this case equation (1.5) directly converts the measured $E(\theta)$ relation to $E(k_{\parallel})$. Electronic states confined in a thin overlayer or in the surface potential well are such two-dimensional systems.

Therefore the aforementioned layered silicide structures might be a case, where a test is feasible, whether experimental ARPES data can be compared to DFT results. For these overlayer structures, one might assume perfect two dimensionality and no dispersion perpendicular to the surface plane.

A typical measurement is shown in Fig. 1.4 for the aforementioned surface silicide (GdSi_2). The measured $E(\theta)$ distribution has already been mapped via equation 1.5 to $E(k_{\parallel})$ and to achieve a higher contrast, the second derivative of the momentum distribution curves is plotted. The measured band structure in this direction clearly shows two well-defined bands cutting the Fermi level around $\bar{\Gamma}$ and \bar{M} , with a small indirect energy overlap, which is indicative of a half metal. The almost filled band around $\bar{\Gamma}$ is called a hole pocket and the almost empty band around \bar{M} is denoted as electron pocket. The in-plane distribution of the two bands at E_F is shown on the right side of Fig.1.4. Such a measurement is called a Fermi surface map (FSM). It shows the photoemission signal in function of the polar and azimuthal angles θ and ϕ , which are shown in parallel projection. The outer ring corresponds to a polar emission angle of 90° .

Given band will yield a high intensity in these two-dimensional maps at some emission angle (θ, ϕ) , if the probed constant energy surface (e.g. the Fermi energy E_F) is cut at the respective k -point location. For $\text{YSi}(111)$ (1×1) the aforementioned electron pocket appears six times in the Brillouin zone, as it is expected for a hexagonal lattice, and it becomes clear that the shape of the electron pocket is actually an elongated ellipse in k -space, while the state at $\bar{\Gamma}$ is not circular either. One of the uncertainties of such a measurement is the change of the photoemission matrix element due to the rotation of the sample with respect to the light source. A change in contrast is therefore not necessarily related to band features. Complementary electron distribution

curves are a necessary check, that features in the constant energy maps are indeed related to the probed band structure.

An even more complete description can be obtained, if for each emission angle a complete spectrum is measured or alternatively a set of maps for different binding energies is obtained. A resulting data set is shown in Fig.1.5 for the YSi(111) (1x1) surface for the photoemission signal around the $\bar{\Gamma}$ point, where the first surface band, the hole pocket is sampled (cp. to 1.4) at different binding energies. The outer ring corresponds to a polar angle of 18° . A comparison to the corresponding band structure in Fig. 1.4 explains the observed behavior for higher binding energy maps, where the downwards dispersing band is sampled at increasingly higher wave vectors. This corresponds to a zoom-out

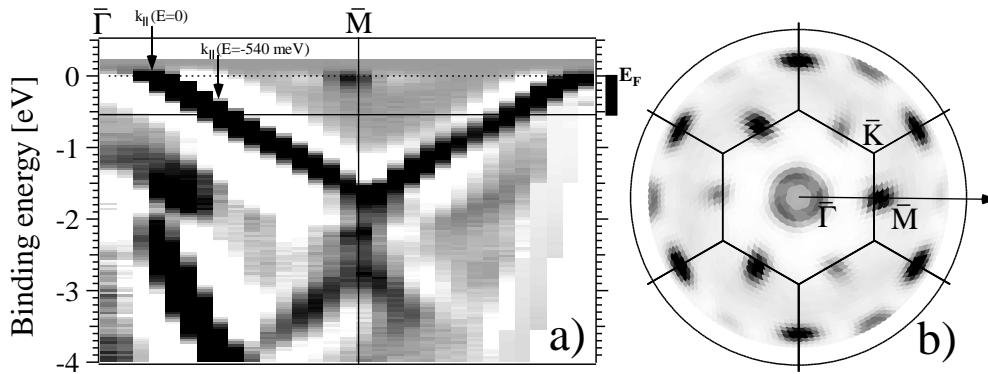


Figure 1.4: a) $E(k_{\parallel})$ along $\bar{\Gamma}\bar{M}$, shown is the second derivative of the momentum distribution curves. b) Fermi surface map in parallel projection and grey scale representation, large photoemission yield corresponds to black. The surface Brillouin zone is indicated together with the direction of the $E(k_{\parallel})$ measurement.

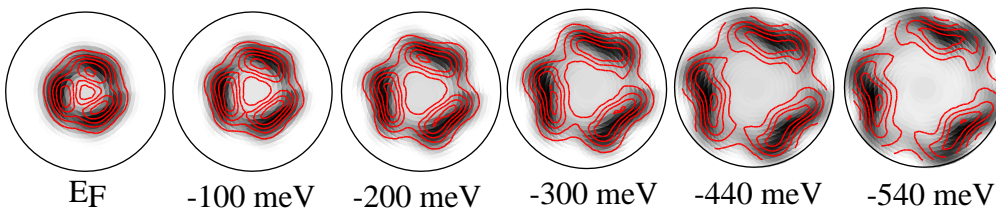


Figure 1.5: Constant energy surfaces for different binding energies between E_F and -540 meV for YSi₂ around $\bar{\Gamma}$ for a maximum polar angle θ of 18° (indicated with a circle). Constant intensity contour lines are shown for illustration purposes.

impression as we observe it in Fig. 1.5. The resulting constant energy cuts can in principle be fitted to a dispersion relation at any given k-point in the surface Brillouin zone. If the measured energies sample the complete bandwidth of a band, its dispersion is determined in the whole Brillouin zone. The price to be paid for such a measurement is a long measurement time if the data sets are obtained by sequential angle-scanning. An experimental constant energy surface consists of typically 2000 angular settings, which translates into approximately 1 hr measurement time per energy channel. Therefore these measurements are restricted to rather inert surfaces, where a sizable sample contamination does not occur in the measurement time. Additionally the sample symmetry itself can be exploited to reduce the size of the data sets. A measurement of the irreducible Brillouin zone can be unfolded with appropriate symmetry operations of the crystal lattice. An interesting experimental development are display-type analyzers, which can acquire the photoemission signal energy- and momentum resolved over a larger window and offer therefore the possibility to reduce the number of sequential scanned angular settings necessary to obtain a coverage of the full hemisphere [6].

The preceding section has shown, that ARPES measurements are related to the k-resolved band structure of solids. Angle-scanned data acquisition allows the sampling of extensive sections of the Brillouin zone. Nevertheless ARPES data are not easily comprehensible simply because the k-resolved band structure of real surfaces is not trivial either. In the following, we will discuss, how the k-resolved band structure can be theoretically determined for a given structure.

1.3 Theoretical Approach DFT

The following paragraph follows closely S. Cottenier's [7] excellent introduction into DFT and the family of (L)APW methods. He already pointed out, that in principle electronic structure calculations are a hopeless task if one considers the complexity of the problem. One needs to solve the time-independent Schrödinger equation

$$H |\Phi\rangle = E |\Phi\rangle \quad (1.7)$$

for an ensemble of M nuclei and N electrons, which are coupled via the long-range Coulomb interaction. The corresponding Hamiltonian is easily written

as the sum of the kinetic energies of nuclei and electrons H_{kin} plus the ion-ion, ion-electron and electron-electron Coulomb interaction H_{coul}

$$H_{kin} = -\hbar^2 \sum_{i=1}^N \frac{1}{2m_e} \nabla_i^2 - \hbar^2 \sum_{A=1}^M \frac{1}{2M_A} \nabla_A^2 \quad (1.8)$$

$$H_{coul} = -\frac{1}{4\pi\epsilon_0} \sum_{i,A} \frac{e^2 Z_A}{r_{iA}} + \frac{1}{8\pi\epsilon_0} \sum_{i \neq j} \frac{e^2}{r_{ij}} + \frac{1}{8\pi\epsilon_0} \sum_{A \neq B} \frac{e^2 Z_A Z_B}{R_{AB}} \quad (1.9)$$

The huge number of electrons and nuclei in a typical macroscopic solid leads to an intractable set of coupled differential equation, which require rather severe simplifications about the interactions between the particles in order to become accessible. First of all the ionic background lattice is assumed to be static and decoupled from the movement of electrons (adiabatic or Born-Oppenheimer approximation). This has the nice effect that the kinetic energy of the background ion lattice does not need to be considered and that the Coulomb field of the nuclei can be summarized via a now external potential V_{ext} . One obtains

$$H_{electronic} = T + V + V_{ext} \quad (1.10)$$

with T the kinetic energy and V the potential energy due to electron-electron interactions. Already the assumption of a static lattice is a severe limitation for compounds involving very light elements and in this sense hydrogen-containing compounds, e.g switchable mirrors, test the applicability of this assumption.

Still the remaining electronic problem is far too difficult to solve. At this point DFT emphasizes the correspondence between the ground state density $\rho(\mathbf{r})$, which can be approximated in some way (see below), and the ground state expectation value of any observable of the same many body system in the two Hohenberg-Kohn theorems.

$$\langle \Psi^* | O | \Psi \rangle = O[\rho] \quad (1.11)$$

for O being the Hamiltonian of the system, the second theorem states

$$E_{V_{ext}}[\rho] = \langle \Psi^* | T + V | \Psi \rangle + \langle \Psi^* | V_{ext} | \Psi \rangle = F_{HK}[\rho] + \int \rho(\mathbf{r}) V_{ext}(\mathbf{r}) d\mathbf{r} \quad (1.12)$$

, where $F_{HK}(\rho)$ is a universal expression for any many-electron system, which depends solely on the electron density, hence it is independent of e.g. the crystallographic structure. The implications of the two Hohenberg-Kohn Theorems are counter-intuitive since one does not expect that the correct ground state density $\rho(\mathbf{r})$ is equivalent of knowing the correct many-electron wave function $\Psi(r_1 \dots r_N)$, which both completely describe the system.

Despite its beauty, the Hohenberg-Kohn theorem does only state, that the functional $F_{HK}(\rho)$ exists, an explicit form though is not known. Nevertheless it provides in principle variational access to the problem, since the solution of the many-body Hamiltonian can be found by minimizing $F_{HK}(\rho)$ with respect to the density.

The practical way to obtain the ground state density is provided by the Kohn-Sham (KS) equations

$$H_{KS}\phi_i = e_i\phi_i \quad (1.13)$$

with the Kohn-Sham Hamiltonian being the Hartree term (non-interacting electron gas) extended by two "external" potentials, due to electron-electron interaction and electron-ion interactions.

$$H_{KS} = T_0[\rho] + V_H + V_{xc} + V_{ext} = -\nabla_i^2 + \int \frac{\rho(r)}{r} dr + V_{xc} + V_{ext} \quad (1.14)$$

with $V_{xc} = \frac{\delta V_{xc}[\rho]}{\delta[\rho]}$. These equations resemble familiar one-particle equations, which still do depend on the electron density $\rho[r]$ over the Hartree operator and the exchange correlation potential $V_{xc}(\rho)$. Therefore the KS equations have to be solved self-consistently until the solutions ϕ_i with their corresponding density $\rho(r) = \sum_{i=1}^N \phi_i^*(r) \cdot \phi_i(r)$ do not lead to a new charge density anymore if the procedure is repeated.

The resulting ground-state eigenfunctions ϕ_i of the Kohn-Sham equations are mathematical constructs which yield the "true" electron density. Nevertheless they stem from one-particle equations for an interacting ensemble and therefore the eigenfunctions are not true electron wavefunctions (which should depend on all other electrons as well) and the corresponding eigenvalues are in principle not electron energies as well.

So far we have cast the untractable many-body problem into an independent quasiparticle problem, where the complicated electron-electron interaction is viewed as a density dependant external potential acting on the Hartree

type electron gas. This treatment is still exact, though the exact form of the exchange-correlation functional is not known and has to be approximated, which in turn is not anymore exact.

The approximation for the exchange correlation functional is the local spin density approximation LSDA

$$E_{xc}^{LDA} = \int \rho(r) e_{xc}(\rho(r)) dr \quad (1.15)$$

with e_{xc} being known for a homogenous electron gas. In practice, each loop in the self-consistency cycle poses the task of constructing the exchange correlation functional for a given electron density $\rho(r)$. The exchange correlation energy for this density is approximated via integration of the exchange correlation energy for infinitesimal small density volumes of constant electron density. Each small volume contributes according to its electron density in LDA. For rather homogenous densities this seems a perfectly valid assumption. More corrugated electron densities are probably better approximated if the gradient to neighboring cells is evaluated as well. The corresponding exchange correlation functional is known as the generalized gradient approximation (GGA). In this work we use the parametrization of Perdew, Burke and Ernzerhof[8], which points to the fact, that there are different versions and parameterizations of GGA, which are sometimes not ab-initio but reflect some fitting process to experimental data.

The aforementioned Kohn-Sham orbitals are expanded in terms of given basis functions. It is exactly the choice of this basis set which determines the different flavors of DFT-LDA approaches. Wien2k utilizes an augmented plane wave basis set with additional local orbitals, therefore it is called an APW+lo code. Wien97 however utilizes a slightly different basis set of linearized augmented plane waves (LAPW) and correspondingly some older calculations have been performed with this basis set. The usual plane wave expansion is restricted to crystal regions with small variations of the charge density. For regions close to the nuclei an expansion in terms of atomic like functions is much more appropriate and efficient. Therefore, the crystal is fractionated into muffin tin regions centered around the specific atoms and interstitial regions in between. A mixed basis set is used

$$\phi_{\mathbf{k}+\mathbf{G}}(\mathbf{r}) = \frac{1}{\sqrt{\Omega}} e^{i(\mathbf{k}+\mathbf{G})r} \quad (1.16)$$

$$\phi_{\mathbf{k}+\mathbf{G}}(\mathbf{r}) = \sum_{lm} A_{lm}^{\alpha}(\mathbf{k} + \mathbf{G}) u_l^{\alpha}(\mathbf{r}, E) Y_{lm}(\mathbf{r}) \quad (1.17)$$

with planes waves in the interstitial region and spherical harmonics in the muffin tin region. The basis functions are matched with the requirement, that their value and slope has to coincide at the muffin tin border (boundary condition). The main advantage of this mixed basis set is the capability to describe valence and core electrons in the same framework, rendering the method a true "all-electron" method. A severe disadvantage is the energy dependence of the searched A_{lm}^{α} 's, which means, that we are not dealing with a linear eigenvalue problem anymore, hence the solution would be very time consuming. It can be shown, that the addition of local orbitals, which are completely restricted to the muffin tin, provides enough variational freedom to use the initial APW basis at some fixed energy.

The expansion of the Kohn-Sham orbital into the basis functions needs to be limited to a certain number of basis functions, determined by a cut-off parameter K_{max} . Furthermore the matching of spherical harmonics with plane waves on the surface of the muffin tin sphere requires a number of plane waves to accommodate the number of nodes for a given Y_{lm} at a given muffin tin radius r . These considerations are cast into a cut-off variable RK_{max} , which determines the matrix size and, over a cubic scaling!, the computation time. In this thesis largely different systems in terms of unit cell size, ranging from surface systems with 20 atoms, to bulk calculations involving only three to four atoms, were studied. The aim of the employed calculations was in most cases only the support of the photoemission data analysis. Extensive convergence studies would require an input parametrization with corresponding high computation times. In this sense RK_{max} values were chosen, which allowed the computation of a self consistency cycle in reasonable time, without too much changes in the band structure, when slightly increasing RK_{max} . It is to be pointed out, that the APW+lo methods is very rapidly converging in terms of matrix size, and that in general the band structure is less sensitive on the degree of convergence compared to e.g. the total energy.

The same relaxed approach in terms of convergence (namely using the band structure as the convergence condition) was utilized in terms of k-point sampling of the Brillouin zone during the scf cycle. Convergence is assumed, if a more dense k-point sampling in the irreducible BZ does not lead to a significantly different band structure.

Once the ground state charge density is known, the eigenvalues along the experimental k-point path can be computed and compared to the experiment. Such an experimental and theoretical dispersion plot is shown for the YSi_2 system in Fig.1.6. The eigenvalues are obtained similar to the self-consistency cycle, but this time eigenvalues are not computed on special grid points in the irreducible Brillouin zone but along high symmetry directions. The measurement is shown in the familiar gray scale, the theoretical eigenvalues are shown as black dotted lines. The obtained results for YSi_2 are very similar to the measurements for GdSi_2 , reflecting their similar atomic structure and their similar valence occupation.

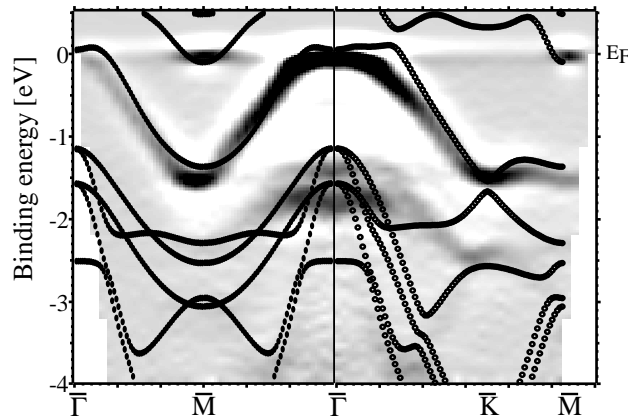


Figure 1.6: Experimental (grey scale) and theoretical dispersion for YSi_2 along high symmetry directions.

The two surface features, which cut E_F at $\bar{\Gamma}$ and \bar{M} are theoretically very well described and the degree of agreement is astonishing if one bears in mind the different assumptions of DFT/LDA and the fact that we are not performing photoemission calculations but merely ground-state calculations. Of course, in the presented framework the photoemission intensity is unaccounted for.

1.4 3D Representation of Constant Energy Surfaces

Full hemispherical experimental ARPES measurements yield data sets, which need to be compared to theoretical band structures on an equal footing. The

previous sections about ARPES have already shown, how the sampled parallel and perpendicular wave vector component changes during a scan over the sample hemisphere. In order to extract the eigenvalues for such an experimental k-point set, it seems appropriate to calculate the eigenvalues on a dense k-mesh, sampling the complete Brillouin zone, and to generate afterwards the desired two-dimensional cut.

Furthermore such a three-dimensional $E(\mathbf{k})$ set offers the possibility to generate "on the fly" the Fermi surface in three dimensions. Besides the general importance of the Fermi surface for various properties of solid materials, such a representation is particularly appropriate in connection with "nested" Fermi surfaces, where parallel sheets of the Fermi surface are looked for.

The main problem of these kinds of three-dimensional representations is the coarse sampling of the Brillouin zone with k-points, for which a diagonalization is performed and the eigenvalue spectrum is obtained. On the one hand a high k-point density is desired if two k-points with the same energy need to be resolved. This depends on the specific shape of the isoenergy surface. On the other hand a very coarse sampling of 25 k-points in k_x , k_y and k_z direction already yields $25^3=15625$ k-points. This has to be compared to the affordable time for one self consistency loop, which needs considerably less k-points (in the IBZ though) for a reasonable convergence.

The finite sampling of the Brillouin zone (BZ) does not permit a scatter plot of all wave vectors for a given energy, since the number of these wave vectors is not sufficient to extract the shape of the isoenergy surface. Instead a 3D interpolation scheme is needed in order to determine the corresponding k-space locations for some isoenergy taking into account the band dispersion itself [9]. Practically one determines the eigenvalues on an equidistant k-space grid in a large enough energy window, such that all valence states are computed. Wien2k indexes the eigenvalues starting from the bottom of the energy window. If no bands disperse through this lower boundary the numbering scheme remains consistent. The eigenvalues are then separated according to their band index and a data file is written for each index, which possesses eigenvalues at the desired binding energy. Fig. 1.7(left) shows the structure of the Wien2k output file with the eigenvalue spectrum for one k-point, namely the Γ point. The circled eigenvalue belongs to the band, which is slightly above the Fermi level in the center of the Brillouin zone. Mathematica routines are then used to compute a three-dimensional constant energy contourplot of the complete data set. The three-dimensional contour-plot is shown in Fig. 1.7 (right), which

confirms the two-dimensional nature of the material, since there is no dependence of the Fermi surface shape on the wave vectors in k_{\perp} direction, which is along ΓA .

The procedure does not take into account the symmetry of the crystal. This is basically due to the equidistant k space grid, which is the prerequisite for the three dimensional contour plot routines. An improved approach could only sample the irreducible Brillouin zone and generate equivalent k -points with the symmetry operations of the crystal space group. However this would require a new contourplot routine.

```

K= 0.00000 0.00000 0.00000 G
MATRIX SIZE 1003 WEIGHT= 2.00 PGR:
EIGENVALUES ARE:
-2.7700003 -1.3135461 -1.2926132 -1.2926125 -0.4767393
-0.4490245 -0.1127309 0.0362693 0.1910317 0.2609406
0.2609409 0.2920562 0.2920566 0.3805091 0.4501150
0.4501150 0.4925023 0.4961327 0.4961328 0.5148852
0.6010040 0.6147863 0.6147866 0.7046979 0.7046982
0.8006483 0.8273038 0.9553024 0.9553025 0.9592358
0.9861421 1.0022406 1.0022406 1.0401910 1.1300575
1.1300577 1.1448738 1.2477082 1.2477085 1.2684428

1.3761197 1.4415757 1.4415758 1.4420272
0 EIGENVALUES BELOW THE ENERGY -7.00000
*****

```

Filtering according to
band index (Igor Pro)

3D contourplot for given
energy for each band index
(Mathematica)

combination of 3D objects
(MathGl3D)

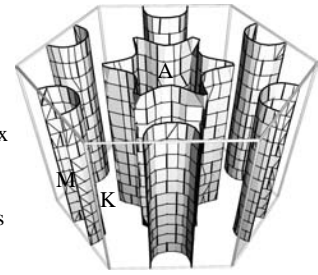


Figure 1.7: eigenvalue spectrum for the Γ point; three-dimensional Fermi surface generated from a cubic grid

1.5 The projected Band Structure

A surface projected band structure is particularly useful for the discussion of film substrate interactions. The complexity of DFT/LDA does not allow the modelling of large interfaces with a vast number of atoms. A coupling to the substrate bulk continuum can be discussed to some extent with the surface projected band structure from a suitable bulk calculation of the substrate. For the case of YSi_2 one is particularly interested if the aforementioned two states are actually surface states or maybe only resonant states, which couple to some extent to Si bulk states but have an increased amplitude at the surface. Therefore it is necessary to project the Si bulk continuum onto a Si(111) surface and to test if Si bulk states with the same k_{\parallel} as the surface states exist and hence might provide a coupling for $E(k_{\parallel \text{ bulk}}) = E(k_{\parallel \text{ surface}})$.

However for YSi_2 such a coupling for the two surface bands is not possible. An inspection of Fig. 1.8 shows that both features are situated in the band gap of the projected Si band structure. Therefore the two states are true surface states. Practically the $[111]$ projected band structure of Si is computed by calculating the eigenvalues on a two-dimensional grid (example Fig. 1.8b, which is spanned by the surface normal and the measurement direction). The k_{\perp} values are discarded and plots similar to Fig. 1.8a) can be obtained. The gray dots show the projected eigenvalues of Si bulk bands obtained by this procedure and confirm the location of both surface states at $\bar{\Gamma}$ and \bar{M} in the band gap of the projected bulk band structure.

1.6 Susceptibility

In connection with the three-dimensional representation of Fermi surfaces it has been mentioned, that parallel sheets of the Fermi surface are particularly interesting, since electronic states in the immediate vicinity of the Fermi level can determine macroscopic materials properties via low energy excitations and the formation of electron hole pairs. The wave vector dependant susceptibility quantifies the energy gain associated with the removal of Fermi surface parts due to a time independent potential caused by e.g. a phonon mode in the charge density wave case. The susceptibility is intimately related to the Lindhard response function

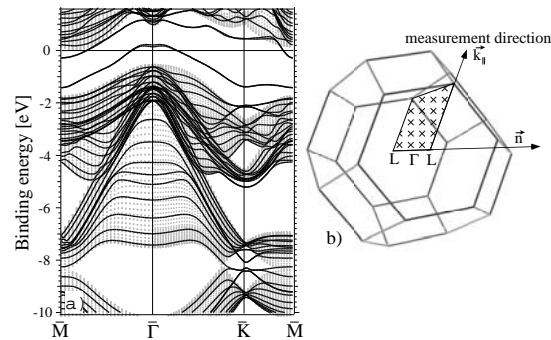


Figure 1.8: Theoretical dispersion for YSi_2 along high-symmetry directions. Shown in gray dots is the projected Si bulk band structure

$$\chi(\mathbf{q}) = \int \frac{f_k - f_{k+q}}{e_k - e_{k+q}} dk. \quad (1.18)$$

It is obvious, why the states at E_F contribute most. In the equation a zero energy difference between e_k and e_{k+q} leads to a divergence and hence to a peak in the response function. If the associated energy gain of all electron/hole pairs in the Brillouin zone exceeds the e.g. energy of the static lattice deformation with wavelength \mathbf{q} , the deformed lattice will be the ground state of the system. The vibrational properties of the lattice are not included at present in the computational framework. Nevertheless, it is possible to distinguish different perturbations \mathbf{q} in terms of their electronic response function. A convincing indication for an electronically driven phase transition is the detection of a gap at E_F at the given \mathbf{q} .

Computationally the response function has to be analyzed for a variety of \mathbf{q} 's in order to detect promising ordering vectors. The corresponding extensions to the standard Wien2k code were written in C. Ambrosch-Draxl's theory group [10]. Specifically this applies to the generation of suitable k-meshes in the IBZ, which is done in the subprogram "qgen" and the evaluation of the integral

$$\chi(E, \mathbf{q}) = \int \delta(\epsilon_{\mathbf{k}+\mathbf{q}} - \epsilon_{\mathbf{k}} - E) d\mathbf{k} \quad (1.19)$$

in the subprogram "coup". A commented input file for the two programs is shown for reference purposes. Fig. 1.9 a) shows the relevant input file for the k-space integration. It is possible to study the susceptibility for a specific band, however the indexing scheme has to remain consistent (as in the case of 3D Fermi surface generation) and therefore the eigenvalues have to be computed in a large energy window. Fig. 1.9 b) shows the input file to generate a suitable k-mesh. The parameters for sectioning the irreducible Brillouin zone are given in units of primitive reciprocal vectors (e.g. b_1, b_2, b_3 , where $b_1 = \frac{2\pi}{V} \cdot (a_1 \times a_2)$ with a_i primitive Bravais vectors) and not in conventional reciprocal lattice vectors. This is a major difference to the usual k vector definition in Wien2k, which is in units of conventional reciprocal lattice vectors. Fig. 1.9 c) shows a shell script, which automates the susceptibility calculation for a plane of q-vectors. With such a shell script, one can calculate the in-plane susceptibility, which can be directly related to Fermi surface maps in case of nesting. This has been used in particular in conjunction with the Fermi surface topology of rare earth dihydrides.

a)

```

FORM          internal label; for susceptibility use FORM (COUP/FORM)
1 16         minimum and maximum index of bands, which are considered
0.001 0.001 1.0  energy window (start, step, end) in Ry with respect to Fermi level

```

b)

```

41 41 41     determines the k-point mesh in kx, ky, kz of BZ
0 0 0       shift vector
1 0 0       q vector in internal coordinates of the BZ vectors (primitive k vectors)
-7.5 5.5    energy window in which eigenvalues are searched

```

c)

```

for ((i=0 ; k=42; i++ ))          two nested counter loops
do
  for ((j=0 ; k=42 ; j++ ))
  do
    let qx = $i+ $i                the q vectors have to be commensurate with
    let qy = $i+ $j                the k-mesh
    let qz = $i+ $j
    echo 41 41 41 > YH2.inq        writing of the appropriate *.inq
    echo 0 0 0 >> YH2.inq
    echo $qx $qy $qz >> YH2.inq
    echo -7.5 5.5 >> YH2.inq
    xqgen                          generating k-mesh
    xlpw2                           determination of occupancy (switch Fermi in *.in2)
    coup coup def                    integration in BZ
    echo nextqvector >> myoutputcoup
    echo $i$j0 >> myoutputcoup
    cat YH2.coup_LR >> myoutputcoup  collecting output in central data file
  done
done

```

Figure 1.9: Input files for susceptibility calculation a) *.inq b) *.incoup c) automated calculation on 41 x 41 grid

Bibliography

- [1] P. Aebi, J. Osterwalder, P. Schwaller, L. Schlapbach, M. Shimoda, T. Mochiku, and K. Kadowaki. *Phys. Rev. Lett.*, 72:2757, 1994.
- [2] P. Blaha, K. Schwarz, , G.K.H. Madsen, D. Kvasnicka, and J. Luitz. 2001. Wien2k, An Augmented Plane Wave + Local Orbitals Program for Calculating Crystal Properties (Karlheinz Schwarz, Tech. Univ. Wien, Austria) ISBN 3-9501031-1-2.
- [3] C. Rogero, C. Polop, L. Magaud, J. L. Sacedón, P. L. de Andrés, and J. A. Martín-Gago. *Phys. Rev. B*, 66:235421, 2002.
- [4] M. Lohmeier, W.J. Huisman, G. ter Horst, P.M. Zagwijn, E. Vlieg, C.L. Nicklin, and T. S. Turner. *Phys. Rev. B*, 54:2004, 1996.
- [5] J. A. MartínGago, J. M. GómezRodríguez, and J. Y. Veuillen. *Phys. Rev. B*, 55:5136, 1997.
- [6] T. Duetemeyer, C. Quitmann, M. Kitz, K. Doernemann, L. S. O. Johansson, and B. Reihl. *Rev. of Scientific Instruments*, 72:2638, 2001.
- [7] S. Cottenier. *Density Functional Theory and the family of (L)APW-methods*. 2002.
- [8] J.P. Perdew, S. Burke, and M. Ernzerhof. *Phys. Rev. Lett.*, 77:3865, 1996.
- [9] the three dimensional contourplot was generated with MathGl3D , an extension to Mathematica from Wolfram Research, to be found at <http://phong.informatik.uni-leipzig.de/kuska/mathgl3dv3/index.htm>.
- [10] Karl Franzens University, Graz, Austria, <http://physik.kfunigraz.ac.at/>.

Chapter 2

Use of Angle-resolved Photoemission and Density Functional Theory for Surface Structural Analysis of YSi₂

C. Koitzsch¹, C. Rogero², J. A. Martín-Gago², M. Bove¹, M. G. Garnier¹ and
P. Aebi¹

¹*Institut de Physique, Université de Neuchâtel, CH-2000 Neuchâtel,
Switzerland*

²*Instituto de Ciencia de Materiales de Madrid (CSIC), Cantoblanco, 28049
Madrid, Spain*

Surf. Sci. 566-568, 1047 (2004).

Abstract: The atomic structure of two-dimensional yttrium silicide epitaxially grown on Si(111) was investigated by means of density functional theory calculations and angle-resolved photoemission experiments. The obtained accuracy of the calculations allowed to discriminate different surface arrangements in a quantitative way

via comparing their theoretical band structure to the experimental result. Theoretically we find significant changes in the dispersion of a surface localized band upon varying the thickness of the topmost silicon bilayer. For a thickness of 0.4 \AA of the topmost silicon bilayer a strong asymmetry of the surface localized band with respect to $\bar{\Gamma}$ is found, while a thickness of 0.8 \AA yields a more symmetric dispersion of the band. By comparison with the experimental photoemission results, which show a rather symmetric band around $\bar{\Gamma}$, we can conclude that the topmost bilayer has a thickness of 0.8 \AA .

2.1 Introduction

For almost two decades the electronic structure of heavy rare earth (RE) silicides has attracted considerable interest due to potential applications in silicon based devices as a metallization layer. Very low Schottky Barrier heights on n-type Si(111)[1] were determined. On a fundamental level, the very initial stages of silicide formation, e.g. the formation of the first monolayer (ML) are of special interest. It has been shown for YSi_2 , GdSi_2 [2], ErSi_2 [3], DySi_2 [4] and HoSi_2 [5] that a solid state reaction at elevated temperatures takes place, which transforms the initially deposited monolayer into a structure commonly denoted as a two-dimensional (2D) surface silicide. Figure 2.1 shows a graphical representation of this model, together with the resulting surface Brillouin zone. An intermixing of the two initial constituents (metal, silicon) leads to a buckled silicon-bilayer terminated surface (Si1-Si2), with a planar, hexagonal metal atom sheet (Y) underneath. Below, the silicon bulk follows (Si3 to Si11), which is rotated 180° around the surface normal with respect to the orientation of the surface terminating bilayer (Si1-Si2). The depicted supercell (slab) is inversion symmetric in order to simplify electronic structure calculations (see below). A generalization of this structural model to other rare earths seems feasible.

A recent detailed structural investigation of the YSi_2 surface silicide based on low energy electron diffraction (LEED), demonstrated that this technique might show ambiguities due to the existence of different local R-factor minima [2]. In this case the ambiguities arose for a bilayer thickness (Si1-Si2) of 0.33 and 0.79 \AA , where the R factor was similarly low. By choosing different measurement geometries and with the support of *ab-initio* total energy calculations Rogero et. al. [2] were able to circumvent this problem and proposed a struc-

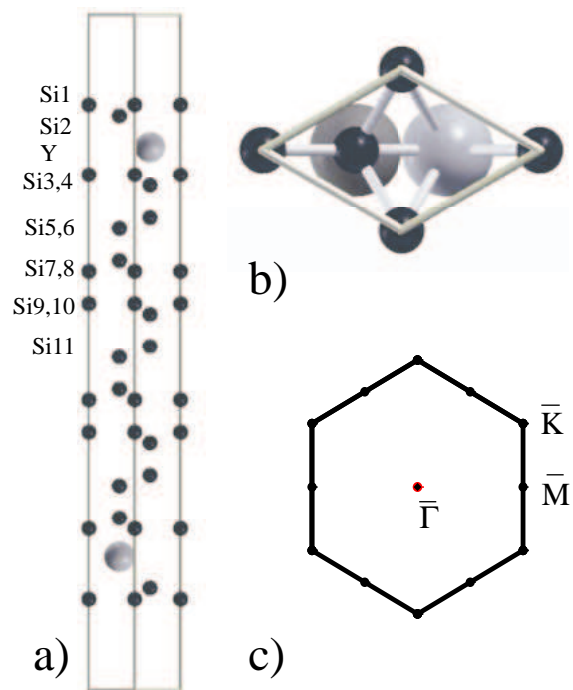


Figure 2.1: a) Side view of supercell. b) Top view of supercell. c) Hexagonal surface Brillouin zone of the same supercell.

tural model with bilayer thickness (Si1-Si2) of 0.8 Å. In this paper we present additional experimental evidence for the proposed model, by comparing the experimental electronic structure to theoretical results obtained for different bilayer thicknesses (Si1-Si2). For this purpose we calculated the band structure for surfaces, which deviated from the proposed structure and compare the calculations to photoemission results. We used structural parameters closely derived from the aforementioned LEED study with one free parameter, namely the uppermost bilayer thickness (Si1-Si2), where the ambiguities in LEED arose [2]. With regard to slight deviations for (Y-Si3) and (Si3-Si4) (see Table 1), it is assumed that they do not affect the employed surface state dispersion due to its localized nature (see below). The band structure was calculated *ab-initio* for different thicknesses of the topmost bilayer (Si1-Si2). The different parameters for structures "α" to "δ" and the LEED derived results are shown in Table 2.1.

2.2 Experimental and Computational Details

The YSi₂:Si(111) silicide was prepared by depositing 1 ML of Y on a clean Si(111)-7x7 reconstructed substrate at room temperature and a subsequent anneal to 400°C for 15 min. The pressure during evaporation and anneal was in the low 10⁻¹⁰ mbar range. The formation of the 2D yttrium silicide was confirmed by the presence of a sharp (1×1) LEED pattern with traces neither of

Table 2.1: Interplanar distances (in Å) between atomic planes along the (111) direction, derived from a LEED study [2] and the values employed in the present investigation. (Si1-Si2) is varied between 0.2 to 1.13 Å.

Atoms	LEED	DFT-LDA (Wien2k)			
		Slab "α"	Slab "β"	Slab "γ"	Slab "δ"
Si1-Si2	0.79	0.2	0.4	0.8	1.13
Si2-Y	1.85			1.88	
Y-Si3	2.08			2.04	
Si3-Si4	0.90			0.78	
Si4-Si5	2.35			2.35	
Si5-Si6	0.78			0.78	
LEED and this study both use a lateral lattice constant of 3.83 Å					

the (7×7) nor the $(\sqrt{3} \times \sqrt{3})$ reconstructions, which would have been indicative for the reconstructed thicker silicide (for more details see Ref.[2]).

The photoemission experiments were performed *in-situ* in a modified VG ESCALAB Mk II spectrometer with a base pressure lower than 10^{-10} mbar. All measurements were obtained using monochromatized He I radiation. The combined angular resolution of sample manipulator and energy analyzer was approximately 1° and the energy resolution 50 meV [6],[7].

For the electronic structure calculations the *ab-initio* code Wien2k [8] was used. A muffin tin radius for Y and Si of 2\AA and 2.1\AA , respectively, was assumed. The calculations are based on a slab as depicted in Fig. 2.1a,b). The hexagonal unit cell with 12 inequivalent atoms has an in-plane lattice constant of 3.83\AA , a value based on the aforementioned LEED study [2]. The lattice vector perpendicular to the surface has a length of 49.3\AA and includes a vacuum region of more than 12\AA . The unit cell is inversion symmetric and is comprised of an YSi_2 terminated top and bottom of the slab. In principle, such a construction is valid, if a standing wave formation due to the limited extension in z-direction is omitted. The supercell was constructed such that, the interaction of the two surfaces through the slab and through the vacuum region was minimized and the calculation was still feasible on a Linux PC with an Ahtlon processor. Self consistency was achieved, when the total energy change was less than 0.1 mRy in subsequent cycles.

2.3 Results

The resulting band structure for Slab " γ " with a bilayer thickness of 0.8\AA is plotted in Fig. 2.2a in an energy window from -10 eV to 1.6 eV along $\overline{M} \overline{\Gamma} \overline{K} \overline{M}$ in the surface Brillouin zone (Fig 2.1c). Additionally the surface projected band structure for Si(111) is shown in gray as an overlay.

Figure 2.2b) shows the corresponding site resolved density of states for the first 5 atoms (Si1-Si4, Y) and the bulk-like atom Si11. The computed band structure (Fig. 2.2a) is in nice agreement with the band structure calculated by Stauffer et. al. [9]. Special emphasis is drawn to band (A), which is in the fundamental gap of the underlying Si(111) substrate. It cuts the Fermi level at $k_F=0.14\text{\AA}^{-1}$ and follows an almost parabolic downward dispersion to \overline{M} and \overline{K} down to $E_B=-1.4$ eV. The band is then rather flat along $\overline{M} \overline{K}$. It is this flat region, which gives rise to a peak in the projected density of states shown in Fig. 2.2b) and labelled as A*. This peak in the projected density of

states can clearly be seen for Si1, Si2 and Y and then quickly fades out. This confirms its localized nature and together with its position in the fundamental silicon gap we identify band (A) as surface state. A discussion of the detailed nature of bonding in this material is forthcoming [10]. In the following we compare the calculated dispersion of band (A) to the experimental spectra. The measurement and the corresponding calculated surface state dispersions are shown in Fig. 2.3a). We restrict the discussion to the aforementioned band (A). We note a very nice overall agreement between the measured $E(k_{\parallel})$ and the predicted behaviour, as an almost fully occupied band with a parabolic downwards dispersion towards \bar{K} and \bar{M} and a rather flat region along $\bar{K} \bar{M}$. Moreover if one compares to the overlaid computed surface state dispersion, we note a maximum agreement between theory and measurement for slab "γ". For the other calculated geometries the agreement is less convincing. While the dispersion is less affected in the $\bar{\Gamma} \bar{M}$ direction, a clear deviation from the measurement is visible in the $\bar{\Gamma} \bar{K}$ direction. For structure "α" and "β" we observe a notable increase of the Fermi wave vector k_F , rendering the band structure more asymmetric around $\bar{\Gamma}$. The increase in k_F is approximately 50 percent with respect to the value for slab "γ", which is in disagreement to

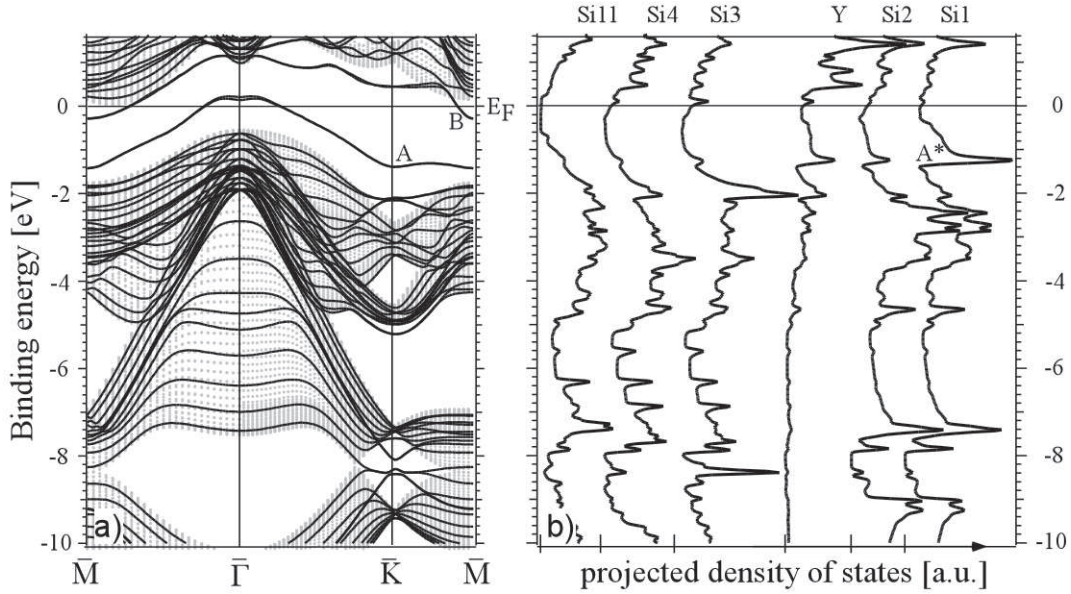


Figure 2.2: a) band structure for Slab "γ" and overlaid the surface projected band structure of Si(111). b) atomic site resolved density of states for slab "γ".

the measurement, where the region of high photoemission intensity is rather symmetric around $\bar{\Gamma}$. This can be clearly seen in the symmetrized spectra of Fig. 2.3b), where an increased intensity at E_F is signified by the merging of the two symmetric features at E_F into one peak. This is the case for spectra (1) and (1*), which are symmetric around $\bar{\Gamma}$. With regard to a distinction between structure "γ" and "δ", we note a better agreement at \bar{K} for the structure "γ"

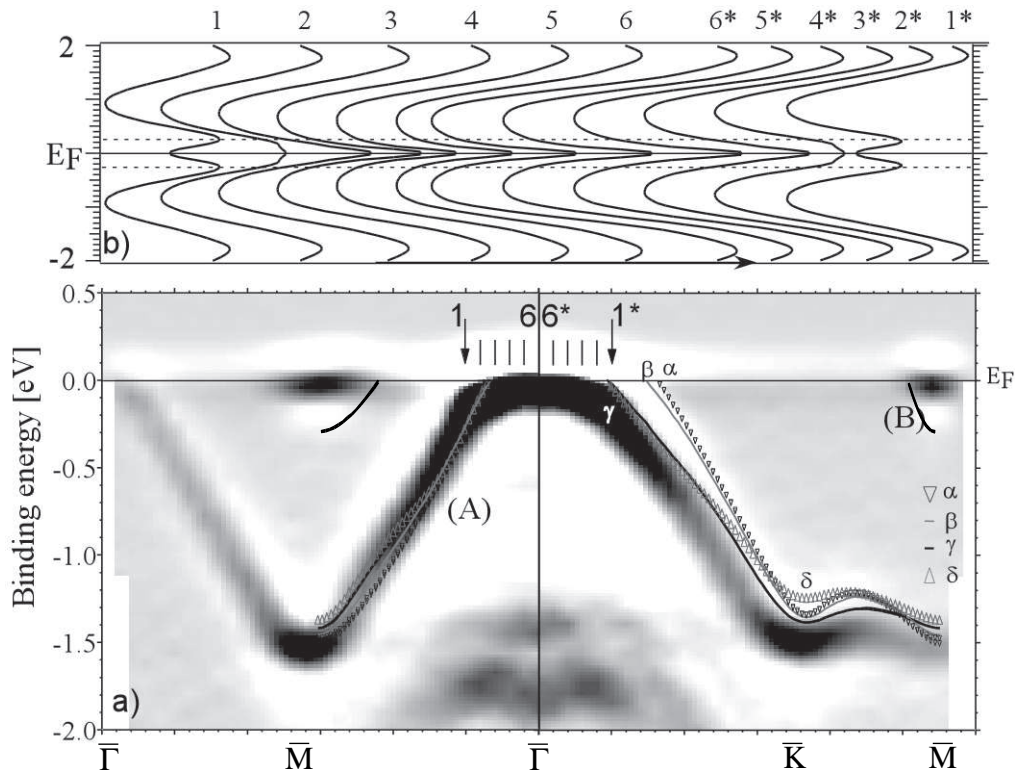


Figure 2.3: a) Experimental band structure (shown is the second derivative of the measured intensities in a grey scale, black corresponds to high intensity) for YSi_2 along $\bar{\Gamma} \bar{M} \bar{\Gamma} \bar{K} \bar{M}$ and overlaid surface state dispersion for different supercells (see text). b) Experimental symmetrized spectra for k_{\parallel} values around $\bar{\Gamma}$.

2.4 Discussion

The idea of discriminating different surface structural models via comparing their corresponding electronic band structure to experimental photoemission results is only feasible for certain cases. Reliable band structure calculations must be possible for the system in question and the band structure, namely specific localized bands, must be sensitive to the variation of structural parameters. In this sense the YSi_2 system presents an ideal case, since it gives rise to a surface state, which is localized largely in the topmost three layers. Furthermore the band dispersion is sensitive to the structural parameter that is to be optimized namely the bilayer thickness (Si1-Si2). This sensitivity allowed us to discriminate between the two different structures in question and it was possible to support the LEED derived bilayer thickness of 0.8 \AA with yet another technique, a photoemission guided DFT study. Whether one can do structural analysis with this technique depends on the required accuracy. Stauffer et. al. [9] have already shown for the same system that one can distinguish between vastly different surface arrangements via comparing experimental photoemission data to simple model calculations. The lack of computational accuracy though did not permit a quantitative analysis. Via using state-of-the-art ab-initio calculations we successfully discriminated between a bilayer thickness for the topmost silicon layer of $0.2, 0.4, 0.8$ and 1.13 \AA . It is very comforting that we used rather symmetry arguments for this distinction and not so much absolute band positions. This points to the advantages of full-hemispherical photoemission, where these symmetry elements can be immediately investigated. Systematic deficiencies of e.g. the LDA approximations with its underestimation of gap sizes and bandwidths, are rendered less important [11]. Despite the overall very good agreement between calculation and measurement in the case of YSi_2 , we note some deviations. The minimum for the surface band (A) is too high by approximately 200 meV and the position of the minimum of the second almost empty surface band around \bar{M} (band B in Fig. 2.2a and Fig. 2.3a) is calculated too low by about 150 meV . This is the case for slabs α to δ (only shown for slab γ in Fig. 2.3a). In this sense the LDA calculation yields a larger overlap between band (A) and (B) (Fig. 2.2) than is actually present, therefore e.g. the band overlap cannot be used in the same way to determine structural parameters, as we have demonstrated for the surface band.

2.5 Conclusion

We demonstrated the use of DFT and angle-resolved photoemission to distinguish between different structural models. Via such a comparison it was possible to support the previously suggested structure for YSi_2 [2] via photoemission spectroscopy. We observe significant changes in the dispersion of a surface localized band upon varying the thickness of the topmost silicon bilayer, ranging from 0.2 to 1.13 Å. We find a strong asymmetry with respect to $\bar{\Gamma}$ of the surface band for a thickness of 0.4 Å of the topmost silicon bilayer, while a thickness of 0.8 Å yields a dispersion of the band in much better agreement to the experiment.

Bibliography

- [1] T. Kalka and C. Preinesberger. *Phys. Rev. Lett.*, 82:1927, 1990.
- [2] C. Rogero, C. Polop, L. Magaud, J. L. Sacedón, P. L. de Andrés, and J. A. Martín-Gago. *Phys. Rev. B*, 66:235421, 2002.
- [3] P. Paki, U. Kafader, P. Wetzels, C. Pirri, J.C. Peruchetti, D. Bolmont, and G. Gewinner. *Phys. Rev. B*, 45:8490, 1992.
- [4] C. Bonet, D. J. Spence, and S. P. Tear. *Surf. Sci.*, 504:183, 2002.
- [5] H. Kitayama, S. P. Tear, D. J. Spence, and T. Urano. *Surf. Sci.*, 482:1481, 2001.
- [6] T. Pillo and P. Aebi. *J. of Electron Spectroscopy*, 66:075104, 199x.
- [7] D. Naumović, A. Stuck, T. Greber, J. Osterwalder, and L. Schlapbach. *Phys. Rev. B*, 47:7462, 1993.
- [8] P. Blaha, K. Schwarz, and J. Luitz. *Comput. Phys. Commun.*, 59:399, 1990. Improved and updated UNIX version of the original copyrighted WIEN code by P. Blaha, K. Schwarz and P. Sorantin.
- [9] L. Stauffer, A. Mharchi, C. Pirri, P. Wetzels, D. Bolmont, G. Gewinner, and C. Minot. *Phys. Rev. B*, 47:10 555, 1993.
- [10] C. Rogero. to be published.

-
- [11] J. Hayoz, C. Koitzsch, M. Bovet, D. Naumović, L. Schlapbach, and P. Aebi. *Phys. Rev. Lett.*, 90:196804–1, 2003.

Chapter 3

The Transition between YSi_2 1×1 and $\text{YSi}_{1.7}$ $\sqrt{3} \times \sqrt{3}$ $R30^\circ$

C. Koitzsch¹, C. Rogero², L. Despont J. A. Martín-Gago², F. Clerc, C. Battaglia, M. G. Garnier¹ and P. Aebi¹

¹*Institut de Physique, Université de Neuchâtel, CH-2000 Neuchâtel,*

Switzerland

²*Instituto de Ciencia de Materiales de Madrid (CSIC), Cantoblanco, 28049 Madrid, Spain*

to be submitted for publication

Abstract: We report angle-resolved photoemission measurements of Y silicide thin films. X-ray photoelectron diffraction data are presented, which provide strong support of previously proposed structural models. UV photoemission data are analyzed in terms of backfolding of surface bands during the structural transition from YSi_2 1×1 to $\text{YSi}_{1.7}$ $\sqrt{3} \times \sqrt{3}$ $R30^\circ$. We find clear indications for the $\sqrt{3} \times \sqrt{3}$ $R30^\circ$ reconstruction in the valence band electronic structure of $\text{YSi}_{1.7}$. However, the observed valence band might indicate an influence of the underlying Si(111) substrate as well. It is proposed that the surface state - substrate interaction is mediated by

the reconstructed $\text{YSi}_{1.7}$ spacer layer via Umklapp scattering. For the unreconstructed YSi_2 (1x1) surface system no scattering vectors are provided by the lattice and the observed bands are true surface states, which exist in the electronic gap of the Si(111) substrate.

3.1 Introduction

Rare earth silicides received increased interest due to potential applications as metalization materials for silicon device applications. The surface electronic structure during the interface formation, namely as a function of the overlayer thickness, is consequently a key point for these materials. Interestingly, a structural phase transition occurs for overlayer thicknesses exceeding one monolayer (ML) with the change from 1x1 to a $\sqrt{3} \times \sqrt{3}$ R30° periodicity for thicker films. It has been shown that the new periodicity is related to the formation of an ordered vacancy network in the silicon planes (see e.g. [1] and ref. therein). It was claimed that the very surface atomic structure in the reconstructed phase is largely unaltered with respect to the unreconstructed phase. A summary of the proposed crystallographic model is given in Fig. 3.1a), a more refined model including lateral relaxations will be published elsewhere [2].

The surface silicide consists of a buried Y layer (Y 1) with a buckled Si bilayer (Si 1 and Si 2) on top. The hexagonal Y layer rests on the silicon bulk crystal (not shown) such that Y atoms are in a T4 position with respect to the underlying substrate. The YSi_2 1x1 unit cell is shown dark gray shaded. For details on the structure, especially regarding lateral relaxations, the reader is referred to [3].

The reconstructed silicide is formed if the initial amount of Y exceeds a coverage of 1 ML. The respective positions of Si1, Si2 and Y1 are assumed to be largely unaltered. The underlying crystal is derived from the bulk YSi structure, which is of the AlB_2 type. For the 2 ML case, this translates into an additional graphite-like Si sheet Si3 and a second planar yttrium sheet (Y2) underneath, which is followed by bulk Si (not shown). It is believed that an ordered array of vacancies is established in the Si3 layer with a $\sqrt{3} \times \sqrt{3}$ R30° periodicity. A possible vacancy array is indicated in Fig. 3.1a) with rectangular markers and the corresponding $\sqrt{3} \times \sqrt{3}$ R30° unit cell is gray shaded. Please note that there are no indications of these vacancies in the topmost silicon bilayer (Si1 and Si2) [4].

Consequently, due to the largely unaltered surface atomic structure, the

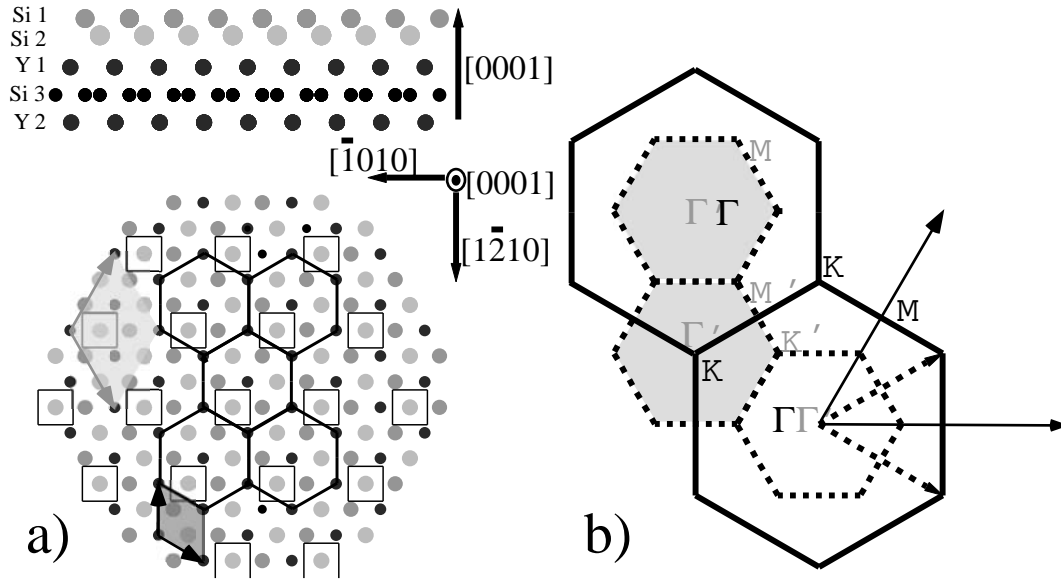


Figure 3.1: a) structural model of yttrium silicide b) Brillouin zones of YSi_2 1×1 (black lines) and $YSi_{1.7}$ $\sqrt{3} \times \sqrt{3}$ $R30^\circ$ (dashed lines)

surface electronic structure of the reconstructed phase is believed to be dominated by umklapp scattering effects [5]. The surface silicide supports two surface states, which should be backfolded into the new smaller $\sqrt{3} \times \sqrt{3}$ $R30^\circ$ Brillouin zone (see Fig. 3.1b) of the reconstructed phase.

Such Umklapp scattering is of great interest for the detection of various ordering phenomena with angle-resolved photoemission. It has been shown by Voit[6], that the detection of shadow bands might be seriously hampered by an unfavorable redistribution of spectral weight, which tends to emphasize the unperturbed bands. We concentrate on three film thicknesses, the unreconstructed surface silicide (YSi_2) and a 2 ML respectively 10 ML thick sample $YSi_{1.7}$, which already exhibits superstructure traces. Angle-resolved photoemission measurements with X-rays (X-ray photoelectron diffraction, XPD) and UV photons (angle resolved UV photoemission, ARUPS) are presented. The measurements are discussed in terms of model calculations obtained via multiple scattering calculations for XPD analysis and density functional theory (DFT) for ARUPS data. The 2 ML thick sample is used to investigate the atomic structure with XPD, since the limited thickness is beneficial for the analysis. ARUPS is however performed for the 10 ML sample, as these thicker films are

more representative of the bulk, since there are indications of a doubled or even quadrupled unit cell in [0001] direction[1].

3.2 Experimental and Computational Details

The experimental details of the sample preparation and the specifications of the employed modified VG Mk II photoemission apparatus have been already outlined in publications dedicated to the understanding of the surface silicide [7][8]. In this investigation the scope is extended from the ultra-thin 1x1 surface silicide YSi₂ to very thin reconstructed silicides.

Full hemispherical measurements of the Y 3p photoemission intensity ($E_{kinetic}=1440.3$ eV), excited with Si K α are presented. These measurements are sensitive to the local environment around the specific scatterer, namely Y atoms [9] and can be understood via scattering calculations based on model clusters. In this investigation the scattering calculations were performed with the multiple scattering code EDAC [10][11].

The electronic structure calculations are based on DFT in the framework of the generalized gradient approximation (GGA). The APW+lo code Wien2k [12] was employed.

3.3 Experimental and Computational Results

3.3.1 X-Ray Photoelectron Diffraction and Multiple Scattering Calculations

The experimental XPD results and their respective simulation counterparts are summarized in Fig. 3.2. The angular distribution of the Y 3p core level emission is shown in stereographic projection in a linear gray scale, where white corresponds to strong emission signal. Fig. 3.2 shows the experimental XPD results for YSi₂ 1x1 (Fig. 3.2a) and 2ML YSi_{1.7} $\sqrt{3} \times \sqrt{3}$ R30° Fig. (3.2b). On the right hand side (Fig. 3.2c,d) the respective multiple scattering simulations are shown. The analysis is based on the cluster model (shown in Fig. 3.2e). Open dots, which are overlaid onto the diffraction maps, originate from a stereographic projection of the relevant forward focusing directions with respect to the two different Y layers (Y1 and Y2 in Fig. 3.2e). The corresponding angles are shown in Fig. 3.2e) in gray for emission from Y1 and in black for

emission from Y2. In order not to cover the complete measurements, only one third of the hemisphere for the stereographic projection of the cluster is shown (Fig. 3.2a-d). Furthermore in order to simplify the discussion, the $\phi=0$ line is shown for all polar angles. This allows an immediate comparison between measurement, simulation and cluster model for this line. The size of the dots for the projection scales inversely with the emitter-scatterer distance, which emphasizes nearest neighbor scattering. The overall agreement between experimental data (Fig. 3.2a,b) and the simulation (Fig. 3.2c,d) is convincing. In the following we will discuss some details.

For YSi_2 1x1 (Fig. 3.2a, c and e) a threefold pattern is obtained. The lack of high emission intensity in normal emission is consistent with the structure model, which places Y 1 in a hollow position underneath a buckled Si hexagon (Si 1 and Si2). The threefold pattern is the direct fingerprint of this buckling. The position of feature 1 (Fig. 3.2a,c) can be directly understood in terms of scattering at the Si 1 layer (Fig. 3.2e, 42.1°). The respective expected forward focusing peak for nearest neighbor scattering between Y1 and Si 1 is shown at 42.1° with an open marker (feature 1 in Fig. 3.2a,c), which is experimentally well confirmed. On the other hand the second primary feature (feature 2 in Fig. 3.2a,c) is the result of interference of nearest neighbor and next-nearest neighbor scattering. The expected forward focusing maxima at 50.1° and 61.0° (Fig. 3.2e) are not reproduced in the experimental data nor the calculation. Instead of maxima at the respective positions (open dots in Fig. 3.2a,c), a rather elongated ellipse is observed (feature 2 in Fig. 3.2a,c). The shape of this ellipse depends crucially on the Debye temperature. We find a strong deviation from bulk silicon values ($\Theta_{Debye}(\text{Si 1, Si 2})=456$ K compared to $\Theta_{Debye}(\text{Si}_{bulk})=645$ K) in agreement to a previous LEED study [3]. Unfortunately the employed multiple scattering code does not yet allow for a layer-resolved definition of the Debye temperature, such that one cannot distinguish between Si 1 and Si 2 vibrations. Another interesting diffraction effect is the occurrence of ring-like features (white line in Fig. 3.2a, c). These rings originate from interference between scattered and unscattered waves.[13]

The diffraction maps for the 2 ML thick $\text{YSi}_{1.7}$ show more features, as it is expected for an emission signal originating deeper in the crystal. Expected forward focusing maxima along the $[\bar{1}0-10]$ direction are labeled in Fig. 3.2e) in gray for Y1 related features and black for Y2 related features) and shown in corresponding open dots in Fig. 3.2b) and d). The overall agreement between experimental data and numerical results is again quite convincing. First of all,

a maximum at the center of the diffractogram is apparent, which can be readily understood as Y2-Y1 forward focusing (long arrow in Fig. 3.2e). Additional maxima close to the center are observed in the diffractograms (Fig. 3.2b and d), which are again Y2 related and are caused by scattering at the respective buckled Si toplayer (Si 1 and 2 in Fig. 3.2e). The corresponding features appear almost hexagonal, since for Y2 centered emission the buckling translates into a smaller polar angle difference compared to emission from Y1 sites (20.7° and 19.0° compared to 50.1° and 42.1°). Another expected feature is Y2 related scattering at the hexagonal graphite-like layer (Si3). A 6-fold symmetric feature is expected at 48.7° . This feature is masked by the primary features due to Y1-Si1,Si2 scattering. Measurements on thicker films (not shown) however confirm the expected 6-fold emission patterns for bulk coordinated Y sites due to the planar graphitic sheet structure of the compound. The proposed vacancy structure in the silicon sheets is not observable with the technique since the signal is integrated over a large area (mm^2) and consequently averaged out for different domains.

3.3.2 UV Photoemission and DFT

The main ARPES results are summarized in Fig. 3.3, together with appropriate DFT calculations (see below). The experimental results were obtained from YSi_2 1×1 (Fig. 3.3a,b and c) and from a 10 ML thick, $\sqrt{3} \times \sqrt{3}$ R30° $YSi_{1.7}$ film (Fig. 3.3e,f and g). Fermi surface maps (Fig. 3.3a,e) together with dispersion plots along $\bar{\Gamma} \bar{K} \bar{M}$ (Fig. 3.3b,f) and along $\bar{\Gamma} \bar{M} \bar{\Gamma}$ (Fig. 3.3c,g) are shown. The two directions, for which band mapping experiments were performed, are indicated in the Fermi surface maps as gray arrows. The results for YSi_2 are mainly reported here as a reference. The main focus lies on a discussion of reconstruction induced changes, which should be visible in the comparison between YSi_2 1×1 and $YSi_{1.7}$ $\sqrt{3} \times \sqrt{3}$ R30°.

The electronic structure of YSi_2 1×1 has been discussed in detail in a recent publication, the major points are given here for ease of argumentation again[7]. The Fermi surface of YSi_2 arises due to contributions of two bands, labeled as features one and two in Fig. 3.3a). An almost filled band (feature 1) gives rise to emission centered at $\bar{\Gamma}$ and an almost empty band (feature 2) cuts the Fermi energy close to \bar{M} . The occupation and bandwidth of the two bands were determined via measuring the dispersion relation in terms of k_{\parallel} along $\bar{\Gamma} \bar{K} \bar{M}$ (Fig. 3.3b) and $\bar{\Gamma} \bar{M} \bar{\Gamma}$ (Fig. 3.3c). Feature one exhibits a nearly parabolic

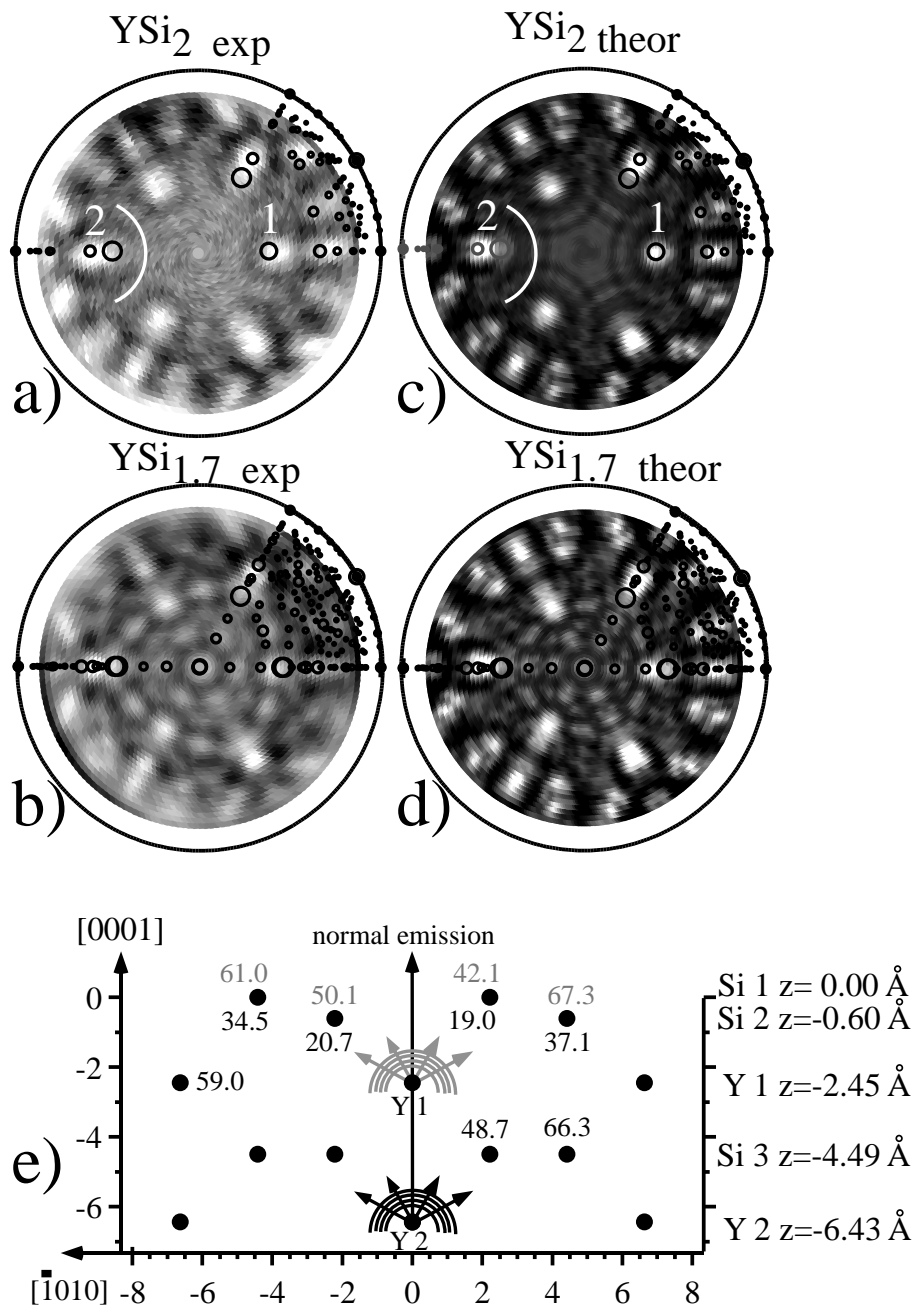


Figure 3.2: Photoelectron diffraction maps for YSi₂ 1x1 and YSi_{1.7} $\sqrt{3} \times \sqrt{3}$ R30°. a) Experimental XPD YSi₂ 1x1. b) Experimental XPD YSi_{1.7} $\sqrt{3} \times \sqrt{3}$ R30°. c) Simulated diffractogram YSi₂ 1x1. d) Simulated diffractogram YSi_{1.7} $\sqrt{3} \times \sqrt{3}$ R30°. e) Employed cluster model.

downwards dispersion towards \overline{M} and \overline{K} , where a binding energy of ≈ -1.5 eV is reached (Fig. 3.3b,c). The dispersion between \overline{K} and \overline{M} is rather flat. The band cuts the Fermi level at $\approx 0.2 \text{ \AA}^{-1}$. Feature two has an elliptical shape around \overline{M} , with a binding energy of ≈ -0.3 eV, rendering YSi₂ a half metal due to a small indirect overlap between feature one and two.

It has been shown previously that both bands are surface localized states. These surface states are very well reproduced by DFT calculations[7][8]. The corresponding theoretical dispersion relation for the electron and hole pocket is shown in Fig. 3.3b) and c) as open (filled) dots for the electron (hole) pocket with a convincing agreement to the experimental data. The theoretical band minimum at \overline{M} is ≈ 200 meV too low, which is reminiscent of the well known band gap problem within the local density approximation. The same calculation is shown in Fig. 3.3d) for $\overline{\Gamma} \overline{K} \overline{M}$, but in a Brillouin zone adapted to a $\sqrt{3} \times \sqrt{3}$ R30° reconstruction (see below).

A perturbation potential with $\sqrt{3} \times \sqrt{3}$ R30° periodicity gives rise to a larger unit cell and consequently a smaller surface Brillouin zone. The relation in k-space between the 1x1 and the reconstructed surface Brillouin zone is shown in Fig. 3.3e) together with the corresponding Fermi surface map obtained for the reconstructed silicide. The 1x1 Brillouin zone is shown in white, the smaller reconstructed Brillouin zone in gray (Fig. 3.3e). The non-symmetric $\overline{\Gamma} \overline{K} \overline{M}$ direction becomes in terms of the new Brillouin zone a symmetric $\overline{\Gamma}' \overline{M}' \overline{\Gamma}' \overline{M}'$ direction. Similarly $\overline{\Gamma} \overline{M} \overline{\Gamma}$ is now denoted as $\overline{\Gamma}' \overline{K}' \overline{M}' \overline{K}' \overline{\Gamma}'$. The high symmetry points \overline{K} and $\overline{\Gamma}$ become equivalent.

It is generally assumed that the stoichiometry of the topmost three layers (Si 1,2 and Y1 in Fig. 3.1a) does not change upon reconstruction. Vacancies are not formed in the topmost layer, since a stress relief is possible by lateral relaxation. Consequently the number of surface state bands in the unreconstructed surface Brillouin zone is not changed either. The new position of the surface bands arises if the new reciprocal lattice vectors $\overline{\Gamma}' \overline{\Gamma}'$ resp. $\overline{M}' \overline{M}'$ are considered, which serve as Umklapp scattering vectors and fold the unperturbed bands into the new $\sqrt{3} \times \sqrt{3}$ R30° Brillouin zone. Such a shift is exemplified for the hole pocket at \overline{M} (arrow in Fig. 3.3d), which appears at \overline{M}' , due to a translation via one reciprocal lattice vector $\overline{M}' \overline{M}'$ (black arrow). Similar translations yield the additional corresponding Umklapp bands, which are shown in gray in Fig. 3.3d).

Compared to the unreconstructed case, the Fermi surface should reflect the new periodicity and it has been proposed that the adaptation proceeds via

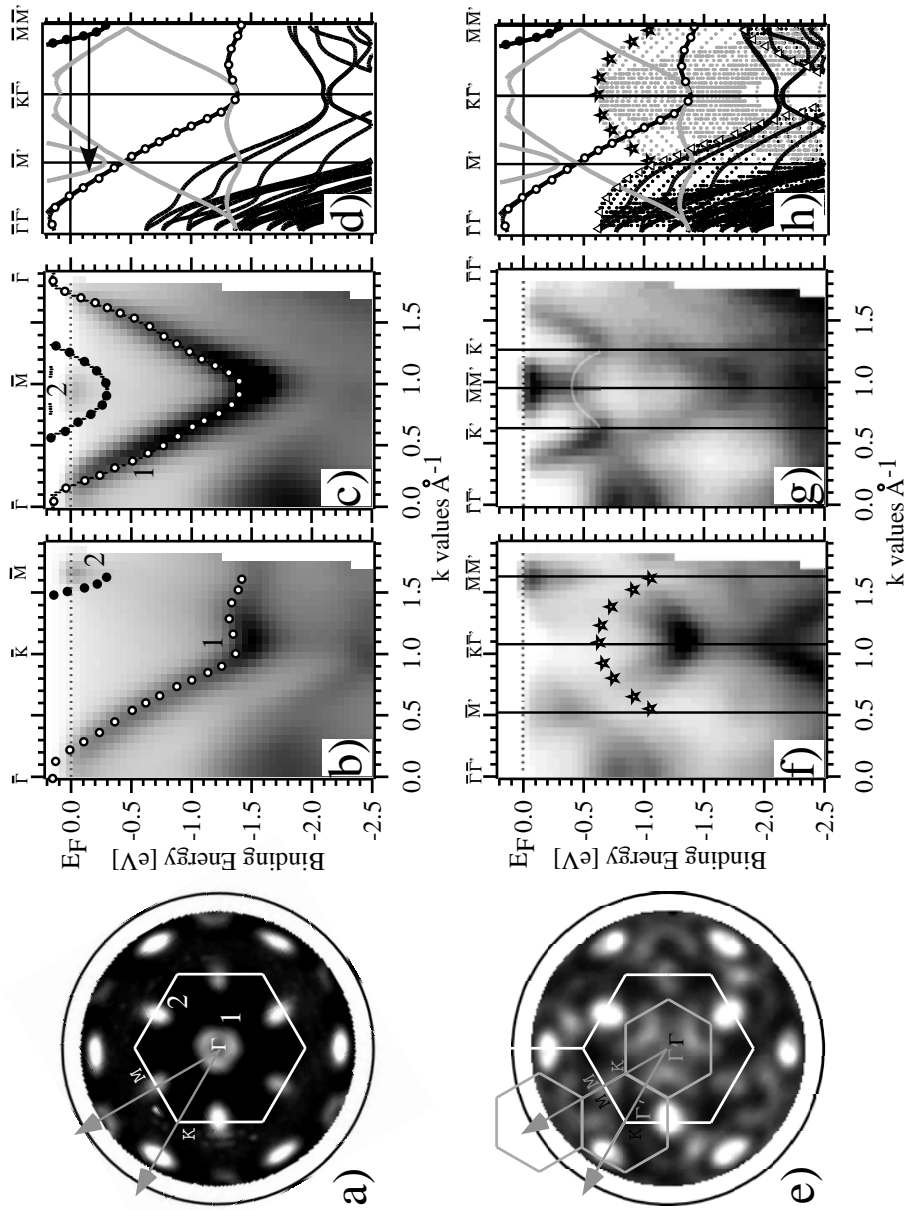


Figure 3.3: ARPES results for 1ML YSi_2 1×1 a,b and c) and $\text{YSi}_{1.7}$ $\sqrt{3} \times \sqrt{3}$ $R30^\circ$ e,f and g). a,e) Fermi surface map in parallel projection in a linear gray scale, white corresponds to high intensity. Surface Brillouin zones of the reconstructed (gray) and the unperturbed lattice (white) are shown. b,c,f and g) Dispersion plots along high symmetry directions, projected onto a k_{\parallel} scale, linear grey scale, high intensity corresponds to black. Results of band structure calculations are overlaid. d,h) Theoretical band dispersion including Umklapp-scattered bands (gray) and the projected silicon bulk band structure (small dots in h)

such a backfolding scheme[14]. In this sense, neglecting hybridization gaps at the zone boundaries, one expects the unperturbed two surface bands to appear in the new small Brillouin zone. And indeed it seems that the aforementioned hole pocket at \overline{M} is now similarly probed at \overline{M}' (cp. to Fig. 3.3e). An effect which seems to persist for higher order Brillouin zones as well. It has been already pointed out for ErSi_{1.7} [14], that the pockets at \overline{M}' seem to be non-symmetric with respect to the high symmetry point. This effect has been ascribed to matrix element effects. However more dramatically, there is no trace of a similar redistribution of spectral weight at $\overline{\Gamma}'$. The expected backfolding clearly suggest Umklapp bands at \overline{M}' and $\overline{\Gamma}'$, as it is shown in Fig. 3.3d).

The absence of an Umklapp band at $\overline{\Gamma}'$ (cp. to Fermi surface map in 3.3e) however does not mean that the corresponding electron pocket is not affected by the new lattice periodicity. Fig. 3.3g) shows clearly a parabolic band, similar to the unperturbed case of Fig. 3.3c), with a slightly larger Fermi wave vector of $\approx 0.3\text{\AA}$. The band exhibits minigaps and backfolding features, as they are suggested by the overlay (line as guide to the eye) in Fig. 3.3g) in the inside of the parabola. However the situation is less clear for the $\overline{\Gamma}'\overline{M}'\overline{\Gamma}'\overline{M}'$ direction (Fig. 3.3f). Evidently at the bottom of the electron band at -1.4 eV at $\overline{\Gamma}'$ a clear splitting is observable. Such a behavior is consistent with an Umklapp scattering scenario (Fig. 3.3d), which predicts a similar splitting at $\overline{\Gamma}'$. The sampling of this band seems to be different for higher order Brillouin zones, as it is evident in the comparison between \overline{M}' points of Fig. 3.3f) and g), respectively. The respective bands are only observable in $\overline{\Gamma}'\overline{M}'\overline{\Gamma}'\overline{M}'$ direction for a small k-range around $\overline{\Gamma}'$ and quickly fade out. For lower binding energies, closer to the Fermi level the respective Umklapp bands are hardly observed.

So far the discussion has been centered on the two surface states and how they are perturbed by the new lattice potential, as it is evidenced as a $\sqrt{3} \times \sqrt{3}$ R30° reconstruction. However these surface states have an appreciable extension into the bulk and are not strictly localized at the top silicon layer [7]. However the interaction with the continuum of bulk silicon states is hardly possible due to a gap in the surface projected band structure. Hence, the aforementioned states are true surface states, which decay exponentially into the bulk. The position of the silicon bulk band edge with respect to the surface state is shown in Fig. 3.3h) as open triangles. Quite contrary, for the reconstructed case, the new periodicity opens up new possibilities of surface-bulk interactions as well. Similarly to an Umklapp scattering of the surface states, the projected silicon band structure has to be evaluated via Umklapp

scattering in terms of the new periodicity as well. Such an evaluation has been done for the $\overline{\Gamma K M}$ direction. The result is shown in Fig. 3.3h). The projected band structure of silicon (small black dots) is backfolded at the $\overline{\Gamma'}$ point (gray dots). Compared to the unperturbed case, where the distance between surface state (open dots in Fig. 3.3h) and bulk band edge (triangles in Fig. 3.3h) does not permit an appreciable interaction, the surface state is expected to interact strongly with the underlying substrate in the backfolded scheme. The upper band edge of the backfolded projected bandstructure is emphasized with star-shaped markers in Fig. 3.3h) and cuts the electron pocket around $\overline{\Gamma'}$. The electron pocket in the measurement seems to sample this band edge, as it is evident in Fig. 3.3f). The small k-space region, where increased emission intensity is observed, is confined by the band edge (star markers in Fig. 3.3f).

3.4 Discussion

The interaction of confined electron states with an underlying bulk band structure has been discussed previously in relation to quantum well states, where similar effects have been observed for Mg on Si(111)[15]. There is no rigorous distinction between a quantum well state and a surface state apart from the higher degree of localization for the surface state. In this respect the observed surface substrate interaction seems not unusual and certainly feasible for the measured thickness. It is the unique role of the reconstructed "spacer" layer, which renders this system potentially unusual. The "spacer" layer of $\text{YSi}_{1.7}$ $\sqrt{3} \times \sqrt{3}$ R30° seems to provide the crystal momentum to enable an interaction between surface and bulk bands, via Umklapp scattering. A schematic sketch is shown in Fig. 3.4.

The interaction, which is not possible in the unreconstructed case, might become feasible due to an interaction of the substrate states with the crystal lattice of the spacer layer. It might be speculated upon if such a scenario might serve to stabilize the $\sqrt{3} \times \sqrt{3}$ R30° reconstruction itself. It is to be pointed out, that such a surface state-bulk interaction might even proceed for large overlayer thicknesses, as it has been confirmed for an sp surface state on W(110)[16]. The electronic structure of the reconstructed $\text{YSi}_{1.7}$ layer has been completely neglected in this argumentation. It would be highly desirable to perform realistic band structure calculations based on an exact structural model with possible lateral relaxations and including both interface and surface effects and photoemission matrix elements. These calculations should clarify

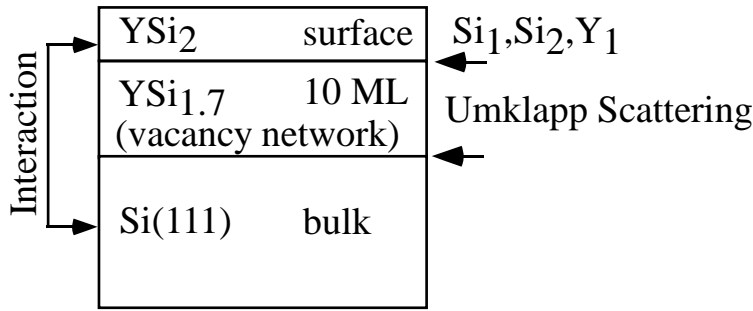


Figure 3.4: Schematic sketch of surface state-bulk interaction

the strength of the scattering potential and the hybridization gaps due to the vacancy network, which should yield realistic Umklapp bands, especially at E_F , where large discrepancies between theory and experiment seem to exist.

3.5 Conclusion

We have presented XPD data for 1 ML YSi_2 and 2 ML $\text{YSi}_{1.7}$. The agreement between multiple scattering calculations based on a cluster model and the measurements are convincing. A structure model is confirmed, which consists of a buckled Si bilayer above a hexagonal Y layer for 1 ML YSi_2 . For 2 ML $\text{YSi}_{1.7}$ additional maxima are observed, which can be assigned to emission from the second, deeper lying Y layer. UV photoemission measurements for YSi_2 are in excellent agreement to DFT calculations. For thicker films the comparison between experimental data and DFT results is less straightforward. We observe a Fermi surface, which is dominated by Umklapp scattering of only one surface band at \bar{M} . For higher binding energies clear traces of Umklapp scattering at the Brillouin zone boundaries related to the $\sqrt{3} \times \sqrt{3}$ R30° reconstruction are found. There is an appealing correspondence between a drop of photoemission intensity and a band edge crossing of the Si(111) projected band structure. The necessary crystal momentum for the proposed interaction between surface state and bulk silicon bands would be provided by the reconstructed spacer layer.

Acknowledgements We are greatly indebted to our workshop and electric engineering team. Financial support by the Fonds National Suisse pour la Recherche Scientifique is gratefully acknowledged.

Bibliography

- [1] L. Magaud, A. Pasturel, G. Kresse, and J. Hafner. *Phys. Rev. B*, 55:13479, 1997.
- [2] C. Rogero et. al. to be published.
- [3] C. Rogero, C. Polop, L. Magaud, J. L. Sacedón, P. L. de Andrés, and J. A. Martín-Gago. *Phys. Rev. B*, 66:235421, 2002.
- [4] T.P. Roge, F. Palmino, C. Savall, J.C. Labrune, P. Wetzels, C. Pirri, and G. Gewinner. *Phys. Rev. B*, 51:10998, 1995.
- [5] L. Stauffer, A. Mharchi, C. Pirri, P. Wetzels, D. Bolmont, G. Gewinner, and C. Minot. *Phys. Rev. B*, 47:10 555, 1993.
- [6] J. Voit, L. Perfetti, F. Zwick, H. Berger, G. Margaritondo, G. Gruener, H. Hoehst, and M. Grioni. *Science*, 290:501, 2000.
- [7] C. Rogero, C. Koitzsch, M. E. González, P. Aebi, J. Cerdá, and J. A. Martín-Gago. *Phys. Rev. B*, 69:045312, 2004.
- [8] C. Koitzsch, C. Rogero, J. A. Martín-Gago, and P. Aebi. accepted for publication in *Surf. Sci.*
- [9] T. Pillo, J. Hayoz, P. Schwaller, H. Berger, P. Aebi, and L. Schlapbach. *Appl. Phys. Lett.*, 75:1550, 1999.
- [10] F.J. Garcia de Abajo, M.A. van Hove, and C.S. Fadley. *Phys. Rev. B*, 63:075404, 2001.
- [11] L. Despont et. al. to be published.
- [12] P. Blaha, K. Schwarz, , G.K.H. Madsen, D. Kvasnicka, and J. Luitz. 2001. *Wien2k, An Augmented Plane Wave + Local Orbitals Program for Calculating Crystal Properties* (Karlheinz Schwarz, Tech. Univ. Wien, Austria) ISBN 3-9501031-1-2.
- [13] T. Greber, J. Wider, E. Wetli, and J. Osterwalder. *Phys. Rev. Lett.*, 81:1654, 1998.

-
- [14] J. A. Martín-Gago, J.Y. Veullen, C. Casado, and T.A. Nguyen Tan. *Phys. Rev. B*, 55:5129, 1997.
- [15] L. Aballe, C. Rogero, P. Kratzer, S. Gokhale, and K. Horn. *Phys. Rev. Lett.*, 87:156801, 2001.
- [16] C. Koitzsch et. al. to be published.

Part II

**Electronic Structure of Rare
Earth Hydrides**

Chapter 4

Introduction

4.1 General Remarks

Rare earth-hydrides (ReH_x) (Re=La and the Lanthanides and for argumentative simplicity Sc and Y are referred to as rare earths as well) have received considerable interest mainly due to promising applications in the field of hydrogen storage [1]. The ease of bulk hydrogenation and the simple hydrogen release seemed to facilitate a means of storing this potentially explosive gas for the use in modern fuel cell applications. Basic research on this subject however could not be based on single crystalline material since the hydrogen incorporation into the lattice leads to large stresses in the material, which tend to crack and powderize the material.

More recently thin films of Re-hydrides have attracted widespread interest due to the possibility to tune very elegantly electronic properties via adjusting the hydrogen content in the material. Moreover the hydrogenation of thin films does not seem to affect the crystallinity of the material, contrary to bulk samples. Hence they offer a possibility for basic research to study single crystal hydrides. The aforementioned hydrogen dependent properties were spectacularly demonstrated for the optical absorption coefficient in the YH_x system. The change between the metallic pure Y, the still metallic and hence reflecting dihydride and the insulating and hence transparent trihydride became commonly known as the switchable mirror effect [2]; switchable, because the effect can be reversed via depleting the crystal from hydrogen (e.g. via heating) The same effect was observed for the whole class of the Lanthanides and their alloys and even for Mg based compounds[3]. The observed change in the op-

tical properties can be characterized in more scientific terms as a hydrogen induced metal-insulator (Me-I) transition. Somehow the addition of hydrogen to a metal leads to an insulating material, whose electronic structure is characterized by an excitation gap, which is in the visible optical range for the Re-hydrides. The prospect of using these materials as optical switches initiated of course numerous experimental efforts in order to increase cycling endurance, switching speed and finally a working device was demonstrated [4][5]. In the wake of these increased activities other properties, tuneable with adjusting the hydrogen content, were discovered. Especially magnetic properties were also shown to depend strongly on the hydrogen content. Gadolinium is a ferromagnet, while GdH_2 orders antiferromagnetically at low temperatures[6]. It was shown that it is possible to tune Ruderman, Kasuya, Kittel, Yosida (RKKY) interactions via a hydrogenation of an appropriate spacer layer [7].

4.2 Theoretical Models

On the other side, theory started out to explain the Me-I transition via modern electronic structure theory. Quite surprisingly, the problem required some rather subtle concepts of modern solid state physics.

The addition of hydrogen to a metallic host can be viewed as an addition of an unpaired electron shell to the metallic host. Depending on the electronegativity of the hydrogen and the metal site, one can imagine the formation of negatively or positively charged H sites. In the former case, electrons from the metallic host are withdrawn and added to hydrogen sites (crudely speaking in order to create a stable $1s^2$ configuration). In the latter, the initial H related electrons are attracted from the surrounding metal and a positively charged H site is left over. Depending on the charge state of the H site, one distinguishes between the protonic and anionic model for positively- and negatively charged hydrogen sites. The charge state of hydrogen was experimentally determined to be negative [8][9]. In a band theory approach, the occupation of H sites by two electrons corresponds to the formation of a hydrogen related band, which is below the Fermi level and hence occupied by two electrons. Contrarily the protonic model would correspond to the formation of an empty hydrogen related band above the Fermi level.

Switendick [10][11] undertook a pioneering band structure calculation for YH_x based on a non-self consistent augmented plane wave (APW) approach. Upon the formation of the dihydride phase (two additional H atoms in the unit

cell) a fully occupied hydrogen related band, below the metal d-band, and well below the Fermi level was calculated. For the insulating trihydride phase an electronic gap of 1.5 eV was obtained. Quite unexpectedly the finding of a large gap, insulating ground state for YH_3 could not be reproduced by self consistent state-of-the-art electronic structure calculations, which yielded a metallic or semi-metallic state for the trihydride phase [12, 13] with an, admittedly very small, band overlap at E_F . It was pointed out by Kelley [14], that a symmetry breaking could turn the semi metal into an insulator via a gap opening due to the new crystal potential. Such a Peierls transition is energetically favoured if enough energy is gained via the band lowering in order to compensate for the deformation of the lattice. The electronic structure of the unperturbed lattice seemed to support such a transition, as evidenced by an apparently nested Fermi surface [15]. A vigorous debate started about the possibility to detect such a broken-symmetry structure experimentally. The proposed wave-like displacement of hydrogen, which should break the symmetry of the lattice is very difficult to detect experimentally. One of the possible structural candidates is a distorted HoD_3 structure which already forms a $\sqrt{3} \times \sqrt{3}$ R30° reconstruction in the hydrogen sublattice of the otherwise hcp YH_3 lattice. Still the obtained gap sizes for various complicated broken symmetry structures did not agree with gap size estimates from optical spectroscopies. Even more puzzling, LaH_3 which remains cubic in the trihydride phase (a broken symmetry can be excluded) was observed to be similarly insulating and switching as well. This renders the apparent subtleties of the YH_3 crystalline structure as of minor importance for the metal insulator transition.

Due to the obvious shortcomings of LDA, which does not treat electron correlation effects properly and since such a disagreement between LDA calculations and experimental observations has also been found in strongly correlated electron systems like NiO_2 , a many body (MB) approach (hence including electron correlation) to the problem was proposed by Ng and Eder[16][17].

Ng[16] used a trial wave function, initially proposed by Chandrasekhar [18]. It is a two-electron wave function, which yields a bound state for the corresponding H^- ion, with a quite reasonable binding energy of 0.7 eV. The wave function can be illustrated as two bound electrons residing in different orbitals (Fig. 4.1). The electrons have opposite spin, but nevertheless the outermost electron is not in the H 2s orbital. The electron correlation is introduced via a term $c \cdot |\mathbf{r}_1 - \mathbf{r}_2|$, which tends to keep the electrons apart and leads to a correlated motion and finally to a stable configuration. The resulting band structure

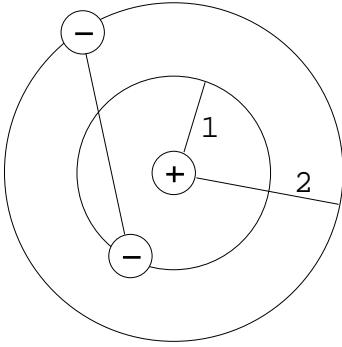


Figure 4.1: Schematic representation of an H^- ion, the correlated motion of the valence electrons is indicated with a line (see text).

(including the many body physics) is obtained in a Gutzwiller approach and can then be compared to LDA bandstructures. Since LDA neglects the correlated electron motion, such a comparison immediately traces the influence of electron correlation in these materials. Fig. 4.2 shows the corresponding bandstructure for LaH_2 and LaH_3 (Fig. 4.2a,b) obtained via calculations in the framework of LDA (black and gray circles) and via a many body approach (open circles). The bandstructures represented with black circles (open and solid) originate directly from Ng's work. An older LDA calculation [19] is shown as well for comparison in gray circles. The many-body correction to the LDA calculation (compare open and solid black circles) reveals the essential physics originating from electron correlation. LaH_2 is experimentally a good metal, which is theoretically well reproduced, since there is no gap at E_F for neither the LDA calculations nor the MB bandstructure. The question arises if there should be at all effects of electron correlation at play for the dihydride phase? One has to bear in mind that the initial motivation for the MB approach were the peculiar properties of the H^- ion. An ionic picture is certainly not very appropriate for the metallic dihydride. But still the effects of electron correlation are quite dramatic for the bandstructure (even if they do not affect the transport properties) as it is shown in Fig. 4.2a). The bandwidth at the Γ -point is dramatically reduced for the calculation including correlation. The gray bars on the right-hand side indicate the narrowing for MB calculations (open circles) compared to LDA calculations (solid circles). At Γ the hydrogen related LDA bandwidth (shading 1) is significantly reduced for the MB calculation (shading 3). However the older LDA calculation from Gupta et. al. shows

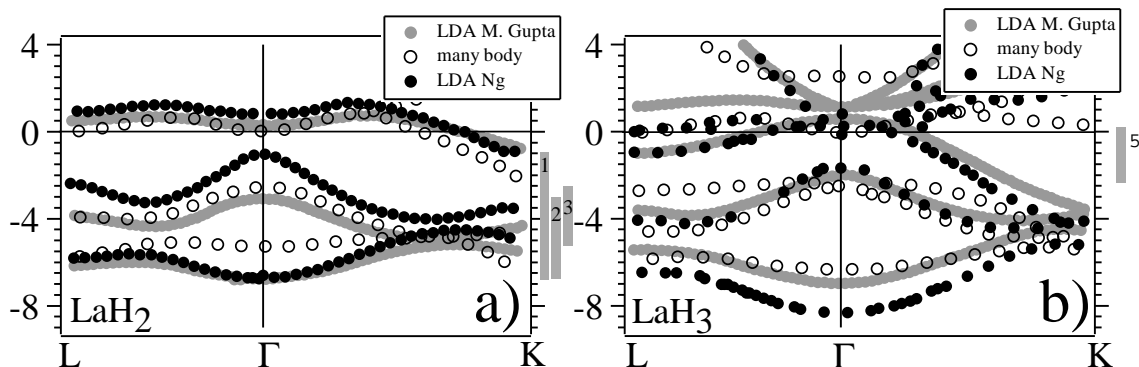


Figure 4.2: Comparison of LDA band structures (gray and black circles) to a many-body approach (open circles). For comparison two different LDA band structures are shown (gray and black circles).

a reduced bandwidth as well (shading 2). These kind of many-body effects on the k-resolved band structure can be directly probed by ARPES and were one of the motivations to study experimentally the rare earth **dihydride** phase in chapter 6. Please note however, the large error margin in the LDA calculations (manifested in the two different LDA calculations in Fig. 4.2a), which cast a severe doubt on discussions about absolute band positions.

The MB effects should be much more important for the trihydride phase (Fig. 4.2b) due to the reduced screening. In this case, the band renormalization should directly affect optical and transport properties. LDA calculations show a very small fundamental gap or even a slight band overlap (semi-metallic ground state), while the MB band structure shows a large gap insulator (gray shading labeled as 5). In fact, an assessment of the electron correlation strength is made via a tight-binding fit of the LDA band structure, which allows for a determination of the physically more illustrative hopping parameters. Interestingly a necessary large renormalization/difference for the LDA-derived hopping parameters indicated the importance of electron correlation for the problem. The proposed local models [16][17] allow to explain, why the insulating state exists even for hydrogen deficient ReH_{3-x} with a very high vacancy (impurity) level. The existence range for the insulating state extends below $\text{ReH}_{2.9}$, which is a very high doping level for conventional semiconductors.

The second model of Eder[17], which includes correlation as well focuses

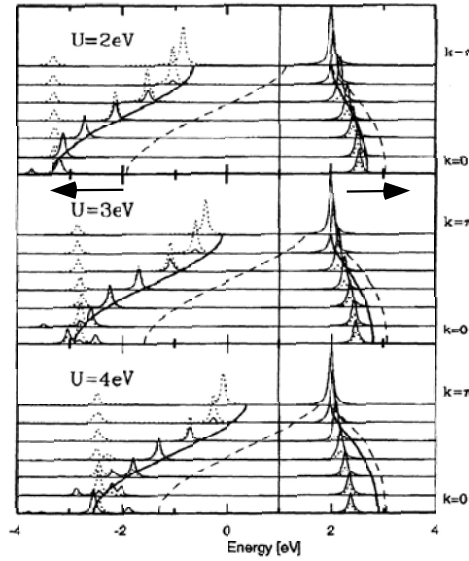


Figure 4.3: Single particle spectral function of a linear chain model calculation. Right-hand (left-hand) side corresponds to electron addition (removal). The dashed dispersion curve gives the mean field result. The scissors-like correction of valence and conduction band is indicated with two arrows.

again on the particular properties of the H^- atom. Similar to Ng et. al., it was shown that the interaction between hydrogen and the surrounding atoms depends crucially on the electron occupation of the hydrogen site. The H^- ion has a vastly different orbital radius, compared to the neutral case, and in turn very different occupation dependent hopping parameters are to be expected for fluctuations involving "negatively charged" H sites and "neutral" sites. It is claimed, that if the resulting differences in the hopping integrals are comparable to other energy scales, the interaction must be treated explicitly. In a model calculation involving a 6-atom linear chain of Y-H, such an occupation dependent hopping integral was introduced in addition to the usual on-site Coulomb interaction of the Hubbard or Anderson impurity models. The resulting corrections of the single particle spectral function with respect to "classical" LDA calculations is shown in Fig. 4.3. The mean field result is shown as a dashed dispersion line, while the result including correlation is shown as a full dispersion line.

It is of course tempting to generalize results from such a model calculation to YH_3 . Upon inspection of the spectral function, one would expect for YH_3 the opening of a substantial gap and the retainment of the calculated LDA bandwidth. In this sense the result is quite different to the aforementioned Ng model, since there the gap is opened due to a band narrowing, while in this latter case the band is more opened due to a scissors like shifting of valence and conduction band. Please note that different parameter values of the Coulomb repulsion U do not change the mechanism opening the gap (Fig.4.3).

After this short review of the two developed theories including electron correlation, it is to be pointed out, that the validity of the two models can be directly probed with ARPES and the interested reader is referred to Chapter 7.

Very recently, it was pointed out that the failure of LDA to produce significant gaps for the trihydride phase might not be due to underestimated correlation terms, but might be caused by an unjustified interpretation of Kohn-Sham eigenvalues (LDA based eigenvalues) as single particle excitation energies. More crudely speaking, it was shown that YH_3 might be more similar to a conventional semiconductor like Si (where LDA fails to reproduce the correct band gap as well) and hence one observes just the usual shortcomings of LDA regarding excitation gap sizes. A technical means to obtain correct excitation energies from LDA is to correct them with the GW method. This method has proven to yield rather satisfactory gap sizes for various materials with known underestimated LDA gaps such as silicon and germanium. There are two independent studies of YH_3 with the GW method [20][21][22]. Again the authors obtained different results regarding the difference between the LDA band structure and the "correct" bandstructure (Fig. 4.4a,b,c). Van Gelderen (Fig. 4.4a,b for LDA results and GW results, respectively) claims a slight increase in bandwidth (though there is a decrease for the LaF_3 structure in his work), which suggests rather extended hydrogen related states and a shift of conduction and valence band. Miyake obtained an unaltered valence band. Here the gap is obtained via a shift of the conduction band. Finally it is to be decided, whether the gap opening is due to large electron correlations at hydrogen sites or not. An indication can be given by comparing the experimental band structure to the different models, namely the models from Ng, Eder, Miyake and van Gelderen. An attempt in this direction is made in chapter 7.

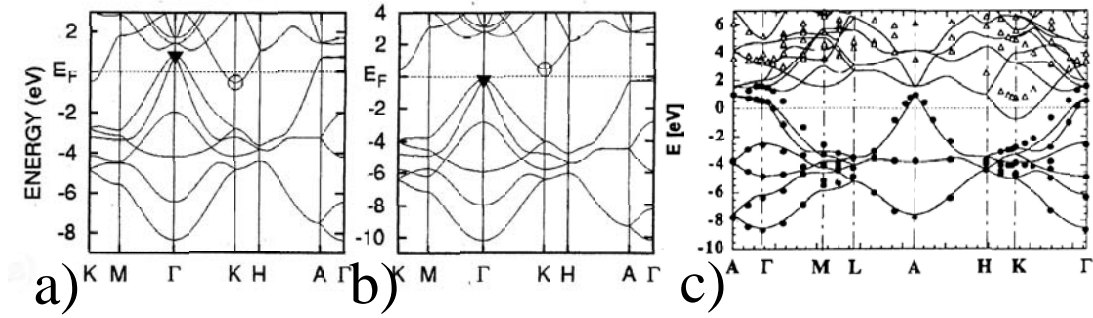


Figure 4.4: Comparison of GW corrections to LDA band structures from van Gelderen and Miyake regarding YH_3 in the LaF_3 structure. a) LDA bandstructure van Gelderen b) GW band structure van Gelderen c) solid lines LDA band structure Miyake; solid circles GW valence band, open triangles GW conduction band

4.3 This Work

One of the main goals of the present work is the application of DFT to describe the hydrogenation of rare earth materials and the comparison of its predictions to measured photoemission data. Theoretically we rely on calculations in the framework of LDA, namely the APW+lo code Wien2k [23]. These calculations are comparable to the state-of-the-art before the advent of the calculations of Ng [16] and Eder [17] (which include correlation effects) and the calculations within the GW approximation [20, 21, 22]. Nevertheless it should be possible to comment on the adequacy of the various theories since they all compare their more refined results to standard LDA calculations.

Chapter 5 reports in a purely theoretical approach on LDA calculations for face centered Y, YH_2 , YH_3 and YH_4 . Special emphasis is drawn to the evolution of the band structure with increasing hydrogen content. It is found, that the different hydrogen absorption sites interact very differently with the Y d-band manifold. Tetrahedral hydrogen affects mainly d-bands of t_{2g} symmetry, while octahedral hydrogen interacts primarily with e_g bands. We find clear indications that the formation of the dihydride phase acts as precursor for the Me-I transition, since the filling of the tetrahedral H lattice leads to a redistribution in the d-band manifold, such that subsequent octahedral hydrogen can interact with (and remove) the remaining e_g Fermi surface. In this sense this

paper presents an improvement to the initial pioneering work of Swietendick [10][11] since the calculations are now self consistent and secondly we present proof for the selective interaction of H sites and Y d-bands, which we believe is crucial for the mechanism of the Me-I transition.

The formation of the dihydride phase is understood as a precursor phase for the Me-I transition. Its electronic structure is discussed in Chap. 6, where angle-resolved photoemission data for ScH₂, YH₂, GdH₂ and LaH₂ are presented. These results are only possible due to recent experimental achievements regarding the preparation of epitaxial hydride films in a UHV environment [24]. Theoretical APW+lo calculations show that the band structure of the different dihydrides should be very similar. An inspection of the data sets confirms this assumption. Via applying the free electron final state model, we achieve excellent agreement between LDA calculations and measurements for the occupied d-band. Nevertheless we find a less convincing LDA description of the hydrogen related bands, which already experimentally confirms the expected deficiencies of LDA with regard to the description of hydrogen related states. The Fermi surface topology is analyzed with theoretical calculations of the generalized susceptibility, which shows only weak nesting. This computational result challenges the view of the dihydride Fermi surface as a nested, warped cube.

Finally Chapter 7 is dedicated to the trihydride phase. ARPES measurements are presented and in detail compared to LDA calculations. A comparison to the aforementioned theoretical models based on strong correlations and the GW correction of LDA results in a preference to the model of Eder et. al. [17]. It must be however stated that this model calculation does not provide a similar reference band structure (Fig. 4.3) as the other calculations, which renders the comparison slightly biased. A better understanding of the photoemission data would certainly be facilitated if the calculations would be better adapted to the photoemission process itself. Namely the calculation of photoemission matrix elements would greatly simplify the identification of specific bands, which in turn would open new experimental possibilities as well, such as the clever use of photon energy and polarization.

Bibliography

- [1] L. Schlapbach and A. Zuettel. *Nature*, 414:23, 2001.
- [2] J.N. Huiberts, R. Griessen, J.H. Rector, R.J. Wijngaarden, J.P. Dekker, D.G. de Groot, and N.J. Koeman. *Nature*, 380:231, 1996.
- [3] T. Richardson, J. Slack, R. Armitage, R. Kostecki, B. Farangis, and M. Rubin. *Appl. Phys. Lett*, 78:3047, 2001.
- [4] P. van der Sluis and V. M. M. Mercier. *Electrochim. Acta*, 46:21672171, 2001.
- [5] R. D. Armitage, M.D. Rubin, T.J. Richardson, N. O'Brien, and Y. Chen. *Appl. Phys. Lett.*, 75:1863, 1999.
- [6] R.R. Arons and J. Schweizer. *J. of Appl. Phys.*, 53:2645, 1982.
- [7] F. Klose, D. Nagengast Ch. Rehm, H. Maletta, and A. Weidinger. *Phys. Rev. Lett*, 78:1150, 1996.
- [8] S.J. van der Molen, M.S. Welling, and R. Griessen. *Phys. Rev. Lett*, 85:3882, 2000.
- [9] M. Rode, A. Borgschulte, A. Jacob, C. Stellmach, U. Barkow, and J. Schoenes. *Phys. Rev. Lett.*, 87:235502, 2001.
- [10] A.C. Switendick. *Sol. State Comm.*, 8:1463, 1970.
- [11] A.C. Switendick. *Int. J. Quantum Chem.*, 5:459, 1971.
- [12] D.K. Misemer and B.N. Harmon. *Phys. Rev. B*, 26:5634, 1982.
- [13] M. Gupta. *Solid State Communications*, 27:1355–1359, 1978.
- [14] P.J. Kelley, J.P. Dekker, and R. Stumpf. *Phys. Rev. Lett.*, 78:1315, 1997.
- [15] Y. Wang and M.Y. Chou. *Phys. Rev. Lett.*, 71:1226, 1993.
- [16] K.K. Ng, F.C. Zhang, V.I. Anisimov, and T.M. Rice. *Phys. Rev. Lett*, 78:1311, 1997.
- [17] R. Eder, H.F. Penn, and G.A. Sawatzky. *Phys. Rev. B*, 56:10115, 1997.

- [18] S. Chandrasekhar. *Astrophys. J.*, 100:176, 1944.
- [19] M. Gupta and J.P. Burger. *Phys. Rev. B*, 22:6074, 1980.
- [20] P. van Gelderen, P. A. Bobbert, P.J. Kelly, and G. Brocks. *Phys. Rev. Lett.*, 85:2989, 2000.
- [21] P. van Gelderen, P. A. Bobbert, P.J. Kelly, G. Brocks, and R. Tolboom. *Phys. Rev. B*, 66:075104, 2002.
- [22] T. Miyake, F. Aryasetiawan, H. Kino, and K. Terakura. *Phys. Rev. B*, 61:16491, 2000.
- [23] P. Blaha, K. Schwarz, , G.K.H. Madsen, D. Kvasnicka, and J. Luitz. 2001. Wien2k, An Augmented Plane Wave + Local Orbitals Program for Calculating Crystal Properties (Karlheinz Schwarz, Tech. Univ. Wien, Austria) ISBN 3-9501031-1-2.
- [24] J. Hayoz, Ph.D. thesis, University of Fribourg, Switzerland (1999).

Chapter 5

Ab-initio Investigation of the Hydrogenation of Y

Christian Koitzsch¹, Michael Gunnar Garnier¹ and Philipp Aebi¹

¹*Institut de Physique, Université de Neuchâtel, CH-2000 Neuchâtel, Switzerland*

Physica Scripta, Vol. T109, 163 (2004).

Abstract: We present an *ab-initio* electronic structure study of a face centered (fcc) cubic Y lattice, which is subsequently filled with hydrogen in tetrahedral and octahedral sites. The stoichiometry of the calculated compounds is Y, $\text{YH}_2^{\text{tetra}}$, YH_3 and $\text{YH}_1^{\text{octa}}$. Upon placement of hydrogen in tetrahedral sites we note for the $\text{YH}_2^{\text{tetra}}$ phase a new, fully occupied hydrogen related band and a redistribution in the d-band manifold at the Fermi level. Interestingly during the fcc $\text{Y} \rightarrow \text{YH}_2^{\text{tetra}}$ transition the overall topology of the Fermi surface (FS) is not changed, but we note a change in character from t_{2g} to e_g of the responsible band. It is this change to e_g character which allows subsequent H in octahedral sites to significantly interact with the FS, finally enabling the metal-insulator transition while reaching YH_3 . A placement of hydrogen solely in

octahedral sites does not affect significantly the t_{2g} d-band at the Fermi level.

5.1 Introduction

The valence electronic structure of rare earth hydrides is both technologically important and fundamentally interesting. Potential optical applications can be envisioned based on the recent discovery of Huiberts et. al. [1] of a reversible (switchable) metal-insulator (Me-I) transition between the reflecting, metallic dihydride and the insulating, transparent trihydride. In a simple ionic picture this transition corresponds to a complete capture of the three Y valence electrons $[\text{Ar}]4d^15s^2$ by the three, then negatively charged H^- ions. However in a single particle picture hybridisation will not allow the H atoms to remove all valence electrons and the system remains metallic. Indeed LDA calculations [2] show a metallic state for YH_3 . The only way a (still insufficiently small) gap could be obtained was via a Peierls type symmetry breaking of the complicated HoD_3 structure [2]. This argumentation certainly fails for the sister compound LaH_x , which does exhibit a similar Me-I transition without complicated crystal structure changes. Later on, various models [3],[4] including strong electron correlations reproduced the insulating ground state and led to a deeper understanding of the electronic interaction between hydrogen and the metallic host lattice. Special emphasis was drawn to the peculiar properties of H^- , whose insufficient description within LDA, is believed to cause the wrong ground state for YH_3 . The debate whether strong electron correlations play a role or not in this material are ongoing, since recent GW calculations are able to reproduce the insulating ground state without use of strong correlations [5, 6, 7].

In the present paper we deliberately assume a very simple fcc based structure for YH_x (Fig. 5.1a). This assumption decouples effects arising from crystal structure changes (such as the complicated HoD_3 structure proposed for YH_3) from the effects of hydrogenation as calculated via LDA. In this sense the paper follows the spirit of the pioneering calculations of Switendick [8] with the benefit of higher accuracy (self consistency) and recent experimental and theoretical developments, which initiate a critical assessment of the obtained LDA based band structures.

5.2 Computational Details

The electronic structure calculations are based on Density Functional Theory (DFT) and the full potential linearized augmented plane wave code FPLAPW Wien2k [9] was employed. There the unit cell is divided into non-overlapping atomic spheres (muffin tin) and an interstitial region. In the muffin tin region the basis functions are comprised of atomic-like wavefunctions while the interstitial region is described with plane wave basis functions.

The crystallographic structure for the four studied compounds is derived from the published experimental structure of YH_2 [10]. A lattice constant of 5.6201 \AA was assumed for all calculated hydrides. The sole difference between the structures are the number and the positions of the incorporated hydrogen atoms. It is assumed that the Y sublattice is not distorted and remains fcc, independent of the degree of hydrogen filling. The fcc metal lattice and the octahedral and tetrahedral hydrogen lattice sites are sketched in Fig. 5.1a). Fig. 5.1b and c) display calculated FSs of fcc Y and YH_2 , respectively (see below).

With regard to the specific Wien2k related parameters, we used a muffin tin radius for rare earth atoms and hydrogen atoms of 1.16 \AA and 0.85 \AA , respectively. Self-consistency was judged to be, when the total energy change was less than 0.1 mRy in subsequent cycles. The calculation was based on 10000 k-points, which corresponds to 286 k-points in the irreducible wedge of the Brillouin zone (BZ). After obtaining self-consistency, the eigenvalues were determined along some high symmetry lines as shown in Fig. 5.2.

5.3 Results

Yttrium: The computed band structure for fcc yttrium (Fig. 5.2a) is typical for a fcc transition metal. The trivalent Y gives rise to an sp-band (open dots), with a binding energy of -4.6 eV at Γ and a partially occupied d-band manifold. A band with t_{2g} character (black dots) cuts the Fermi level between Γ and X, while the bands with e_g symmetry (grey ovals) remain above the Fermi level.

$\text{YH}_2^{\text{tetra}}$: Experimentally an exposure of the clean metal to hydrogen leads to the formation of the dihydride phase, where hydrogen occupies tetrahedral sites. The corresponding band structure is shown in Fig. 5.2b). The aforementioned Y sp-band (open dots) hybridizes with the H 1s state, leading to an almost rigid shift of this band by 3.4 eV to higher binding energies. Accordingly

the position at the Γ point changes from -4.6 eV to -8 eV. A new band is formed above the Y sp-band of almost entirely H 1s character (open rectangles in Fig. 5.2b). It is found between the Y sp band (open dots) and the d-band (grey ovals). There is an indirect energy overlap between this band at its maximum at the Γ point and Y d bands at its minimum at the X point. Correspondingly the dihydride remains metallic, even for a considerable Fermi level lowering (in a rigid band model) upon further hydrogen uptake as suggested in an ionic picture. Furthermore the hydrogenation affects very much the aforementioned d-band of t_{2g} character (black dots), which was cutting the Fermi level between Γ and X for the pure metal (Fig. 5.2a). This band (black dots in Fig. 5.2b) does not cut the Fermi level anymore and has acquired instead an upwards dispersion between Γ and X. Very importantly the FS is now formed solely by one d-band of e_g symmetry (grey ovals in Fig. 5.2b). Recently it has been experimentally confirmed by angle-resolved photoemission that this single band hydride FS is indeed largely correct for ScH_2 , YH_2 , GdH_2 and LaH_2 [11]. This symmetry change due to the strong interaction between H in tetrahedral sites and the Y t_{2g} band is exploited in the formation of the trihydride phase.

YH₃: A further exposure to hydrogen leads to the formation of the trihydride phase, which is characterized by the hydrogen occupation of tetrahedral and octahedral sites. The calculated band structure for fcc YH₃ is shown in Fig. 5.2c). The band bottom of the initial Y sp-band is now found at approximately -10 eV (open dots in Fig. 5.2c) and the YH₂^{tetra} related H 1s band (open rectangles) is virtually unaffected. The addition of octahedral hydrogen leads to an upwards dispersion of the e_g band (grey ovals) between Γ and X. Again the introduction of hydrogen leads to the formation of one new band (black rectangles in Fig. 5.2c), which is partially unoccupied and overlaps with the d derived bands (circled in Fig. 5.2c). As explained in the introduction, this renders the trihydride a LDA metal, which is in disagreement to the experimental data.

YH₁^{octa}: In order to deepen our band analysis, we calculated the electronic band structure for a fcc Y lattice with H solely in octahedral sites and the result is shown in Fig. 5.2d). We note a very similar Y sp-band (black dots in Fig. 5.2d) for the YH₁^{octa} structure (Fig. 5.2d) compared to the YH₂^{tetra} (Fig. 5.2b) structure. Obviously, compared to fcc Y, the t_{2g} derived d-band (black dots) between Γ and X remains at its position at the Fermi level, E_F , similar to the pure metal (Fig. 5.2a). The e_g derived band (grey ovals) is lowered in binding energy compared to the fcc Y case. For YH₁^{octa} the largest changes appear for

the Γ L direction and not for the Γ X direction. For Γ L we note a H 1s derived band (grey rectangles), which now cuts the Fermi level.

5.4 Discussion

The preceding results illustrate a number of important hydrogen related electronic structure changes. We note a considerable lowering of the Y sp band (open dots) by 3.4 eV for $Y \rightarrow YH_2^{tetra}$ and by 2 eV for $YH_2^{tetra} \rightarrow YH_3$, which might explain the readiness of hydrogen-incorporation into the lattice. Furthermore we observe a strong interaction between H in *tetrahedral* sites and Y d-states of t_{2g} symmetry (black dots), while *octahedral* sites interact mainly with e_g d-states (grey ovals). It is to be pointed out that the general shape of the FS is conserved during the transition between fcc Y and YH_2^{tetra} . The FSs for the pure metal and YH_2^{tetra} are shown in Fig. 5.1 b and c). The difference is just that the FS in the Y case is due to a t_{2g} band, while in the YH_2^{tetra} case it is derived from an e_g band (as compared with the corresponding band structures in Fig. 5.2a and b). In addition slight deviations occur in the vicinity of the W point, which could easily be removed by a rigid shift (arrow in Fig. 5.2a) of the Y sp-band (black dots) for the pure metal. The general shape of these FSs (Fig. 5.1b and c) is a warped cube with protruding necks extending in the Γ L direction. Contrarily the FS is largely different for YH_1^{octa} due to the E_F crossing of a H 1s related band between Γ and L. In addition to the very different FS, we note a partially unoccupied band of hydrogen character (grey rectangles Fig. 5.2d), which does not give rise to the same stability as the completely filled H 1s related band for the dihydride (open rectangles Fig. 5.2b). Accordingly the formation of YH_2^{tetra} is naturally preferred. The occupation of both, tetrahedral and octahedral sites then induces a new band, which overlaps only slightly with the Y d-band manifold. In this sense, YH_3 is an "almost" insulator.

Since experimental probes of the occupied band structure in general do not detect major insufficiencies of the LDA band structure for the dihydride phase, it would be now quite tempting to ascribe the shortcomings of LDA to an insufficient description of H in octahedral sites. In terms of the many-body theoretical model of Ng et. al.[3] for the related LaH_x system this is only partially correct. If one compares their band structure for LaH_2 and LaH_3 one notices as a major difference to the LDA based band structures a flattening (localization) of LDA bands. For the dihydride this affects primarily an un-

occupied t_{2g} band, which does not give rise to a major change in the physical properties of the material. On the other hand for the trihydride, the flattening of the uppermost H related band leads to the aforementioned opening of a gap. One expects in this framework, that correlation effects are especially strong for the trihydride phase, since the calculated renormalization parameters of the overlap integrals are much larger for the interaction between H in tetrahedral and octahedral sites, compared to the coupling parameters via metal d-states. Nevertheless the many-body band structure for the dihydride is modified compared to the LDA case as well. The correlation effects are simply not "visible" as they do not lead to a gap opening.

One could then ask, whether the dihydride phase is important at all for the switching of the material or if it (in light of its natural occurrence for all heavy rare earths) even acts as a precursor state? We believe yes and one important feature turns up in our presented calculations. It is the hydrogen induced change of the d-band character at E_F . The strong interaction of tetrahedral hydrogen with t_{2g} d-bands leads to a FS which is comprised of states with strong e_g character. These states were shown to heavily interact with octahedral hydrogen states, as they are provided during the dihydride \rightarrow trihydride transition. One is tempted to interpret the fcc dihydride phase with a partially occupied e_g band as the natural template for hydrogen absorption in octahedral sites, which annihilates large parts of the dihydride FS. An "almost-insulator" state with a rather unstable partially filled H 1s related band (filled rectangles in Fig. 5.2c) is therefore reached and the various scenarios for the Me-I transition might or might not take place. This interpretation is supported by the natural occurrence of the dihydride phase for all the rare earths.

5.5 Conclusion

We have presented *ab-initio* calculations for Y, $\text{YH}_2^{\text{tetra}}$, YH_3 and $\text{YH}_1^{\text{octa}}$ all in the fcc structure. We found important changes in the spherical harmonics decomposition of the charge density at E_F upon hydrogenation. We identify the $\text{YH}_2^{\text{tetra}}$ phase as the natural precursor for the trihydride formation. The observation of the transition from a t_{2g} derived Y FS to an e_g derived $\text{YH}_2^{\text{tetra}}$ FS is an achievement of band theory and presents an extension of the simple ionic picture, which *a priori* does not distinguish between hydrogen in octahedral and tetrahedral sites.

Acknowledgements We are greatly indebted to our workshop and electric engineering team. Financial support by the Fonds National Suisse pour la Recherche Scientifique is gratefully acknowledged.

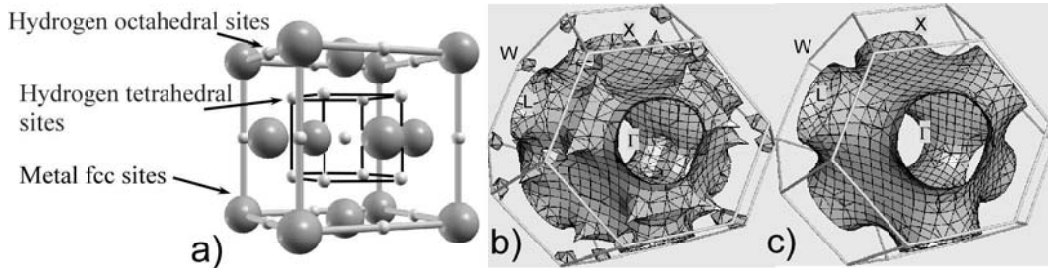


Figure 5.1: a) fcc lattice with occupied octahedral and tetrahedral sublattices. b) FS for fcc Y and c) YH₂

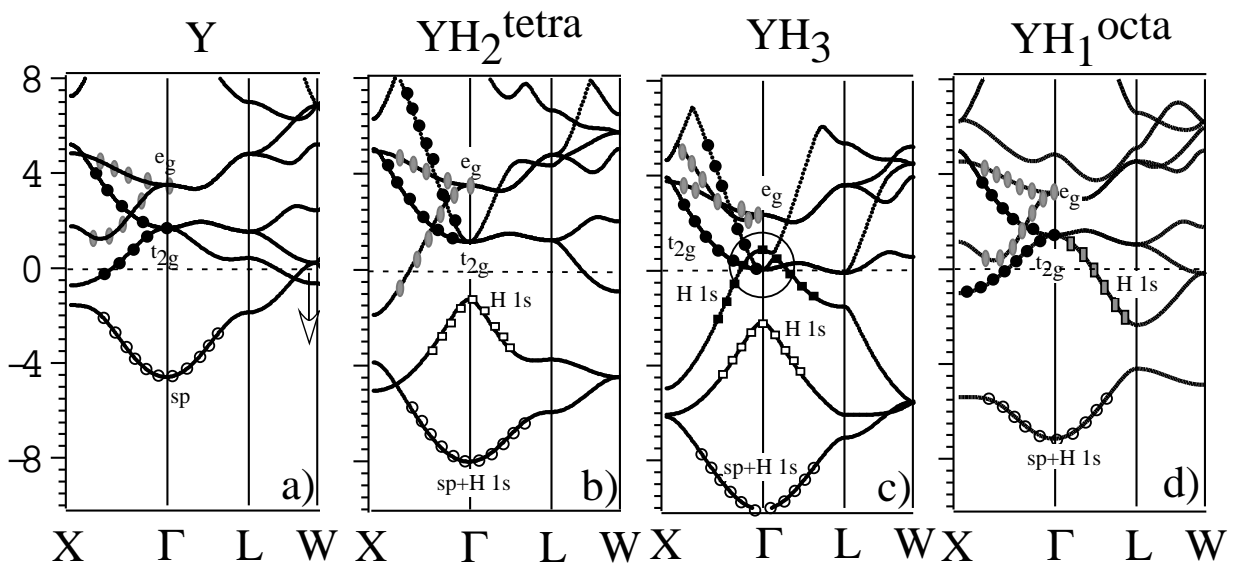


Figure 5.2: Band Structure along high symmetry directions for a) fcc Y b) fcc YH₂^{tetra} c) fcc YH₃ d) fcc YH₁^{octa}. Different symbols represent different orbital character (see text).

Bibliography

- [1] J.N. Huiberts, R. Griessen, J.H. Rector, R.J. Wijngaarden, J.P. Dekker, D.G. de Groot, and N.J. Koeman. *Nature*, 380:231, 1996.
- [2] P.J. Kelley, J.P. Dekker, and R. Stumpf. *Phys. Rev. Lett.*, 78:1315, 1997.
- [3] K.K. Ng, F.C. Zhang, V.I. Anisimov, and T.M. Rice. *Phys. Rev. Lett.*, 78:1311, 1997.
- [4] R. Eder, H.F. Penn, and G.A. Sawatzky. *Phys. Rev. B*, 56:10115, 1997.
- [5] P. van Gelderen, P. A. Bobbert, P.J. Kelly, and G. Brocks. *Phys. Rev. Lett.*, 85:2989, 2000.
- [6] P. van Gelderen, P. A. Bobbert, P.J. Kelly, G. Brocks, and R. Tolboom. *Phys. Rev. B*, 66:075104, 2002.
- [7] T. Miyake, F. Aryasetiawan, H. Kino, and K. Terakura. *Phys. Rev. B*, 61:16491, 2000.
- [8] A.C. Switendick. *Sol. State Comm.*, 8:1463, 1970.
- [9] P. Blaha, K. Schwarz, , G.K.H. Madsen, D. Kvasnicka, and J. Luitz. 2001. Wien2k, An Augmented Plane Wave + Local Orbitals Program for Calculating Crystal Properties (Karlheinz Schwarz, Tech. Univ. Wien, Austria) ISBN 3-9501031-1-2.
- [10] Pearson. *Pearson's Handbook of Crystallographic Data for Intermetallic Phases*. American Society for Metals, Metals Park, OH 44073, 3000.
- [11] C. Koitzsch. unpublished.

Chapter 6

Fermi Surface Topology of Rare Earth Dihydrides

C. Koitzsch², J. Hayoz¹, M. Bovet¹, F. Clerc², L. Despont², C. Ambrosch-Draxl³, and P. Aebi²

¹*Université de Fribourg, Institut de Physique, Perolles, CH-1700 Fribourg, Switzerland*

²*Institut de Physique, Université de Neuchâtel, CH-2000 Neuchâtel, Switzerland*

³*Institute of Theoretical Physics, Karl-Franzens-University Graz, Universitätsplatz 5, A-8010 Graz, Austria*

Phys. Rev. B, 70, 165114 (2004).

Abstract: We report high resolution angle-resolved photoemission experiments on epitaxial thin films of different rare earth (RE) dihydrides (RE=Gd,La) and of YH₂ and ScH₂. It is found through *ab-initio* calculations and confirmed by Fermi surface mapping that the electronic structure becomes very similar upon hydrogenation, rendering the studied dihydrides isoelectronic. We propose that the dihydride phase acts as a common precursor state for the formation

of the insulating trihydride phase. For states with higher binding energies (which exhibit considerable H character) the agreement between calculation and measurement is less convincing. Independent of the difficulties to describe these hydrogen related states, we note in the comparison between experiment and calculation a very convincing description of the Fermi surface for the dihydrides. Therefore we trace the apparent inability of density functional theory to describe the hydrogenation up to the trihydride phase to an insufficient description of hydrogen states in general and in particular involving octahedral sites.

6.1 Introduction

The valence electronic structure of rare earth hydrides is both fundamentally interesting and technologically important. Fundamentally interesting, because one finds interesting phenomena, e.g. electronic and magnetic ordering and metal-insulator (Me-I) transitions for a whole class of materials[1], hence allowing the possibility to study these effects for different hydrogen concentrations and various metallic host lattices. Initiated by potential applications, the phase transition between the dihydride and trihydride phase received recently tremendous interest, since the structural transition between the fcc dihydride and the hcp trihydride (exception is LaH_{2+x} which remains cubic) is accompanied by a spectacular change in the optical properties. The so called "switchable mirror" transition for the reversible phase change from a metallic reflecting dihydride to a transparent insulating trihydride was first described by Huijberts et. al. [2] for YH_x and LaH_x . The search for other reliable and fast switching materials beside the original systems revealed an astonishing diversity of materials for which a hydrogen induced Me-I transition occurs, basically comprising the whole rare earths, but also lighter materials such as Mg [3] and different ternary compounds. The apparent universal nature of the Me-I transition upon hydrogenation is one of the motivations to investigate in this work the electronic structure of the metallic dihydride, which can be perceived as a *precursor phase*. We report on high resolution angle-resolved photoemission (ARPES) experiments on epitaxial thin films of different rare earth dihydrides ($\text{GdH}_2, \text{LaH}_2$) and of YH_2 and ScH_2 . In the following, for argumentative simplicity, Y and Sc are referred to as rare earths (RE) as well.

The aforementioned insulating trihydride phase posed a very demanding

challenge for modern electronic structure calculations. *Ab-initio* calculations with the local density approximation (LDA) were unable to reproduce the insulating ground state at all. Only a structural deviation [4],[5] led to a small gap via a symmetry lowering. The discrepancy in gap size between calculation and the experiment [6],[7] is comparable to known strongly correlated systems and different models were proposed, which ascribed the Me-I transition to strong electron correlations on H sites [8],[9]. Recently GW calculations were able to reproduce the experimental gap and it was claimed, that the insulating trihydride is similar to a conventional semiconductor [10],[11],[12]. From a practical point of view it seems that the GW calculations only lead to a shift of LDA bands with no significant modifications in terms of band width or band topology. It is at present still unclear, where the limitations of LDA are and if there is a general recipe how to correct LDA results. It is therefore very interesting to test LDA for the dihydride phase, which is still metallic (therefore presumably accessible with LDA) but can be viewed in a simplified view as a hydrogen deficient trihydride. We therefore utilized an *ab-initio* augmented plane wave plus local orbital (APW+lo) code [13] with the generalized gradient approximation (GGA) [14] to calculate the electronic structure and compare it to the experimental ARPES results.

The paper is organized as follows. The next section deals briefly with the experimental setup and the sample preparation. Furthermore the employed APW+lo *ab-initio* electronic structure calculations are described. The main section III gives an introduction into the electronic structure of rare earth dihydrides based on band structure calculations. Already existing models are briefly discussed in this context. Furthermore we present the angle-resolved photoemission data for the different rare earth hydrides and focus on YH₂ for an in-depth comparison to computationally obtained results. In section IV we discuss our findings in a more general context and comment on the recent debates about the Me-I transitions and various structural and magnetic ordering phenomena in this class of materials. The paper finishes with conclusions in section V.

6.2 Experiment and Calculation Details

The preparation of contamination-free single crystalline dihydride films imposes stringent requirements in terms of base pressure during evaporation of the pure metals and hydrogen gas purity due to the strong affinity to oxygen and

the subsequent undesired formation of surface or even bulk oxide. Therefore we took the utmost care in outgassing the water-cooled e-beam evaporator ensuring that evaporation was achieved below $4 \cdot 10^{-10}$ mbar. 200 Å of metal were evaporated in a hydrogen pressure of $4 \cdot 10^{-6}$ mbar on a clean W(110) single crystal held at 500 K. The utilized hydrogen was filtered through a Pd-Ag permeation tube [15]. The resulting films are single crystalline. Low energy electron diffraction (LEED) shows no superlattice spots, just a 1x1 surface unit cell with lattice parameters equal to the bulk values within the experimental error of ± 0.3 Å. The film thickness of 200 Å is sufficient to exclude any quantum size effects [16],[17] and should allow for a sufficient strain release.

The photoemission experiments were performed immediately after film growth, *in-situ* in a modified VG ESCALAB Mk II spectrometer with a base pressure lower than 10^{-10} mbar. Surface cleanliness was ensured by the absence of O 1s and C 1s core level emission in the X-ray photoelectron spectrum employing Mg K_α radiation. The angular dependence of emission from metal core levels over the full hemisphere was measured via rotating the sample with a two-axis sample goniometer enabling sequential computer-controlled sample rotation [18],[19]. This measurement mode is commonly called X-ray photoelectron diffraction (XPD), for a review see e.g. [20]. All prepared films were found to exhibit fcc stacking with two domains, both oriented in (111)-direction but rotated 180° with respect to each other. The fcc crystal structure immediately confirms the preparation of the dihydride phase. We could not detect traces of hcp stacking, which translates the hydrogen content close to a stoichiometric dihydride. Nevertheless, a partial occupation of octahedral sites and/or the existence of tetrahedral vacancies cannot be ruled out completely. Details of the structural analysis via X-ray photoelectron spectroscopy and -diffraction are not presented here, the interested reader is referred to [21]. The ARPES measurements were performed via sequential angle-scanning data acquisition. The accuracy and efficiency of this method was demonstrated for two- [22] and three-dimensional [23] materials. The obvious advantage of this method is the uniform sampling density over a wide range of k-space and hence a global view of direct transitions crossing E_F . The experimental procedure was outlined in [23] and the reader is referred to this work for details. We furthermore present conventional E(k) scans, which are restricted to the $[\bar{\Gamma} \bar{M}]$ high symmetry direction covering an energy window of 7.48 eV. These measurement modi are complementary in terms of range in k-space and energy and provide a global and yet detailed view of the electronic structure in the vicinity of the Fermi level.

All presented measurements were obtained using monochromatized He I radiation [24], the combined angular resolution of sample manipulator and energy analyzer is approximately 1° and the energy resolution 50 meV. All calculations rely on the published structural data from Pearson [25]. The electronic structure calculations are based on Density Functional Theory (DFT) and the APW+lo code Wien2k [13] was employed. There the unit cell is divided into non-overlapping atomic spheres (muffin tin) and an interstitial region [26]. In the muffin tin region the basis functions are comprised of atomic-like wavefunctions while the interstitial region is described with plane wave basis functions. A muffin tin radius for rare earth atoms and hydrogen atoms of 1.16 Å and 0.85 Å was assumed, respectively. Self consistency was judged to be, when the total energy change was less than 0.1 mRy in subsequent cycles. The calculation was based on 10000 k-points, which corresponds to 286 k-points in the irreducible wedge of the Brillouin zone (BZ).

6.3 Experimental and Theoretical Results

6.3.1 General electronic properties of (Sc,Y,Gd,La) - dihydrides

The electronic structure of RE dihydrides and their related compounds YH₂, ScH₂ was already investigated more than 20 years ago by photoemission [27], [28], [29]. These studies employed poly-crystalline samples and hence only the effects of hydrogenation on the density of states were investigated. These experiments were combined with theoretical calculations [30],[31],[32],[33]. In order to allow for a comparison of our LDA results with already published calculations, we show in Fig. 6.1 conventional band structure plots based upon converged calculations for the studied compounds. A very good agreement to the aforementioned older calculations is achieved. This points to an apparent robustness of the band topology in terms of technique and self consistency, since older calculations are often not self consistent and/or use different basis sets. Nevertheless small shifts in the relative positions of bands are possible.

The band structures, presented in Fig. 6.1 are very similar. One notices three bands below the Fermi level, marked with 1,2 and 3 for the case of ScH₂ in Fig. 6.1 a). The pioneering calculation of Swietendick [30],[31] already attributed d-like metallic character to band one, hydrogen antibonding character to band two and mixed metal-hydrogen (Me-H) character to band three. The

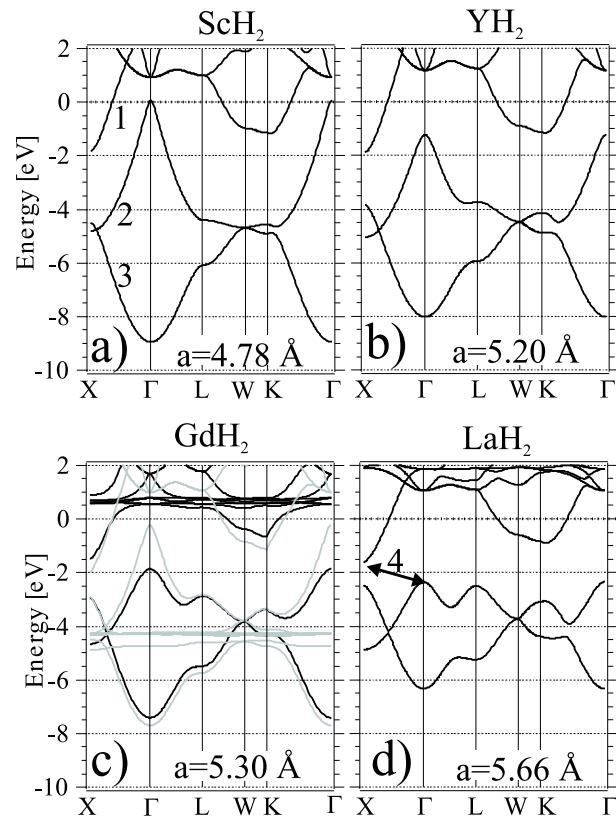


Figure 6.1: Band structure along high symmetry directions for a) ScH₂ b) YH₂ c) GdH₂ and d) LaH₂; one notices three bands labelled 1,2 and 3 with an indirect gap respectively overlap between band 1 and band 2 marked as feature 4 in d). The calculation for GdH₂ is spin polarized in order to avoid a placement of the 4f levels at the Fermi level, the majority bands are shown in grey.

nature of bonding in these compounds must be discussed in terms of interaction between metal d-states and hydrogen 1s states. Metal sites are surrounded by 8 hydrogen atoms situated on tetrahedral sites in the fcc lattice. The atomic environment of the metal sites is comprised of a cube with hydrogen atoms at the cube corners and the metal atom at the center. An equal occupation of the three t_{2g} orbitals, which is required by the cubic symmetry, leads to charge maxima along the cube diagonals, the [111]-direction. By the same argument one can correlate the remaining two e_g orbitals with bonding orbitals to octahedral sites, which are unoccupied in the dihydride phase[33]. The formation of a Me-H bonding band with a binding energy at Γ between -6 and -9 eV poses the question of ionicity of this bond. Charge transfer analysis [33] points to an effective charge transfer away from the metal site to the tetrahedral hydrogen sites.

If one compares the band structure of the different dihydrides, one notices subtle differences. The bandwidth of hydrogen related bands (band two and three in Fig. 6.1) increases with decreasing lattice constant. While there is an indirect gap of 0.73 eV between band two at Γ and band 1 at X for the alloy with the largest lattice constant LaH_2 , marked as feature 4, there is considerable overlap of 0.65 eV for YH_2 and 1.89 eV for ScH_2 between band one and band two. It is interesting to note that the position of band one with respect to the Fermi level does not significantly change for the different alloys. In contrast, the maximum of the hydrogen antibonding band at Γ moves away from the Fermi level to larger binding energies for increasing lattice constants. This shift leads finally to the aforementioned indirect gap of 0.73 eV between band 1 and band 2 for LaH_2 . Band 3 exhibits an opposite trend, here the band minimum at Γ shifts upwards from a binding energy of -8.9 eV for ScH_2 to -6.3 eV for LaH_2 . The observed increase of bandwidth with decreasing lattice constant supports the proposed assignment of antibonding and respectively bonding character to band 2 and band 3. The increased bandwidth for small lattice constants can then be understood as an increased level spacing for decreasing separations.

In order to confirm this presumed lattice constant scaling, band structure calculations for ScH_2 with different lattice constants were performed. The results (not shown) confirm this assumption. It seems that the band structure for hydrogen related states can be tuned quite freely by changing the lattice constant, but the metal derived d-band remains rather unaffected. Based on these band structures one expects very similar Fermi surface topologies for the different dihydrides since band one is solely responsible for the Fermi surface,

with the exception of ScH₂, where the calculation yields a small pocket at Γ derived from the hydrogen related band 2. We are not concentrating on the implications of this small pocket on the electronic structure of ScH₂ since our measurement geometry is not sensitive to k-points exactly at Γ , as it will be shown later and as it would be necessary to confirm this point. In the following we concentrate on band 1. There one sees a Fermi level crossing between Γ and X and between Γ and K and between L and W. One does not observe a Fermi level crossing between Γ and L. This points to a connected Fermi surface, where the necks extend along the Γ L-direction, hence one does not observe a crossing in this direction. This will be discussed in more detail in conjunction with the experimentally obtained Fermi surface maps.

6.3.2 Experimental Data and Calculation

The following discussion of the electronic structure takes mainly place in reciprocal space, in the surface Brillouin zone (SBZ). Fig. 6.2a) shows the SBZ for an fcc (111) orientated surface, the scale is adapted to YH₂. The various high symmetry points originate from a projection of the 3D bulk BZ onto the surface. For the specific $\bar{\Gamma}$ \bar{M} -direction, the Γ KLUX plane is projected onto the surface, as it is shown in Fig. 6.1b). It becomes obvious, that the a priori inequivalent \bar{M} and \bar{M}' points stem from a projection of the X respectively L point of the bulk BZ. This inequivalency is lifted for our measurement geometry, because the photoemission signal is integrated over two film domains. The second film domain is rotated 180° with respect to the first. The bulk BZ of this second domain is shown in grey and is constructed via a rotation around the (111) axis. As a result of this rotation the \bar{M} and \bar{M}' points become indistinguishable. A photoemission experiment allows for an exact determination of the band dispersion $E(k_{\parallel})$ in the SBZ, due to the conservation of the parallel wave vector component, k_{\parallel} , in the photoemission process. The perpendicular wave vector component, k_{\perp} , is less well defined and its reconstruction is based on the free electron final state (FEFS) assumption. Here one assumes for the photoemission final state a free electron parabola. This assumption appears adequate for the reconstruction of the perpendicular wave vector component for excitations in the employed energy range[23]. Within this approximation, energy and momentum conservation correspond to spherical cuts through the three dimensional BZ. The radius of the cut, k_0 , is determined via equation (6.1) by the photon energy ($\hbar \cdot \omega = 21.2\text{eV}$), the inner potential V_0 , the work-

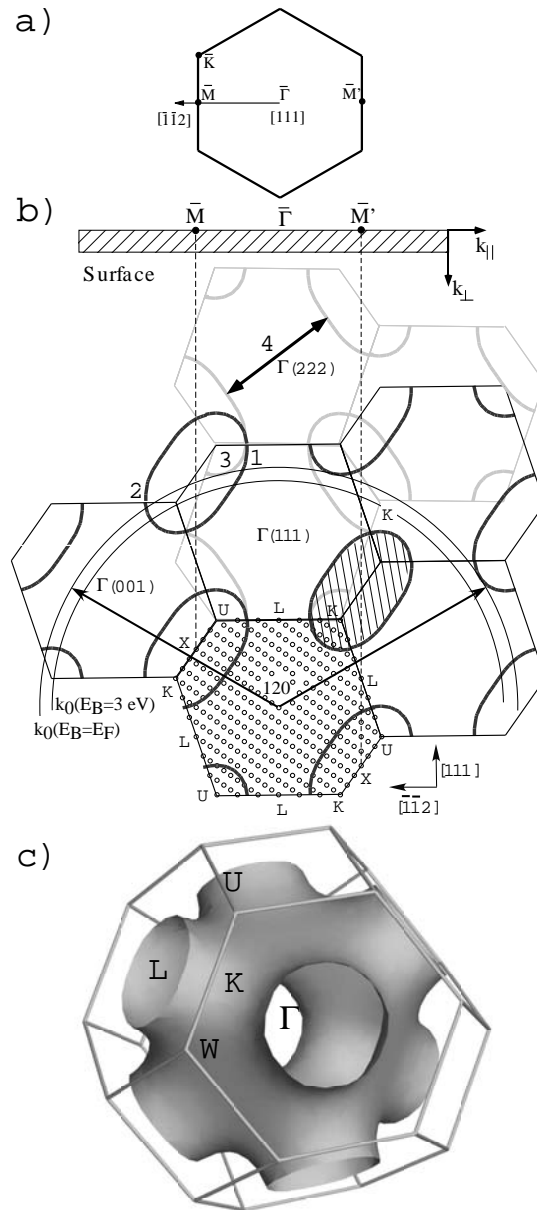


Figure 6.2: a) surface Brillouin zone for YH₂. b) Side view of the BZ for a fcc structure in the Γ KLUX plane and its relation to the surface Brillouin zone for a [111]-oriented crystal. Free electron final state model in an extended zone scheme for YH₂. The free electron final state spheres ($V_0=13 \text{ eV}$, $\phi=3.1 \text{ eV}$) are drawn for the Fermi energy and a binding energy of -3 eV . Shown in thick black is the Fermi surface contour, which was obtained via calculating the eigenstates on a cubic k-space grid, which is shown with open circles. The occupied region is shown hatched for one pocket. Features one, two and three denote regions of coincidence between the free electron final state of E_F and the Fermi surface contour. Feature four shows a possible Fermi surface nesting vector (see text). Contributions of a second domain are shown in grey. c) Fermi Surface and bulk BZ

function ϕ and the probed initial state energy E_B .

$$k_0 = 0.51 \cdot \sqrt{\hbar \cdot \omega - |E_B| - |\phi| + |V_0|} \quad (6.1)$$

$$k_{\parallel}(\theta) = 0.51 \cdot \sqrt{\hbar \cdot \omega - |E_B| - |\phi|} \cdot \sin[\theta] \quad (6.2)$$

k_0 and k_{\parallel} are the length of the FEFS wave vector in the solid and the conserved parallel wave vector component, respectively. Equations (1) and (2) are such that energies are in [eV] and wave vectors in [\AA^{-1}].

If one varies the photoelectron detection angle θ , one follows the corresponding FEFS sphere and automatically samples different states along the FEFS sphere in the BZ. One notices in Fig. 6.2b), that a scan in the SBZ corresponds only superficially to a high symmetry direction in the bulk BZ. The discrete nature of the photon energy restricts the k-space sampling to a certain region in k-space. The exact k-space location is determined by the radius of the FEFS sphere and the dimensions of the BZ of the material. The FEFS sphere is determined via equation one and extends beyond the first BZ, hence we work in an extended zone scheme. Inscribed are FEFS spheres for initial states at the Fermi level and for a binding energy of -3 eV. Regarding the remaining parameters, we use reasonable values for the workfunction and the inner potential of $\phi=3.1$ eV and $V_0=13$ eV, respectively. Shown in black (grey for the mirror domain) is furthermore a calculated Fermi surface contour, which is based on a grid in k-space, where the grid points are shown as open circles.

If one measures the energy distribution of photoelectrons, which are emitted normal to the surface, one samples a region in k-space between Γ and L. Fig. 6.2b) shows, that the FEFS is found between Γ and L. For increasing emission angles, various other high symmetry lines are crossed. Special emphasis is drawn to the Γ K X and Γ L line in the extended zone scheme, which will be later employed to compare experimental data and theoretical data along high symmetry lines in more detail. If one compares the FEFS sphere and the corresponding constant energy surface for a specific binding energy one expects high photoemission intensities if the two coincide. Specifically for e.g. the Fermi energy, this would be the case around the points one and two (Fig. 6.2b), where the final state sphere cuts through the Fermi surface contour and around region three, where the Fermi surface is for a large k point range in the immediate vicinity of the FEFS sphere.

Fig. 6.2c) shows a three dimensional representation of states at the Fermi level, based on the same potential that was utilized to generate the Fermi energy contour in Fig. 6.2b). A three dimensional contour plot [34] in k-space of states at the Fermi energy correspondingly yields the three dimensional Fermi surface. Clearly visible are the open necks along the Γ L-direction. The discussed Fermi surface is a hole surface, which means that the occupied states are concentrated around the X-point and not around the Γ point, as it is common for the free electron metals. The occupied region is hatched for one pocket in Fig. 6.2b) and correspondingly in Fig. 6.2c) the occupied regions are found between the calculated Fermi surface and the various Brillouin zone boundaries .

Experimentally these Fermi surface contours can be probed via measuring the angular dependence of the photoemission intensity originating from states at the Fermi level. In Fig. 6.3 we present so-called Fermi surface maps for the studied dihydrides, which were obtained at room temperature. The intensity of He I excited photoelectrons, with energy centered at E_F , was mapped via equation 2 to k_{\parallel} . The outer circle corresponds to a polar angle of 90° , and the center of the image represents normal emission. Intensities are linearly color coded, high intensities (in white) result at k_{\parallel} locations, where direct transitions move through E_F . The mapping corresponds to a section through the Fermi surface perpendicular to the [111]-direction, as has been demonstrated for the example of Cu [23] and sketched for YH₂ in Fig 6.2b). All Fermi surface maps show a 6-fold symmetry. The apparent doubling of symmetry compared to the trigonal [111]-axis is due to the existence of the aforementioned two domains, which are rotated 180° with respect to each other.

The most prominent feature of the presented Fermi surface maps is an almost circular feature centered around the $\bar{\Gamma}$ point, in the middle of each image. The exact dimensions of this feature vary slightly. In general one observes a Fermi surface crossing, displayed as region of high intensity between 11° and 14° . This corresponds via equation 2 to 0.4 to 0.5 \AA^{-1} . A very similar feature is sampled in the second surface BZ as well, noticeable as half circles in the outer parts of the map. One observes it only partially due to the limited k-range via excitation with He I radiation. Moreover a clear drop in intensity at the \bar{K} point can be recognized. Besides this, one notices a general high background intensity, especially in k-space between the ring-like central part and the boundaries of the SBZ with additional slight intensity variations. The underlying band dispersion, which leads to the intensity enhancement at the Fermi level is investigated via complementary high resolution scans along high

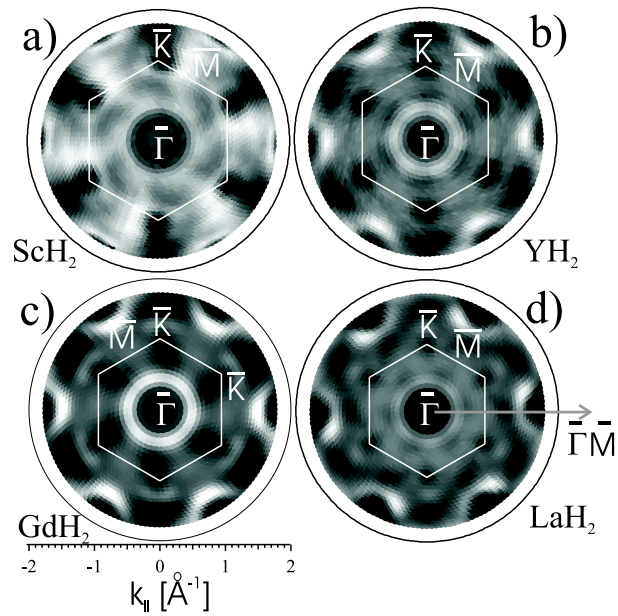


Figure 6.3: Fermi surface maps measured with He I radiation, high intensities are shown in white, outer ring corresponds to 90° emission, center corresponds to normal emission, all intensities are shown in parallel projection, the raw data are symmetrized and divided by a background of Gaussian shape; the high symmetry points and the SBZ are indicated. The size difference of the SBZ originates from the different lattice constants. a) ScH₂ b) YH₂ c) GdH₂ d) LaH₂

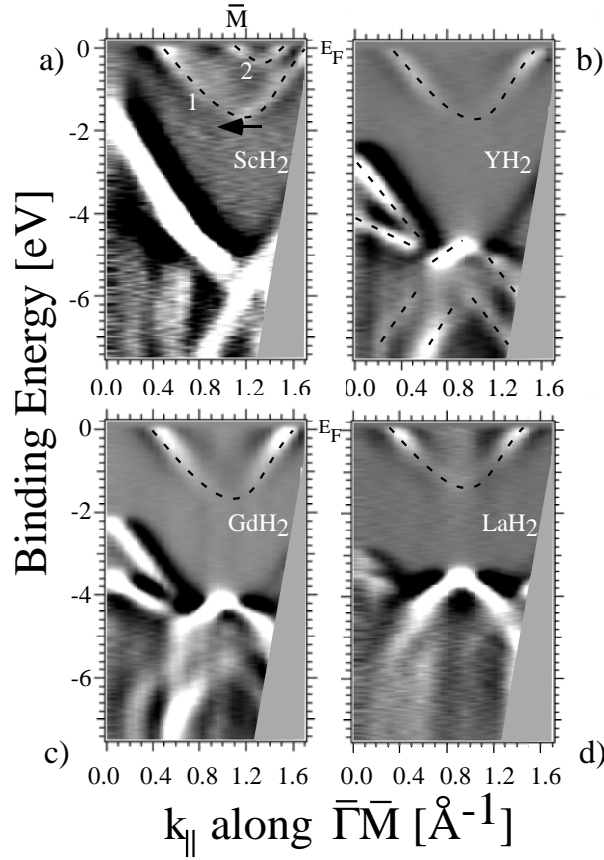


Figure 6.4: Second derivative of experimental momentum distribution curves a) ScH_2 b) YH_2 c) GdH_2 d) LaH_2 , colorcoded such that white corresponds to high intensity, the dashed lines serve as guide to the eye

symmetry directions of the SBZ. For this purpose we recorded 31 photoelectron spectra in a range between 0° and 60° along the $\bar{\Gamma}-\bar{M}$ -direction (as indicated by an arrow in Fig. 6.3d). For this direction we measured the photoelectron intensity not only at the Fermi level but for binding energies between 0.2 and -7.48 eV. The data sets were mapped onto a regular (E_i, k_{\parallel}) grid. In Fig. 6.4 the second derivative of the corresponding momentum distribution curves are visualized as grey scale plots with white corresponding to maximum intensity. The reason for taking the second derivative is a contrast enhancement (typical spectra are displayed in Fig. 6.6 below).

The obtained $E(k)$ plots (Fig. 6.4) are complementary to the measured

Fermi surfaces in terms of being able to analyze more thoroughly the origin of enhanced intensity at the Fermi level. For the $\bar{\Gamma}$ \bar{M} -direction we can therefore assign a band to the observed circular feature in the Fermi surface maps. This band cuts the Fermi level at approximately 0.4 \AA^{-1} and then disperses towards higher binding energies with increasing parallel wave vector component. It exhibits a clear minimum at the SBZ boundary, at the \bar{M} point. The band and its minimum is marked in Fig. 6.4a) as feature 1. We find a binding energy of approximately -1.6 eV at the extremal point. The k-space location of this minimum is different for the different compounds, since the different lattice constants manifest themselves in different SBZ dimensions, $k = \frac{2\pi}{a}$, ranging from 1.31 \AA^{-1} to 1.11 \AA^{-1} . This effect becomes apparent in the Fermi surface maps, as a zoom-out impression, when comparing ScH₂ and LaH₂. Correspondingly one notices in the electron distribution curves a horizontal shift of the band minimum to lower k_{\parallel} values (indicated in Fig. 6.4a) with an arrow). Furthermore one notices for ScH₂ and LaH₂ additional regions of high intensity close to the Fermi level in the inside of the aforementioned band, close to the \bar{M} point. This feature is labelled as 2 for ScH₂. These additional intensities are different for the investigated compounds. For ScH₂ an almost empty electron pocket becomes visible in the electron distribution curves (marked as feature 2). A very similar feature appears (though markedly weaker) for LaH₂ as well.

In order to facilitate a more in-depth comparison between experimental and theoretical results, one has to consider the measurement geometry and the FEFS model in conjunction with the theoretical band structure. For the states at the Fermi level one can immediately interconnect the FEFS sphere and its relation to the computed Fermi surface contour. For states with higher binding energy one can eventually compute the theoretical dispersion relation within this FEFS model for a comparison to experimental E(k) curves.

We concentrate on YH₂ for the calculations but stress the applicability to ScH₂, GdH₂ and LaH₂. Following the previous discussion about the bandstructure, one notices that only one band (exception ScH₂, where the calculation yields a small contribution from band 2, see Fig. 6.1a) contributes to the Fermi surface. Direct transitions are now expected for k-points, where the FEFS sphere coincides with the Fermi surface in the extended zone scheme, as shown in Fig. 6.2b).

The corresponding circle cuts the Fermi surface contour at the points labelled as 1 to 3. Initial states of k-space region one (Fig. 6.2b) yield the primary circular feature around the $\bar{\Gamma}$ point. The crossing between FEFS circle

and Fermi surface contour at point 2 in Fig. 6.2b) yields the semi circle in the second SBZ. Furthermore the FEFS sphere coincides with the Fermi surface around region three. These points simultaneously appear for the $\bar{\Gamma}$ \bar{M} and the $\bar{\Gamma}$ \bar{M}' -directions due to the existence of two mirror domains. Hence one observes in between point one and two an additional increase of photoemission intensity due to initial states at point three. It has to be pointed out, that in this region the choice of the FEFS parameters are quite crucial, since the sphere and the contour barely touch each other. This peculiar topology is responsible for the additional intensity around the \bar{M} point. Since the FEFS does not cut but merely touches the initial state contour, one expects not sharp transition but more a diffuse background for this region, as it is indeed observed experimentally (Fig. 6.3). With regard to the slight deviations between the investigated dihydrides, we have to assume that they stem primarily from effects due to the measurement geometry and due to the free electron final state assumption and are not signs of principal differences of the band structure in this energy region.

Via the FEFS model one can plot the eigenvalues of the appropriate k-points for a measurement in $\bar{\Gamma}$ \bar{M} -direction and obtain computationally a conventional $E(k)$ relation. The corresponding computed energy distribution curves (Fig. 6.5b) correspond very nicely in the energy range between 0.2 to -2 eV to the measured curves of Fig. 6.5a. The topology of the sampled band is nicely reproduced. At the \bar{M} high symmetry point of the SBZ, states in the environment of the X point of the bulk BZ are sampled. This particularly holds true for states at E_F , while for states at $E_B = -3$ eV k points in the vicinity of L and K are sampled (compare to Fig. 6.2b). Our combined measurements (Fig. 6.4) clearly indicate that the observed d-bandwidth is constant for the measured dihydrides. This finding is theoretically very well reproduced. We find a binding energy of -1.6 eV, which is in excellent agreement to the position of band 1 at the X-point in Fig. 6.1.

With regard to the sampling of this band, we notice the appearance of a second feature (labelled as 2+ in Fig. 6.5b) which is due to the existence of a second mirror domain (especially for ScH₂ and LaH₂), we notice the appearance of a second feature (labelled as 2+ in Fig. 6.5b). The exact location in energy and momentum is very dependant on the parameters of the FEFS and therefore leaves ample room to maintain the picture of an isoelectronic Fermi surface for the dihydrides, despite slight differences in the measurements.

In terms of testing the LDA band structure we have not discussed so far the hydrogen related bands, which are not in such close proximity to the Fermi

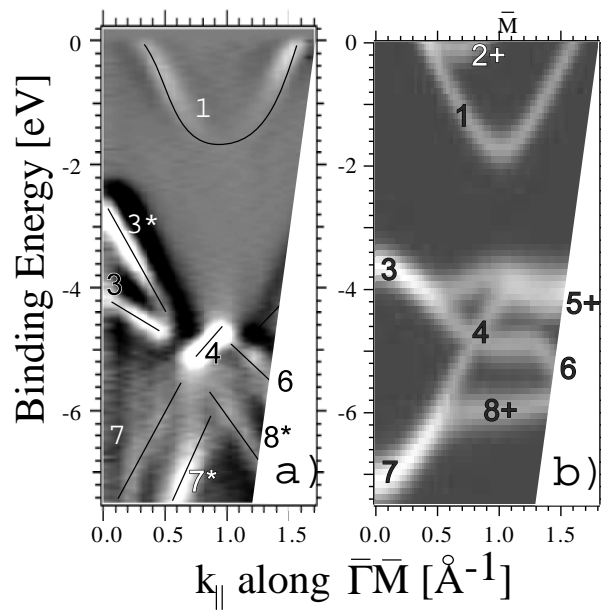


Figure 6.5: Experimental and theoretical $E(k)$ for YH_2 . a) Second derivative of experimental $E(k)$ distribution curves b) theoretical $E(k)$ distribution, eigenvalues were computed on a k -grid, which is adapted to the experimental $E(k)$ distribution curves, both inequivalent domains (see text) are considered.

level. The band structure calculations predict two additional bands at higher binding energies, which have been labelled band 2 and band 3 in Fig. 6.1. The application of the FEFS model places these bands at -3.6 eV and 7.2 eV for normal emission (bands 3 and 7 in Fig. 6.5b). Subsequently if one follows the dispersion along the $[\bar{\Gamma} \bar{M}]$ -direction, the two bands split up in up to 4 bands, an effect which again is due to the existence of the aforementioned mirror domain. With regard to the comparison between measurement and theoretical results, we note for this energy range between -2 eV and -7.48 eV a less convincing agreement. It is quite common, that one does not observe theoretical bands in a measurement due to unfavorable photoemission cross-section. We might therefore attribute the absence of the feature 5+ and 8+ in the measurement to such an effect. On the other hand the experimental observation of additional features with respect to theory cannot as easily be discarded. This specifically applies to features 3*, 7* and 8* in Fig. 6.5a), which are not theoretically reproduced. Especially the splitting between feature 3 and feature 3* can be found not only for YH_2 but for GdH_2 and less clearly for LaH_2 as well (Fig. 6.4). The same holds true for feature 7* for YH_2 and GdH_2 and less clearly for LaH_2 . ScH_2 seems to be exceptional in this sense, since it only exhibits one of the respective features.

In order to stress the similarities between the different materials, we present in Fig. 6.6a) electron distribution curves in the vicinity of the \bar{M} point for ScH_2 , YH_2 , GdH_2 and LaH_2 . These spectra were measured at 30° emission angle along the $[\bar{\Gamma} \bar{M}]$ -direction, which translates via equation 2 to 1.08 \AA^{-1} and is in the vicinity of the d-band minimum (feature 1 in Fig. 6.4). The presented spectra in Fig. 6.6a) are therefore part of the already presented energy distribution curves in Fig. 6.4, differing just in the data representation, which is now scaled to the true photoemission intensity and not to the second derivative, as it was the case in Fig. 6.4 and Fig. 6.5a).

One notices again a very similar appearance for all measured dihydrides. The spectra are dominated by a peak at approximately -3.7 eV for LaH_2 and -5 eV for ScH_2 (marked as feature 1 in Fig. 6.6a), which is below the previously discussed d-band minimum (feature 1 in Fig. 6.4). Even further below in energy additional structures (feature 2 in Fig. 6.6) can be distinguished. Emission from these H induced states is very strong. Compared to Fig. 6.4, now due to the intensity scale, almost no structure is found in the region between the Fermi level and -2 eV. As the only feature a small peak is visible at -1.8 eV (LaH_2) and -2.4 eV (ScH_2) and marked as feature three in Fig. 6.6a).

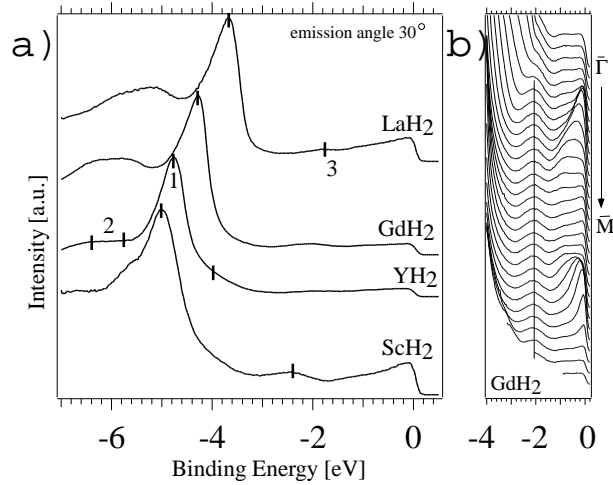


Figure 6.6: a) experimental spectra ScH_2 , YH_2 , GdH_2 and LaH_2 , all measured at an emission angle of 30° . b) ARPES spectra along the $[\bar{\Gamma} \bar{M}]$ -direction for GdH_2 up to an emission angle of 60° .

An inspection of the data set shows that a region of high intensity persists for all dihydrides in this energy range between -1.8 eV and -2.4 eV, and there is virtually no dispersion with the parallel wave vector component. This absence of dispersion is highlighted in Fig. 6.6b), where angle resolved photoemission spectra along the $[\bar{\Gamma} \bar{M}]$ -direction for GdH_2 are shown. The feature does not show up in the plots of Fig. 6.6 because the derivative of the corresponding momentum distribution curves vanishes for nondispersing peaks. Such a non-dispersive behavior is clearly inconsistent with the computed bandstructure, namely bands 1 to 3 in Fig. 6.1 and we tentatively assign this feature to structural imperfections, such as hydrogen in octahedral sublattice and/or tetrahedral vacancies.

We would like to point out that the k-space location around the \bar{M} point represents a best case agreement to the computed band structure. For other k-points (as shown in Fig. 6.4 and 6.5) one observes additional features, whose origins have not been resolved so far. This might be largely due to structural deviations in the hydrogen lattice, which we cannot experimentally exclude and which would certainly affect the hydrogen induced states much more than the previously discussed metal d-states. On the other hand a deviation to the calculated band structure might be a fingerprint of many-body physics, which has already been proposed in the context of the occurring Me-I transition (see

section IV). The comparison between the LDA calculations and the photoemission results is very satisfactory in terms of band position and band topology for the metal derived d-states.

6.4 Discussion

Apparently LDA is quite capable of describing the Fermi surface of rare earth dihydrides, as can be judged from the agreement to the presented measurements. In view of the fact, that the pure elements do not have identical Fermi surfaces, it is especially intriguing that the hydrogenation of these different elements seems to yield a universal dihydride Fermi surface. Without discussing in detail the electronic structure of pure Sc, Y, Gd and La, it has to be considered that the following different properties are generally ascribed to deviating Fermi surfaces. The doubling of the unit cell for La (e.g. its dhcp structure) has been already attributed to a Peierls-type distortion initiated by the removal of a nested part of the Fermi surface [35]. The occurrence of anti-ferromagnetic ordering for Gd-Y [36] alloys and the occurrence of ferromagnetic order for pure Gd has been explained by differences in the nesting properties of the Fermi surface of Y and Gd. Apparently the structural transition between the pure metal and the dihydride removes these differences and yields a universal Fermi surface. It would be certainly highly beneficial to extend these photoemission studies to over- and understoichiometric dihydrides, in order to monitor *in-situ* the establishment and existence range of this universal *precursor* state for the rare earth hydrides.

In accordance to Gupta et. al. [37] for ErH₂ we find experimentally and computationally for all considered dihydrides a multiply connected hole surface, that is comprised of a distorted cube with necks protruding along the Γ L-directions. It is well-known that large parallel sections of a Fermi surface are prone to be annihilated by the formation of a charge/spin density wave[38]. Intuition would point for this Fermi surface to a nesting vector, which connects opposite sides of the cube and hence a nesting vector in [001]-direction (label 4 in Fig. 6.2b). Gupta et. al.[32] quantified this nesting vector with approximately $[0.4, 0, 0] \times 4\pi/a$ for ErH₂. It was pointed out by Liu[39], that the corresponding ordering phenomena for such a nesting vector have so far not been observed in experiments[40]. Liu [39] proposed an alternative nesting vector $[\psi, \psi, 1 - \psi]$, where ψ is a materials dependant parameter. The ordering wave vector arises by considering an extended zone scheme and apparently

complies more with the experimental results. In order to discuss this issue we have integrated the obtained band structure to obtain the generalized susceptibility $\chi(E, \mathbf{k})$, which quantifies the linear electronic response to a perturbation with wave vector \mathbf{q} according to equ. 3 [41].

$$\chi(E, \mathbf{q}) = \int \delta(\epsilon_{\mathbf{k}+\mathbf{q}} - \epsilon_{\mathbf{k}} - E) d\mathbf{k} \quad (6.3)$$

In this expression ϵ is the eigenvalue for a given wave vector \mathbf{k} and \mathbf{q} is the spanning vector between nested parts of the Fermi surface. The band index is omitted since only one band contributes to the Fermi surface. Fig. 6.7a) displays the susceptibility for initial states in the vicinity of E_F (integration over 100 meV) in the [100] plane of YH_2 shown in a greyscale representation, where black corresponds to large values of χ . The calculations were performed for spanning vectors \mathbf{q} between $\mathbf{q}=(0,0)$ and $(1,1)$ (in units of the conventional reciprocal lattice vector $4\pi/a$). A sketch of the Fermi surface contours in the Γ X W K plane is shown as an inset. Fig. 6.7b) shows a cut along the x-axis $(\mathbf{q},0)$ of the same susceptibility matrix.

We note regions of high susceptibility along the lines $(\mathbf{q},0)$ and $(0,\mathbf{q})$ with a maximum (marked with a circle in Fig. 6.7a) for a displacement vector, which corresponds to twice the Fermi wave vector and is close to the proposed value from Gupta [32]. Such a behavior would be consistent with a Peierls like scenario for various ordering phenomena [38]. We have to note however, that the wave vector dependent part of the susceptibility does not exhibit strong fluctuations or a divergence in the calculated plane. The proposed nesting vector does not lead to a pronounced maxima in the susceptibility (Fig. 6.7b). The diagonal contributions to the susceptibility from \mathbf{q} vectors in [110] direction (marked as feature 1 in the inset) are comparable to the contributions in [100] direction. For the [100] direction we note a very high susceptibility for excitations with small \mathbf{q} (feature 3 in inset) compared to the proposed nesting vector (feature 2 in inset). In this sense the Fermi surface is not heavily nested along the principal axis of the warped cube. This fact might explain, why the search for parallel sheaths of the Fermi surface in order to explain experimentally observed nesting phenomena has not been successful so far.

Fermi surface nesting has been proposed for the trihydride phase as well [5] in conjunction with the complicated YH_3 atomic structure. It would be worthwhile to consider the electronic response to the addition of hydrogen atoms in vacant octahedral substitutional sites. First of all one might explain the ordering phenomena in superstoichiometric dihydrides [42] and secondly one

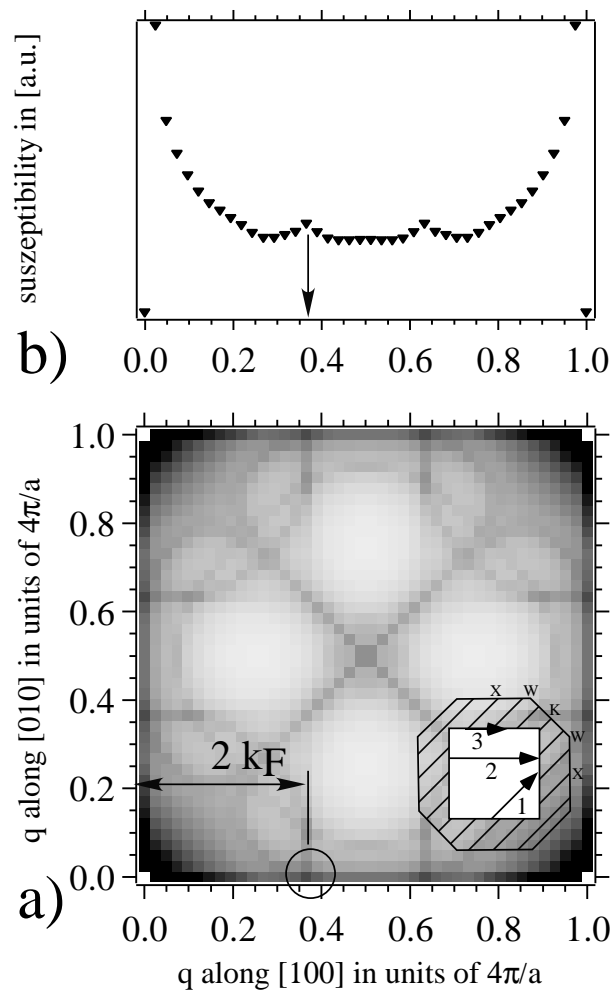


Figure 6.7: Susceptibility in the $[100]$ plane, derived from LDA band structure; greyscale with dark regions corresponding to high susceptibilities

might get more insight into the Me-I transition, which occurs at even higher hydrogen concentration, close to the trihydride phase.

With regard to the still ongoing debate on the origin of the insulating trihydride phase, one finds in the literature two different approaches [43]. One either argues on the basis of standard electron gas theory enriched by strong electron-phonon coupling (weak correlation approach) or one employs strong electron correlations to explain the large band gap of the trihydride phase. The weak correlation proposal certainly suffered from a still ongoing debate about the exact crystallographic structure of YH_3 and the absence of a broken symmetry structure in the twin compound LaH_3 .

Van Gelderen [11],[12] pointed out, that the failure of LDA can be traced back to an incomplete LDA description of the H ground state. This artifact directly stems from deficiency of the local exchange-correlation potential. Surprisingly the here presented data and calculations show a very nice agreement between LDA calculations and the dihydride phase for states in the immediate vicinity of the Fermi level. These bands originate from d-bands, centered at the metal sites. For binding energies below -2eV the agreement between experiment and calculation is less convincing. From a phenomenological point of view it seems that the dihydride phase already exhibits traces of many-electron phenomena but yet still with an unperturbed Fermi surface. Only the addition of octahedral hydrogen leads to a collapse of this Fermi surface and correspondingly to the Me-I transition. Therefore it seems appropriate to pinpoint the failure of LDA to the description of hydrogen in general and in particular involving octahedral hydrogen. This in turn is related to the scenarios of Eder[8] and particularly Ng [9], which assigned a crucial role to octahedral hydrogen. Judging from the observed isoelectronic nature of all dihydrides it is therefore very tempting to understand the dihydride phase as a *precursor* phase for the subsequent formation of the insulating trihydride phase.

6.5 Conclusions

We presented ARPES data on single crystalline [111]-oriented ScH_2 , YH_2 , GdH_2 and LaH_2 thin films on $\text{W}(110)$. It was experimentally shown, that the Fermi surface is very similar for the studied compounds. Most prominent features of the Fermi surface are necks along the ΓL -direction, which originate from a band, which has a minimum at the \bar{M} point at approximately -1.6 eV

binding energy in the ARPES experiments for all the investigated dihydrides. This state is very well reproduced via calculations based on a FEFS model. The observed universal Fermi surface for the measured dihydrides lets us propose that hydrogenation induces a common electronic *precursor* state, namely a common Fermi surface, which is then annihilated for the subsequent Hydrogen induced Me-I transition for the trihydride phase.

Acknowledgements We would like to acknowledge valuable discussions with D. Naumović, O. Gröning and L. Schlapbach. We are greatly indebted to our workshop and electric engineering team, including O. Raetzo, E. Mooser, R. Schmid, R. Vonlanthen, Ch. Neururer, and F. Bourqui. Financial support by the Fonds National Suisse pour la Recherche Scientifique is gratefully acknowledged.

Bibliography

- [1] P. Vajda. *Handbook on the Physics and Chemistry of Rare Earths*, volume 20. Elsevier, Amsterdam, 1995.
- [2] J.N. Huiberts, R. Griessen, J.H. Rector, R.J. Wijngaarden, J.P. Dekker, D.G. de Groot, and N.J. Koeman. *Nature*, 380:231, 1996.
- [3] T. Richardson, J. Slack, R. Armitage, R. Kostecki, B. Farangis, and M. Rubin. *Appl. Phys. Lett.*, 78:3047, 2001.
- [4] P.J. Kelley, J.P. Dekker, and R. Stumpf. *Phys. Rev. Lett.*, 78:1315, 1997.
- [5] Y. Wang and M.Y. Chou. *Phys. Rev. Lett.*, 71:1226, 1993.
- [6] J. Hayoz, C. Koitzsch, M. Bovet, D. Naumovic, L. Schlapbach, and P. Aebi. *Phys. Rev. Lett.*, 83:196804, 2003.
- [7] A.T.M. van Gogh, E.S. Kooij, and R. Griessen. *Phys. Rev. B*, 83:4614, 1999.
- [8] R. Eder, H.F. Penn, and G.A. Sawatzky. *Phys. Rev. B*, 56:10115, 1997.
- [9] K.K. Ng, F.C. Zhang, V.I. Anisimov, and T.M. Rice. *Phys. Rev. Lett.*, 78:1311, 1997.
- [10] T. Miyake, F. Aryasetiawan, H. Kino, and K. Terakura. *Phys. Rev. B*, 61:16491, 2000.
- [11] P. van Gelderen, P. A. Bobbert, P.J. Kelly, and G. Brocks. *Phys. Rev. Lett.*, 85:2989, 2000.
- [12] P. van Gelderen, P. A. Bobbert, P.J. Kelly, G. Brocks, and R. Tolboom. *Phys. Rev. B*, 66:075104, 2002.
- [13] P. Blaha, K. Schwarz, , G.K.H. Madsen, D. Kvasnicka, and J. Luitz. 2001. Wien2k, An Augmented Plane Wave + Local Orbitals Program for Calculating Crystal Properties (Karlheinz Schwarz, Tech. Univ. Wien, Austria) ISBN 3-9501031-1-2.
- [14] J.P. Perdew, S. Burke, and M. Ernzerhof. *Phys. Rev. Lett.*, 77:365, 1996.

-
- [15] J. Hayoz, T. Pillo, A. Zuettel, S. Guthrie, P. Aebi, and L. Schlapbach. *J. of Vac. Sci. Techn. A*, 18:2417, 2000.
- [16] C. Koitzsch. unpublished.
- [17] O. Rader and A. M. Shikin. *Phys. Rev. B*, 64:201406(R), 2001.
- [18] J. Osterwalder, T. Greber, A. Stuck, and L. Schlapbach. *Phys. Rev. B*, 44:13764, 1991.
- [19] D. Naumović, A. Stuck, T. Greber, J. Osterwalder, and L. Schlapbach. *Phys. Rev. B*, 47:7462, 1993.
- [20] C.S. Fadley. *Synchrotron Radiation Research: Advances in Surface Science*, volume 1. Plenum, New York, 1990.
- [21] J. Hayoz, S. Sarbach, Th. Pillo, D. Naumovic, P. Aebi, and L. Schlapbach. *Phys. Rev. B*, 58:R4270, 1998.
- [22] P. Aebi, J. Osterwalder, P. Schwaller, L. Schlapbach, M. Shimoda, T. Mochiku, and K. Kadowaki. *Phys. Rev. Lett.*, 72:2757, 1994.
- [23] P. Aebi, J. Osterwalder, R. Fasel, D. Naumovic, and L. Schlapbach. *Surf. Sci.*, 307-309:917, 1994.
- [24] Th. Pillo, L. Patthey, E. Boschung, J. Hayoz, P. Aebi, and L. Schlapbach. *J. of Electr. Spectr. and Rel. Phenomena*, 97:243, 1998.
- [25] Pearsson. *Pearsson's Handbook of Crystallographic Data for Intermetallic Phases*. American Society for Metals, Metals Park, OH 44073, 3000.
- [26] S. Gotennier. *Density Functional Theory and the family of (L)APW methods: a step-by-step introduction*. 2002.
- [27] J.H. Weaver, D.T. Peterson, and R.L. Benbow. *Pys. Rev.*, 20:5301, 1979.
- [28] J. Osterwalder. *Z. Phys. B - Condensed Matter*, 61:113–128, 1985.
- [29] L. Schlapbach, J. Osterwalder, and H.C. Siegmann. *J. of the Less-Common Metals*, 88:291, 1982.
- [30] A.C. Switendick. *Int. J. Quantum Chem.*, 5:459, 1971.

-
- [31] A.C. Switendick. *Sol. State Comm.*, 8:1463, 1970.
- [32] M. Gupta and J.P. Burger. *Phys. Rev. B*, 22:6074, 1980.
- [33] D.K. Misemer and B.N. Harmon. *Phys. Rev. B*, 26:5634, 1982.
- [34] the three dimensional contourplot was generated with MathGl3D , an extension to Mathematica from Wolfram Research, to be found at <http://phong.informatik.uni-leipzig.de/kuska/mathgl3dv3/index.htm>.
- [35] G.S. Fleming, S.H. Liu, and T.L. Loucks. *Phys. Rev. Lett.*, 21:1524, 1968.
- [36] H.M. Fretwell, S.B. Dugdale, M.A. Alam, D.C.R. Hedley, and A. Rodriguez-Gonzalez. *Phys. Rev. Lett*, 82:3867, 1999.
- [37] M. Gupta. *Solid State Communications*, 27:1355–1359, 1978.
- [38] G. Gruner. *Density Waves in Solids*. Connecticut, USA, 2000.
- [39] S.H. Liu. *Solid State Communications*, 61:89, 1987.
- [40] R.R. Arons and J. Schweizer. *J. of Appl. Phys.*, 53:2645, 1982.
- [41] I.I. Mazin and D.J. Singh. *Phys. Rev. Lett.*, 82:4324, 1999.
- [42] J. Shinar, B. Dehner, R.G. Barnes, and B.J. Beaudry. *Phys. Rev. Lett*, 64:563, 1990.
- [43] A number of authors proposed the opening of a gap due to symmetry lowering via wave-like modulation of H atoms in the complicated HoD₃ structure. In view of an equivalent electronic structure of LaH₃ which apparently does not exhibit these wave-like modulations, a broken symmetry / charge density wave scenario has become rather doubtful.

Chapter 7

Electronic Structure of the YH_3 Phase from Angle-Resolved Photoemission

J. Hayoz¹, C. Koitzsch², M. Bove¹, D. Naumović¹, L. Schlapbach¹ and P. Aebi²

¹*Université de Fribourg, Institut de Physique, Perolles, CH-1700 Fribourg, Switzerland*

²*Institut de Physique, Université de Neuchâtel, CH-2000 Neuchâtel, Switzerland*

Phys. Rev. Lett. 90, 196804 (2003)

Abstract:

Yttrium can be loaded with hydrogen up to high concentrations causing dramatic structural and electronic changes of the host lattice. We report on angle-resolved photoemission experiments of the Y trihydride phase. Most importantly, we find the absence of metal d -bands at the Fermi level and a set of flat, H -induced bands located at much higher binding energy than predicted, indicating an increased electron affinity at H sites.

7.1 Introduction

Recently, switchable optical properties of metal hydrides at ambient pressures and temperatures have attracted strong interest.[1] For trivalent Y , for instance, up to three H atoms can be absorbed. The dihydride is even a better metal than Y itself but during the transition to the trihydride phase it turns from shiny metallic to transparent and insulating. With H a proton and an electron are introduced to the metal host. This results in doping the host material. Different models have been proposed to explain this spectacular metal-insulator transition (MIT). However, the behavior of H in such hydrides is still under debate.

State-of-the-art *ab-initio* local density approximation (LDA) calculations do not reproduce the optical gap necessary to explain the transparent state in the trihydride phase unless additional symmetry lowering is considered by displacing H atoms away from positions given by the HoD_3 structure of YH_3 . [2] Other models[3, 4], based on strong electron correlations, have been proposed to explain the MIT. Ng et al. [3] studied the effect of correlations on the bandwidth of H induced states. Hydrogen is present in the form of H^- [5, 6], where one electron is taken from the metal host. The two electrons on H^- are strongly correlated and the essence of the result of Ng et al. [3] is that the opening of the band gap is due to a correlation-induced band narrowing.

The model of Eder et al. [4] is based on the observation that the radius of H is very sensitive to the occupation number. The two electrons on H^- are correlated but with drastically different radii around the proton. This results in a so-called breathing mode and a local singlet-like bound state with one electron on the proton and the other on the neighboring metal orbitals. Already at the meanfield level this introduces a significant correction to the potential at the H site, effectively increasing the electron affinity, lowering the H band and opening the gap.

On the other hand, very recent GW-calculations [7, 8] demonstrate the formation of a sufficient gap to explain the MIT without need of strong electron correlations. Rather, these calculations indicate that the gap opening is described as in normal semiconductors. For semiconductors LDA does not produce the correct gap whereas the self-energy corrections included in the GW-calculations are able to account for this deficiency.

Indeed, detailed angle-resolved photoemission (ARPES) experiments are needed to favor one or the other model. However, practically all previous work

on metal hydrides has been done on polycrystals and/or on samples that are capped with a protective Pd layer. In order to perform ARPES experiments, uncapped single crystalline material is needed. Furthermore, preparation has to take place *in situ* since Y is extremely reactive.

Here we present, to our knowledge, the first ARPES data on the trihydride phase of uncapped single crystalline films. We find that the overall bandwidth of the Y trihydride phase agrees with LDA calculations. However, a set of flat bands is observed with significantly higher binding energy, a fact that argues in favor of the model proposed by Eder et al. [4].

7.2 Experimental Details

Experiments were performed in a VG ESCALAB Mk II spectrometer with motorized sequential angle-scanning data acquisition. [9] ARPES measurements were performed with monochromatized He I α ($h\nu = 21.2$ eV) at room temperature. [10] The energy resolution is 35 meV. Single crystalline Y hydride films were grown on a W(110) single crystal. Details of the preparation and the careful characterization of the crystal and electronic structure and the calibration of the H -concentration have been described elsewhere [11, 12]. In brief, this setup allows to prepare clean, single-crystalline rare-earth hydride films using H pressures up to 1.3 bar. It combines a high-pressure reaction cell with a custom made hydrogen purification system based on a Pd-24%Ag permeation tube and a sorption pump. The results presented here are taken from 200 Å thick, well-ordered[13] single crystalline films[11] in the trihydride phase.[14] The H composition is determined via photoelectron diffraction and X-ray photoelectron spectroscopy (not shown) to be $YH_{2.9}$. [11]

Bandstructure calculations using the full-potential linearized augmented plane-wave method [15] within the generalized-gradient approximation [16] have been performed for comparison with the experiments. Calculations were performed for the HoD_3 structure with space group 165 ($P\bar{3}c1$). The lattice parameters used for the YH_3 calculation were $a = b = 6.34$ Å and $c = 6.6$ Å. A total of 485 k-points within the irreducible wedge of the Brillouin zone (BZ) were considered for the self consistency cycles and convergence was reached to within 0.1 mRy.

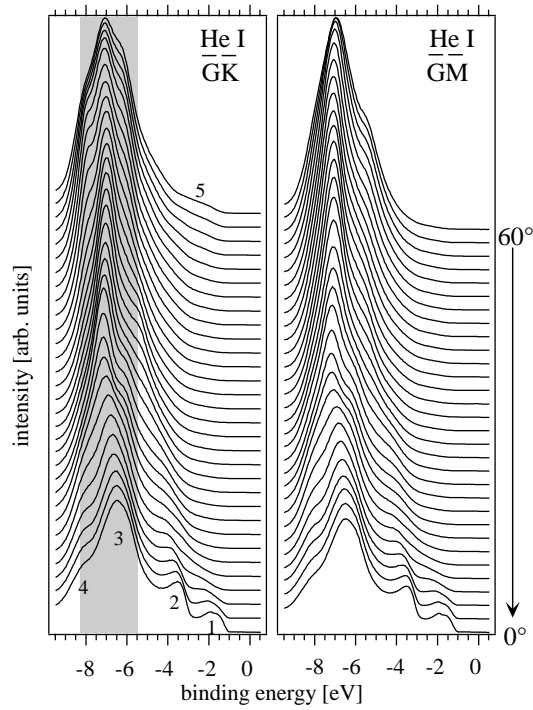


Figure 7.1: Energy distribution curves taken along the $\bar{\Gamma}\bar{K}$ (left) and $\bar{\Gamma}\bar{M}$ (right) directions of the surface BZ (see Fig. 7.2), using HeI radiation and collecting spectra up to 60° off-normal emission. Normal emission (0°) corresponds to $\bar{\Gamma}$; the \bar{K} and \bar{M} points are reached approximately at 17° and 15° off-normal emission, respectively, for 0 eV binding energy. Mapping into k-space is shown in Fig. 7.4. A shaded area marks weakly dispersing, broad spectral features (see text).

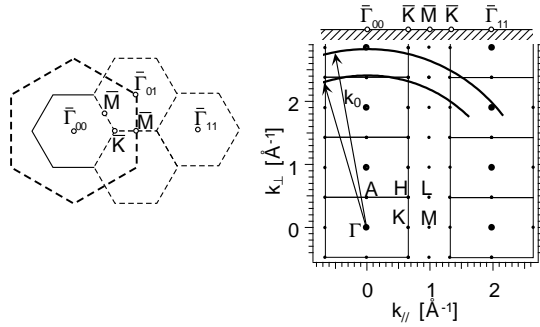


Figure 7.2: Situation in k -space. (Left) The surface BZ for the HoD_3 structure with high symmetry points. The large hexagon represents the surface BZ for the Y sublattice. (Right) Section across the bulk BZ containing the Γ, A, H, L, M, K high symmetry points. Spherical segments indicate the k -space region probed within the free-electron final-state approximation used for the calculation in Fig. 7.4.

7.3 Results and discussion

Figure 7.1 shows ARPES data measured along two high symmetry directions of the surface BZ. The situation in reciprocal space is illustrated in Fig. 7.2 where the surface BZ (left) and a cut through the extended bulk BZ containing the Γ, A, H, L, M, K high symmetry points (right) is shown. YH_3 with the HoD_3 structure consists of a $(\sqrt{3} \times \sqrt{3}) - R30^\circ$ reconstruction with respect to the hexagonal Y-lattice, i.e., the unit cell has a and b vectors which are $\sqrt{3}$ times longer and rotated by 30° . Therefore the YH_3 BZ is smaller and rotated accordingly (Fig. 7.2).

Inspecting the experimental spectra (Fig.7.1) a similar behavior is observed for both directions. The dispersion appears relatively weak and the electronic states do not reach the Fermi level (E_F) or 0 eV binding energy, which is indicative for a gap. The d -states that are present in Y ($[\text{Kr}]4d^15s^2$) and YH_2 (not shown) have disappeared.[17] Five dispersing features are easily discernible and are labeled from 1 to 5. A broad almost dispersionless maximum between 5.5 and 8.3 eV (shaded area) persists for all angles respectively k -points. At first sight one is tempted to interpret the fact that the dispersion is weak and the spectral features are broad as caused by strong electron correlations and self-energy effects.

However, taking a closer look reveals a different point of view. In Fig. 7.3 the result of our bandstructure calculation of YH_3 in the HoD_3 structure

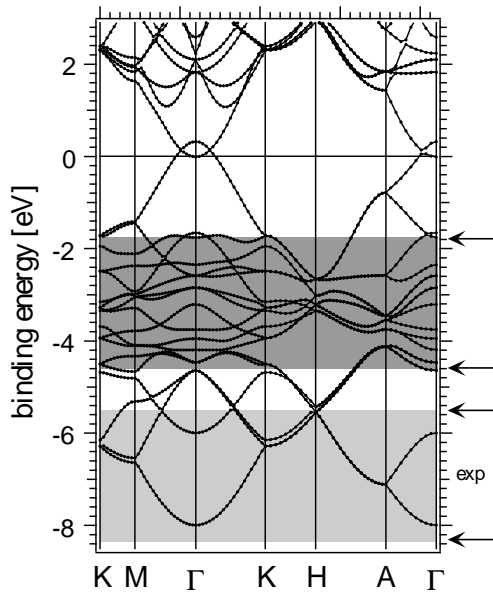


Figure 7.3: LDA based bandstructure calculation for the HoD_3 structure. Indicated is the region (dark shading) of flat, H -induced bands and the corresponding region (light shading) where the experiment (Fig. 7.1) shows a high density of states. (see text)

is displayed. As mentioned above the approach using LDA does not show a gap. The calculation presented here is in good agreement with the results of Kelly et al.[2]. We notice that there are many bands. This is a consequence of the large real-space unit cell of the HoD_3 structure containing 24 atoms including 6 Y atoms and 18 H atoms in the unit cell. The important point to notice here is that there is a set of rather flat, H -induced bands (as deduced from a band character analysis) between 1.8 and 4.6 eV (dark shaded area) extending over the whole bulk BZ. Such a set of flat bands naturally gives rise to a high density of states (DOS) in this energy region. This leads to the interpretation of the broad, high intensity features in the experiment (shaded area in Fig. 7.1) as due to these flat bands. [18] The energy width of the region in the experiment agrees well with the energy interval of the flat bands in the bandstructure calculation. The only difference is that the experimental bands occur at a 3.7 eV greater binding energy.

In order to obtain a more detailed comparison we use a gray scale repre-

presentation of both, the experimental data and the calculated band structure. Figure 7.4 displays the results along the $\bar{\Gamma}\bar{K}$ -direction. For the experimental data (left) the second derivative of the spectra of Fig. 7.1 has been plotted as a function of wave vector parallel to the surface ($k_{//}$). The reason for plotting the second derivative is to flatten the spectra and to accentuate the dispersing features. The calculation (right) follows the free-electron final-state (FEFS) wave vectors drawn in Fig. 7.2 [19]. The locations of the flat bands are marked by shading the energy scales in both the experiment and the calculation where they occur with a 3.7 eV smaller binding energy. We have to note that the experiments do not probe the path along high symmetry directions in the *bulk* BZ. Rather, the experiment follows a circle-like path as indicated in Fig. 7.2. At $k_{//}$ values between 0.7 and 1 Å⁻¹ (see Fig. 7.2, right) we pass the region of K and M points and we can compare Fig. 7.4 with the KM dispersion of Fig. 7.3. The bands are concentrated around a narrow energy range and the discrepancy between experiment and calculation induced by the band shift is evident. In addition we can identify the bands labeled 1 to 5 as already indicated in Fig. 7.1. These labels, 1-5, in both figures have the same relative positioning, but in the calculation they are rigidly shifted upwards by ≈ 1.5 eV. At this point we have to note that the agreement of relative positions is extremely good taking into account the fact that we use the FEFS approximation. Labels 1, 2, 5 can directly be attributed to each other. The difficulty appears for labels 3 and 4 since this is where the downward shift of the flat bands affects the comparison. Looking at the right side of Fig. 7.4 (calculation) we see the flat bands between labels 2 and 3 as an accumulation of almost horizontal lines between 1.8 and 4.6 eV binding energy. In the experiment, as explained above, these flat bands appear between 5.5 and 8.3 eV binding energy. In fact they come to lie on top of labels 3 and 4 and therefore obscure the direct comparison between experiment and calculation in this energy range.

Comparing our experiments with the LDA calculation shows that the overall band width compares well. The differences are a rigid shift of approximately 1.5 eV and the position of the flat bands. However, a detailed comparison of different bands and their relative positions depends on the validity of the FEFS approximation. Therefore we cannot, at present, give a robust statement about the exact position of the top of valence band (label 1, Fig. 7.4, left) and, as a consequence, about the size of the gap. This depends on the exact location in the component of the wave vector perpendicular to the surface, k_{\perp} . On the other hand, the difference in the position of the flat bands is independent of

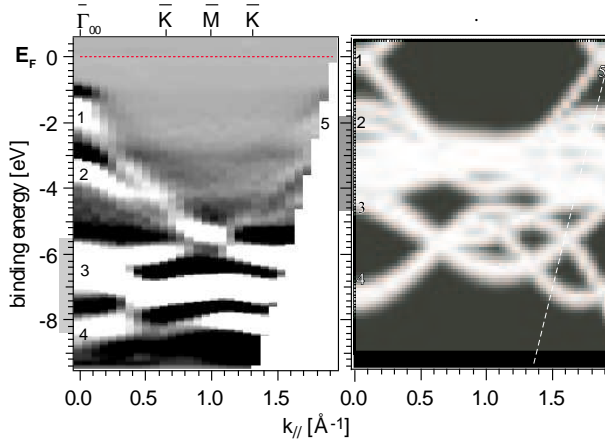


Figure 7.4: Second derivative of spectra from Fig. 7.1 mapped into k-space using gray scale intensity coding with high intensity in white (left). Model calculation using the FEFS approximation (right) (see text).

this approximation since the flat bands extend over the whole BZ as seen from experiment (Fig. 7.1) and theory (Fig. 7.3).

In a way the situation is very favorable for the interpretation. The spectra in Fig. 7.1 are very similar along the two different directions of the BZ. This indicates in particular that the broad feature between 5.5 and 8.3 eV binding energy is characteristic for the phase and persists in large parts of the BZ. At the same time the LDA bandstructure calculation of Fig. 7.3 shows the flat bands between 1.8 and 4.6 eV extending along all the high symmetry directions, again indicating that they are characteristic for the phase and persist in large parts of the BZ. Using this observation and attributing the flat bands to the high DOS, i.e., the broad high intensity spectral feature, we affirm the downward shift of flat bands. That the overall bandwidth is in good agreement with LDA also follows from comparing the experimental spectra (Fig. 7.1) and the bandstructure calculation (Fig. 7.3). In particular, the bandwidth extends down to below 8 eV binding energy.

It is interesting now to compare with theoretical models. At first we look at the GW calculations. In the study of Miyake et al. [7] the gap opens due to a shifting up of the conduction bands whereas in the case of van Gelderen et al. [8] the gap opens because of both, shifting up of the conduction bands and shifting down of valence bands. Otherwise the quasiparticle wavefunctions are

practically identical to the LDA wave functions and there is basically a one to one correspondence between the bands of the LDA and GW bandstructures. The total band widths do not differ significantly as well. From our experiments we conclude that the overall bandwidth is well reproduced by LDA and GW-calculations. However, the high binding energy of the flat bands is not reproduced. Even the downwards shift of the valence bands (≈ 1 eV) in the case of van Gelderen et al. [8] is not sufficient and does not account for the *relative* shift of certain bands.

Clearly, the good agreement of the overall bandwidth with the LDA calculations is in contrast to the model of Ng et al. [3] where strong electron correlations induce a band narrowing. However, we cannot exclude that individual bands are subject to narrowing. The reason is that from the experimental data, due to the large number of bands, it is not possible to identify every individual band. The width of the experimentally observed spectral features is not resolution limited and might be explained either by self-energy effects or also by a relatively high mobility of H atoms and defects due to the substoichiometry of the films. Furthermore, there is still debate on whether the HoD_3 structure really corresponds to the one for YH_3 . [20, 21]

Finally we compare our results to the model by Eder et al.[4]. The dependence of the occupation number of electrons on the H site is incorporated in their model Hamiltonian by having a novel hopping integral. The resulting singlet-like bound state is manifest via increasing the binding energy of the H states. Contrary to the treatment of Ng et al. where the result is a narrowing of bands, Eder et al.[4] predict a shift of the potential at the H site *retaining* the large H bandwidth.

It is now very tempting to interpret our data, showing a shift of bands towards higher binding energy, in terms of such an additional potential on H sites. Observing Fig. 7.3 it appears that only the set of flat bands is strongly shifted down whereas the others, covering the full bandwidth, are consistent with the GW approach. This might be interpreted in the sense that the bands within the set of flat bands have a more localized character and therefore are stronger affected by the singlet-like bound state. However, a detailed comparison of how different bands are affected is not possible since a realistic bandstructure for the HoD_3 structure is not available within Eder's model Hamiltonian.

7.4 Conclusion

In conclusion we have performed ARPES experiments on single crystalline films of Y in the trihydride phase. A comparison with LDA calculations shows a good agreement of the overall bandwidth. No significant band narrowing is observed although a narrowing of individual bands cannot be excluded. However a set of H induced, flat bands is identified in the experiment with a binding energy ≈ 3.7 eV higher than in the calculation. Furthermore, based on the FEFS approximation, we infer a rigid shift of the valence band towards higher binding energy by more than 1 eV which is consistent with GW-calculations [8] and the opening of a gap. The downwards shift of flat bands supports the model proposed by Eder et al.[4] predicting a shift of the potential at the H site and *retaining* the broad H band.

Acknowledgements Skillful technical assistance was provided by E. Mooser, O. Raetzo, R. Schmid, O. Zosso, Ch. Neururer and F. Bourqui. This project has been supported by the Fonds National Suisse de la Recherche Scientifique.

Bibliography

- [1] J.N. Huiberts, R. Griessen, J.H. Rector, R.J. Wijngaarden, J.P. Dekker, D.G. de Groot, and N.J. Koeman. *Nature*, 380:231, 1996.
- [2] P.J. Kelly, J. P. Dekker, and R. Stumpf. *Phys. Rev. Lett.*, 78:1315, 1997.
- [3] K.K. Ng, F.C. Zhang, V.I. Anisimov, and T.M. Rice. *Phys. Rev. Lett.*, 78:1311, 1997.
- [4] R. Eder, H.F. Penn, and G.A. Sawatzky. *Phys. Rev. B*, 56:10115, 1997.
- [5] F.J.A. den Broeder et al. *Nature*, 394:656, 1998.
- [6] M. Rode et al. *Phys. Rev. Lett.*, 87:235502, 2001.
- [7] T. Miyake, F. Aryasetiawan, H. Kino, and K. Terakura. *Phys. Rev. B*, 61:16491, 2000.
- [8] P. van Gelderen, P. A. Bobbert, P.J. Kelly, and G. Brocks. *Phys. Rev. Lett.*, 85:2989, 2000.
- [9] J. Osterwalder et al. *Phys. Rev. B*, 44:13764, 1991.
- [10] Th. Pillo et al. *J. Electr. Spectrosc. Relat. Phenom.*, 97:243, 1998.
- [11] J. Hayoz, T. Pillo, A. Zuettel, S. Guthrie, P. Aebi, and L. Schlapbach. *J. of Vac. Sci. Techn. A*, 18:2417, 2000.
- [12] J. Hayoz, S. Sarbach, Th. Pillo, D. Naumovic, P. Aebi, and L. Schlapbach. *Phys. Rev. B*, 58:R4270, 1998.
- [13] The films exhibit well-defined low energy electron diffraction spots according to the hexagonal arrangement of Y in the HoD_3 structure. The H-induced superstructure does not appear since H is a weak scatterer.
- [14] E_F calibration is important since the H_3 -phase is insulating and charging effects could shift the spectra; that this is not the case has been verified by blowing-up the zero-binding energy region up to the point where the Fermi-Dirac distribution onset becomes visible.

-
- [15] P. Blaha, K. Schwarz, and J. Luitz. *Comput. Phys. Commun.*, 59:399, 1990. Improved and updated UNIX version of the original copyrighted WIEN code by P. Blaha, K. Schwarz and P. Sorantin.
- [16] J.P. Perdew, S. Burke, and M. Ernzerhof. *Phys. Rev. Lett*, 77:365, 1996.
- [17]
- [18] DOS calculations (not shown) indicate indeed a peaked DOS around 3 eV (region of flat bands). Matrix elements should not change strongly over the binding energy range (since all bands below E_F have almost exclusively H character) and the interpretation of the spectral intensity in terms of DOS should be valid.
- [19] The gray scale levels of the calculation are determined by checking energy conservation with respect to the FEFS, i.e., perfect energy conservation appears in white. An inner potential of 10 eV and a workfunction of 3 eV have been assumed. No matrix-elements are considered.
- [20] T.J. Udovic et al. *Phys. Rev. B*, 61:12701, 2000.
- [21] P. van Gelderen, P.J. Kelly, and G. Brocks. *Phys. Rev. B*, 63:100301, 2001.

Part III
Quantum Wells

Chapter 8

Introduction to Quantum Well States

8.1 General Remarks

One of the basic tenets of solid state physics is the quasicontinuity of states in k-space. The Born-von Karmann boundary condition adapts the wavefunctions to the macroscopic dimensions of the crystal. For a three dimensional crystal the k-space volume per state $D(k) = \frac{(2\pi)^3}{L^3}$ is due to the large volume L^3 so small, that macroscopic properties of solids, which depend on all k states, do not depend on the outer dimensions of the sample. However if these outer dimensions are reduced to the order of some lattice constants this should change and measurements should reflect the quantum nature of matter. Semiconductor super lattices are a familiar example, where quantization effects due to wavefunction confinement are employed for device purposes, e.g. laser diodes employ band gaps as effective confinement barriers. However for metallic super lattices these band gaps do not extend over the complete Brillouin zone, instead the metallic substrate provides only a confinement in certain directions. Therefore in order to detect quantum effects in the case of metallic interfaces k-resolved measurements are appropriate.

Two very well written review articles, which give an introduction into the field of metallic quantum wells are recommended to the reader [1][2]. These articles summarize a development, which started with tunnelling experiments on Pb, Mg, Au, and Ag already 30 years ago by Jaklevic and Lamb[3], who observed periodic structures in the tunnelling signal, which they identified as

a direct observation of size dependant electronic states. An even more direct method to observe these states is photoemission and Loly and Pendry [4] pointed out, that theoretically photoemission spectra of thin films should consist of a number of thickness dependent, closely spaced states. By that time nobody had observed such quantum well states, which was basically due to the fact, that theory did not take into account the experimental film thickness fluctuations. Only the advances of thin film growth with molecular beam epitaxy made the preparation of more or less atomically uniform films possible and the first direct observation of quantum well states with photoemission was reported in 1986 [5].

8.2 This Work

In this work we investigated the heteroepitaxial system Mg(0001) on W(110). Starting from a simple particle in a box model, it is derived how the energy quantization of thin films is related to the bulk band structure of the overlayer material. For this purpose the phase accumulation model is introduced and its predictions for different thicknesses are compared to experimental photoemission data. A separate chapter is dedicated to the analysis of the in-plane dispersion of these thin-film states, which is found to depend strongly on the underlying W(110) band structure. The high atomic mass of the substrate is expected to give rise to strong spin-orbit effects of the confined overlayer states. The Rashba effect at the interface gives rise to a zero-field spin splitting of Mg surface states and quantum well states.

8.3 Experimental Details

Thin films of Mg were prepared by evaporation from a water-cooled resistively heated molybdenum basket onto clean W(110) at room temperature. The pressure during evaporation was 7×10^{-10} mbar. The deposition rate was monitored by a water cooled crystal rate monitor. X-Ray photoelectron diffraction was employed to determine the epitaxial relationship between the Mg thin film and the underlying W(110) substrate. It is found that Mg grows epitaxially in (0001) direction and the hexagonal Mg layers obey the Nishiyama-Wassermann relationship[6] with the substrate, where the $[11\bar{2}0]_{hexagonal}$ direction is aligned with $[001]_{bcc}$ direction of the substrate. Fig. 8.1 shows the bulk structure of

W and Mg and the corresponding surface meshes, together with the respective surface Brillouin zone. Additionally, X-Ray photoelectron diffraction pattern (8.1g,h), which corroborate the structural analysis are shown together with the stereographic projection of atom-atom directions present in W(110) and Mg(0001) crystals (red circles). XPD pattern from Mg thin films on W(110) are clearly 6-fold symmetric and indicate high growth quality. The 6-fold symmetry indicates a largely unstrained overlayer growth, which is quite common for metals. This is in contrast to strained superlattices in the case of semiconductor heterostructures and reflects the isotropic nature of the metallic bond.

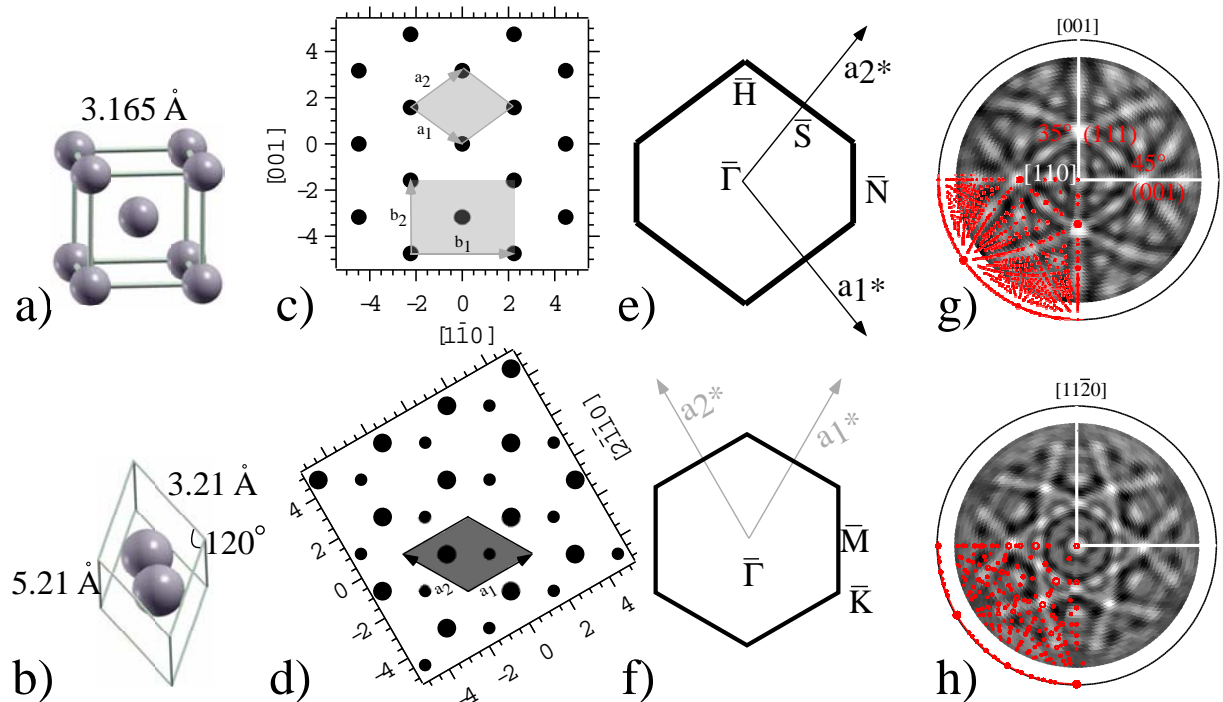


Figure 8.1: Structural properties of W and Mg. a,b) Bulk unit cell of bcc tungsten and hcp magnesium. c,d) Surface mesh of W(110) and Mg(0001) with correct orientation to each other e,f) Surface Brillouin zone of W(110) and Mg(0001) with high symmetry points. g,h) X-ray photoelectron diffraction pattern of W 4f and Mg 2s core levels together with the stereographic projections created from cluster models for the two structures.

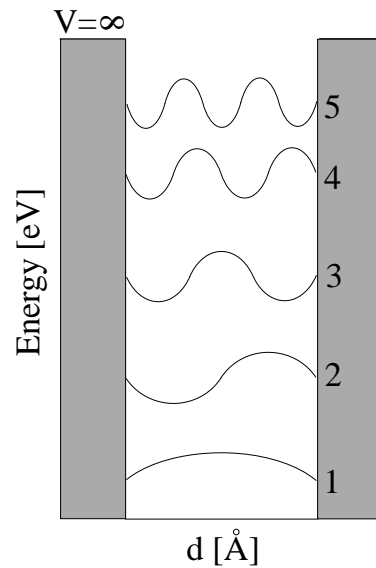


Figure 8.2: Particle in the box solutions

8.4 Evolution of QWS with thickness

The first starting point for an understanding of thin film quantum well states is a review of the one dimensional particle in a box model of finite width d and full confinement, which means that the potential barrier is assumed to be infinitely high.

The time independent Schrödinger equation

$$-\frac{\hbar^2}{2m} \cdot \frac{d^2u(x)}{dx^2} + V(x)u(x) = Eu(x) \quad (8.1)$$

has to be solved for the appropriate boundary conditions of the problem.

$$\begin{aligned} V(x) &= \infty & x < 0 \\ &= 0 & 0 < x < d \\ &= \infty & x > d \end{aligned} \quad (8.2)$$

The general solution $A \cdot \sin(kx) + B \cdot \cos(kx)$ translates due to $u(0)=0$ and $u(d)=0$ (continuity) to

$$u(x) = A \cdot \sin(kx) \quad kd = n \cdot \pi \quad (8.3)$$

This means that only certain k values can be fit into the geometry as it is shown in Fig. 8.2. The corresponding free electron eigenvalues become quantized such that the energy scales with the square of the quantum number n . Six layers of Mg in [0001] direction correspond to a thickness of 5· interlayer distances of 2.605Å. Of course, the exact well thickness depends on the location of the interface.

$$E_{n;sixlayers} = \frac{\hbar^2 k^2}{2m} = \frac{\hbar^2 \pi^2 n^2}{2m \cdot 13\text{\AA}^2} = 0.222eV \cdot n^2 \quad (8.4)$$

For each thickness a series of peaks is expected, which become more and more closely spaced. Such a model does not consider the exact form of the boundaries, which provide some confinement but especially the interface between film and substrate might allow some wave function leakage. In the particle in the box model such a wave function leakage is introduced with adjusted boundary conditions, which matches the wave function inside the well to an exponentially decaying wavefunction outside of the well. Furthermore the details of the Mg band structure $E(k)$ are not considered. The latter is easily corrected by displacing the free electron dispersion relation (8.4) with the $E(k)$ relation of bulk Mg in the correct [0001] direction. This direction corresponds in reciprocal space to the ΓA direction and quite similarly to the free electron case one has to determine the eigenvalues belonging to k -values which satisfy the phase accumulation model (equation 8.5).

$$\phi_{interface} + \phi_{surface} + 2 \cdot k_{\perp} \cdot d = 2n\pi \quad (8.5)$$

This model assigns to the reflection at the well boundaries and the wave propagation in the film a phase shift. For the following simple analysis the interface and surface contributions are not considered, which is particularly appropriate for very thick films, where the film contribution becomes the dominant term. Fig. 8.3 summarizes the main idea. The bulk band structure along ΓA is discretized, such that the allowed solutions "fit" into the cavity. The connection between the dimensions of the Brillouin zone and the allowed k vectors arises from relation between real space lattice and reciprocal lattice, which allows to rewrite equation 8.5 ($\phi_{interface}$ and $\phi_{surface}$ are neglected)

$$k_{\perp} = \frac{n\pi}{d} = \frac{n\pi}{N \cdot a_{unitcell}} = \frac{n}{N} \cdot \Gamma A = \left(1 - \frac{\nu}{N}\right) \cdot \Gamma A \quad (8.6)$$

, where a new reduced quantum number $\nu=N-n$ is introduced. For a 10 and 12 unit cells thick film, the procedure to obtain the allowed eigenvalues is

schematically indicated. The Brillouin zone is sectioned along ΓA into N equal k -slices. Wherever such an allowed k -point coincides with a bulk Mg band a QWS is expected. For a 10 ML thick film we expect two occupied QWS, while for a 12 ML thick film the state $\nu=3$ has already crossed the Fermi level and we expect three occupied QWS. The uppermost Bulk band, which gives rise to QWS closest to the Fermi level cuts the Fermi level at $\approx 1/4$ ΓA . Therefore not every additional unit cell leads to a new occupied QWS and in fact the appearance of a new QWS allows for a very accurate thickness determination. If the indicated graphical construction is repeated for a number of thicknesses, one can obtain a so called structure plot, as it is shown in 8.3. It shows the evolution with thickness (or with N) for quantum well states, which are all derived from the same Mg bulk band but which belong to different ν 's. From inspecting this structure plot, main characteristics for quantum well state evolution with thicknesses can be extracted. If the film thickness is increased, the number of allowed QWS increases. The energy spacing between quantum well states depends on the bulk band dispersion from which the QWS are derived. Therefore localized bands (e.g. d-bands) are expected to give rise to narrowly spaced quantum well states, while sp-bands should be more similar to the free electron model. The dispersion with thickness is drawn as a continuous line. However the thickness cannot vary continuously because each layer has a discrete height. For a minimal roughness in film thickness, one expects experimentally not a continuous shift of levels but the abrupt appearance of new states if the thickness is increased appropriately.

An alternative approach to understand the occurrence of quantum well states are *ab-initio* slab calculations. If the electronic problem is solved for a super cell geometry, one expects to observe similarly thickness dependant states. A supercell consists of a number of bulk-like unit cells, which are separated by a sufficient amount of vacuum in between. Such an approach still employs periodic boundary conditions in three dimensions. However in one direction the symmetry is broken by the introduction of vacuum space. The structure resembles therefore a free standing thin film. This has the advantage that the surface potential step is accurately described. However the film substrate interface is not included but assumed to be equivalent to the surface potential step, since the surface is included twice (front and backside are equivalent). The electronic structure calculations are based again on Density Functional Theory (DFT) and the full potential augmented plane wave code APW+lo Wien2k [7] was employed. Fig. 8.4a) shows as an example the comparison between a 3

unit cell slab geometry and the Mg bulk structure. The in-plane crystal structure remains unchanged as it is shown in Fig. 8.4a). However the out-of plane symmetry is broken by including a 12Å thick vacuum region. Nevertheless we employ periodic boundary conditions, which makes the choice of an appropriate vacuum thickness ambiguous. The free standing slabs should not interact over the vacuum region but on the other hand, the unit cell size should still allow a matrix diagonalization in a reasonable computation time. A vacuum thickness of 12Å is certainly conservative to minimize the interaction over the vacuum layer. Slab calculations have been used mainly in conjunction with the description of surface states. There, the idea is to simulate a semi infinite system, which translates into a many-layer slab in order to avoid not only an interaction over the vacuum region, but an interaction over the crystal region as well. The computation of the Au(111) surface state required the use of 19 gold layers in order to have a minimal bonding-anti bonding split between the two surface states[8]. In the present case however, we are exactly interested in these kind of interference phenomena due to the finite size of the quantum well, respectively the finite size of the slab. However the surface state is then necessarily not adequately described, since we are dealing with a thin free standing film and not a semi-infinite crystal.

Upon comparing the band structure of the slab (Fig. 8.4d) to the Mg bulk

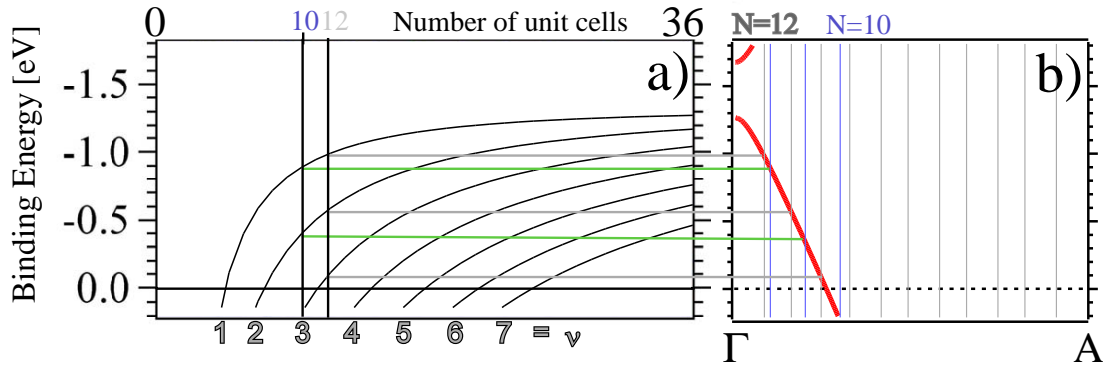


Figure 8.3: Phase accumulation model for Mg quantum well states a) structure plot showing the evolution with thickness and quantum number ν for b) [0001] bulk band derived quantum well states

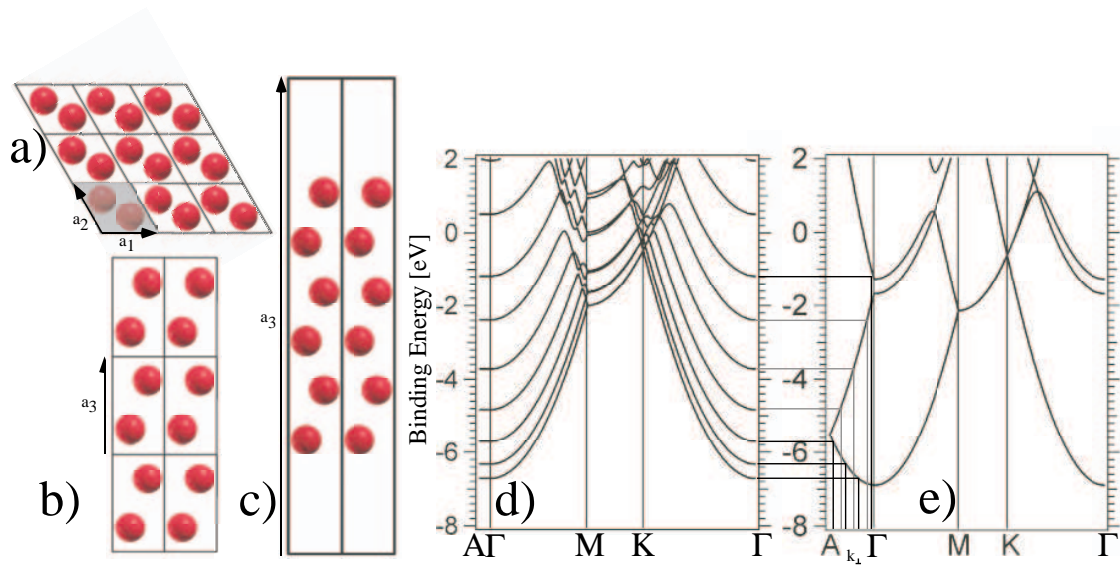


Figure 8.4: Band Structure calculations for bulk Mg and a 3 unit cell slab. a) In-plane structure for slab and bulk phase. b) Out-of-plane structure for bulk calculations. c) Out-of-plane structure for a three unit cell slab with 12 Å vacuum space. d) Slab band structure along high symmetry directions. e) Bulk band structure along high symmetry directions with corresponding k -values for the slab band structure at Γ (see text)

(Fig. 8.4e) band structure, we note similarly to the phase accumulation model a quantization of bulk bands in the slab band structure. Since the confinement is only in [0001] direction, the bands between Γ and A are quantized. Compared to the phase-accumulation model, the ab-initio calculations reveal the energy dependence of the k vector quantization. Each eigenvalue at Γ in the slab calculations corresponds to a slightly different bulk k_{\perp} value. A free electron-like parabola is attached to each of these allowed k_{\perp} values. A quantization perpendicular to the surface generates therefore a number of stacked parabolas, whose in-plane dispersion is not affected by the quantization.

The correspondence between the slab eigenvalues at Γ (Fig. 8.4d) and the k_{\perp} values in the bulk band structure (Fig. 8.4e) are shown with lines between Fig. 8.4d) and Fig. 8.4e). The major difference to the phase accumulation model is, that each band is differently quantized. The energy-independent phase accumulation would predict the same k_{\perp} values for eigenvalues derived from different bands, but with the same quantum numbers. One can understand this phenomena as an energy dependant extension of the wavefunction in the slab. The same effect can be introduced in the phase accumulation model as energy dependant phase shifts at the surface and the interface

$$\phi_{interface}(E) + \phi_{surface}(E) + 2 \cdot k_{\perp} \cdot a = 2n\pi. \quad (8.7)$$

The phase shift at the surface is expected to be isotropic and largely independent of the specific surface structure. McRae and Kane[9] proposed a formula, which solely depends on the position of the vacuum level (E_V) and the energy (E) of the QWS.

$$\phi_{surface}(E) = \pi \sqrt{\frac{3.4eV}{E_V - E}} - \pi \quad (8.8)$$

The interfacial phase shift on the other hand cannot be described in general by such a universal formula. For full confinement Smith proposed a phase shift, which solely depends on the position within the gap[10]. However for the resonant case, the coupling between quantum well resonances and substrate Bloch states depends on energy, k -vector and symmetry and hence the intricate wave function matching cannot be associated with band edges of the substrate projected band structure. It is the purpose of the following chapter to investigate in more detail the transition between a quantum well state and a quantum well resonance. Instead of tuning the QWS energy with thickness such that a gap is crossed in normal emission, we follow a more convenient approach and map the

dispersion with k_{\parallel} for a given thickness and observe the "quantum well state to resonance transition" for a substrate dependant k_{\parallel} (see below).

8.5 Results for normal emission

We now turn to the results from UV photoemission spectroscopy, where we expect thickness dependant quantum well states, as it has been discussed in the previous section. Fig. 8.5 shows one of the first sets of UPS spectra in normal emission geometry from an ≈ 20 unit cell thick film for different excitation energies. We observe the well known surface state at -1.7 eV and additionally, above the surface state, a series of closely spaced states, which resemble the expected quantum well states. The photoemission cross section is optimal for H Ly α radiation and therefore all subsequent studies involving the parallel dispersion of QWS have been performed with an excitation energy of 10.2 eV. The slight change in energy for different excitation energies has been observed for Ag(111) on Ni(111) as well [1] and seems to be a general property of quantum well resonance systems compared to true quantum well states, which should (as two-dimensional states) show no dependance on the photon energy.

The most important criterium for the detection of QWS is however their thickness dependance and the preceding section posed the question if the evolution with thickness can be described by a simple phase accumulation model. The phase accumulation model yields sets of quantum well states, which become more numerous and more closely spaced with increasing thickness. In Fig. 8.6 such a behavior is clearly obtained for UPS spectra in normal emission geometry for different thicknesses. The thickness is adjusted to a maximum agreement. An absolute experimental thickness measurement with an oscillating quartz crystal was not feasible.

Similarly to Fig. 8.3 we observe an increasing number of quantum well states, whose thickness evolution can be well described with a discretization of Mg bulk bands (Fig. 8.6b). For very thin films a decrease in surface state energy indicates an increasing overlap between the surface state wave function and the substrate. We observe QWS up to 36 unit cells, which indicates a very high uniformity of film growth.

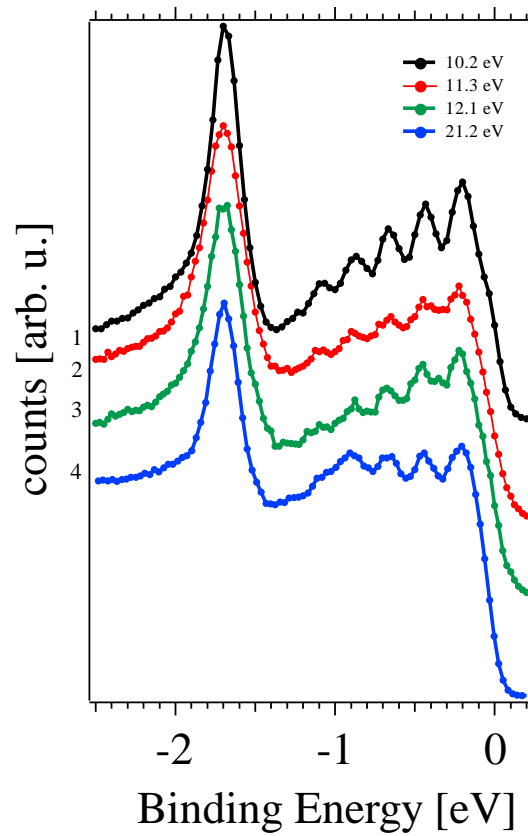


Figure 8.5: UPS spectra in normal emission geometry for different excitation energies, the spectra have been normalized to the intensity of the surface state at -1.7 eV

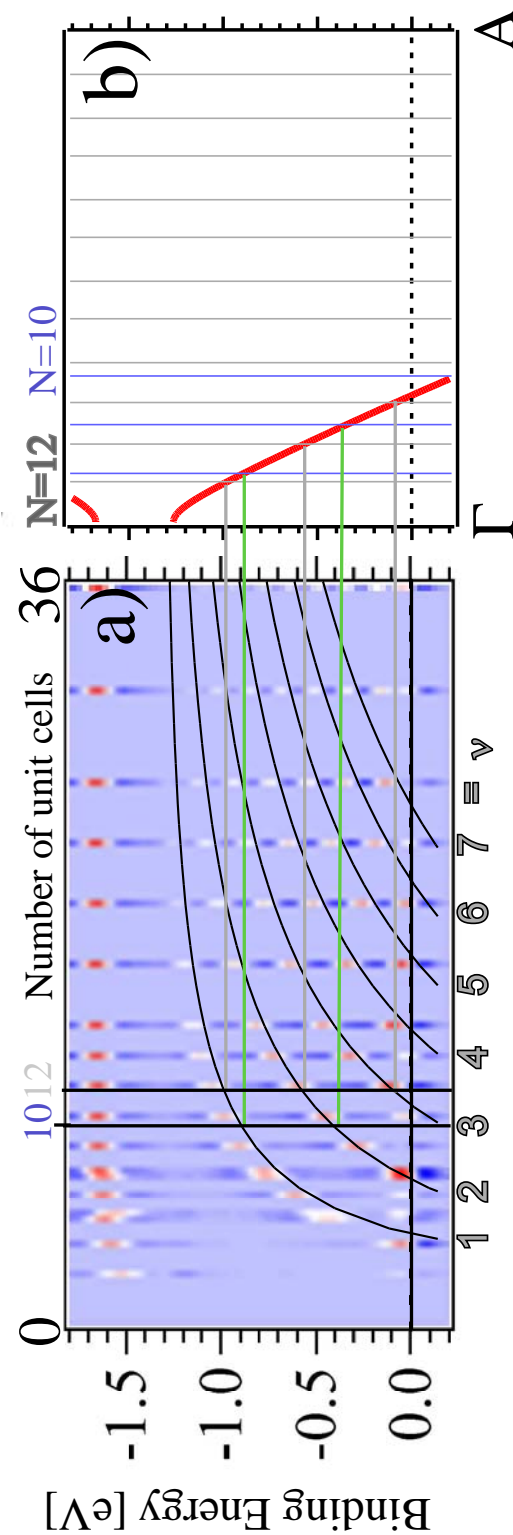


Figure 8.6: UPS spectra in normal emission geometry for different thicknesses. A red-white-blue representation of the second derivative of spectra obtained from different thicknesses is shown. Red corresponds to high photoemission intensity

Bibliography

- [1] T.C. Chiang. *Surface Science Reports*, 39:181, 2000.
- [2] M. Milun, P. Pervan, and D.P. Woodruff. *Reports on Progress in Physics*, 65:99, 2002.
- [3] R. C. Jaklevic and John Lambe. *Phys. Rev. B*, 12:4146, 1975.
- [4] P.D. Loly and J.B. Pendry. *J. Phys. C*, 16:423, 1983.
- [5] A.L. Wachs, A.P. Shapiro, T.C. Hsieh, and T.-C. Chiang. *Phys. Rev. B*, 33:1460, 1986.
- [6] L.A. Bruce and H. Jaegger. *Philos. Mag. A*, 38:223, 1978.
- [7] P. Blaha, K. Schwarz, and J. Luitz. *Comput. Phys. Commun.*, 59:399, 1990. Improved and updated UNIX version of the original copyrighted WIEN code by P. Blaha, K. Schwarz and P. Sorantin.
- [8] G. Nicolay, F. Reinert, S. Huefner, and P. Blaha. *Phys. Rev. B*, 65:033407, 2002.
- [9] E.G. MacRae and M.L. Kane. *Surf. Sci.*, 108:435, 1981.
- [10] N.V. Smith. *Phys. Rev. B*, 32:3549, 1985.

Chapter 9

Photoemission of a Quantum Cavity with non-magnetic Spin Separator

C. Koitzsch, C. Battaglia, F. Clerc, L. Despont, M.G. Garnier and P. Aebi

*Institut de Physique, Université de Neuchâtel, CH-2000 Neuchâtel,
Switzerland*

accepted for publication in Phys. Rev. Lett.

Abstract: Quantum well states or more familiar *particle in a box* states are a consequence of confinement in a quantum cavity. In this study we investigate with photoemission the influence of the interface electronic structure on the quantum well state energy dispersion in ultra thin Mg(0001) films on W(110). The possibility of coupling between the sp-derived quantum well states and the substrate across the interface becomes manifest in a deviation from free electron-like dispersion behavior. Most importantly, we observe a marked level splitting, which is interpreted as due to the Rashba effect at the interface. The Rashba effect is a relativistic effect, which, in the vicinity of strong potential gradients, leads to electron spin

splitting. Such an interfacial electron beam splitting on materials with strong spin-orbit coupling is an essential ingredient for novel spintronic devices. The combination of a quantum cavity with a heavy, electron reflecting substrate demonstrates the necessity for a relativistic extension of the simple particle in the box model.

9.1 Introduction

Classical physics is at its limit for reduced dimensions, where the quantum regime comes into play. The wavelike nature of electrons is frequently introduced with the *particle in a box* model. The advent of molecular beam epitaxy allowed the direct investigation of this textbook example of quantum mechanics with high resolution photoemission. [1][2] (and ref. therein). Discrete, thickness dependent energy levels (see Fig. 9.1a) originate from the finite film thickness, which permits only certain cavity eigenmodes or quantum well states, whose wavelengths (λ) form a standing wave upon reflection at the boundaries (see Fig. 9.1b). Depending on the $E(\lambda)$ relation in the solid, these allowed wavelengths translate into discrete energy levels. [3] In a first, semi-classical approach, tunneling across the confining barriers is usually neglected. This model is frequently called in quantum mechanics textbooks a *particle in a box* with infinitely high walls, see Fig. 9.1c). In reality however the barrier height is only finite and the wavefunction might leak to some extent over the interface barrier. Therefore the electron wavefunction inside the cavity has to be matched to an appropriate wavefunction at the cavity boundaries. The quantum well state (QWS) is (partially) reflected and has to be matched to an evanescent wave, if no coupling crystal Bloch states are available. Otherwise the matching proceeds with substrate Bloch states. One distinguishes between quantum well states (complete confinement) and quantum well resonances (partial confinement due to coupling).

If the cavity modes are tuned such that the coupling scheme switches to the resonance case (or vice versa), one expects a discontinuous change in the allowed wavelengths and corresponding energies (see Fig. 9.1d). In this sense the quantized states probe, via their reflectivity, the energy dependent substrate band structure, as will be demonstrated below.

The main purpose of this study is to show that there is another effect (not considered so far for QWS) that influences, modifies or tunes the QWS. The substrate not only perturbs the dispersion relation, it may also lead to an

appreciable spin-splitting of the quantum well states.

The interfacial, electron reflecting potential gradient translates, via relativistic Zeeman coupling, to an effective in-plane magnetic field, which in turn lifts the spin degeneracy. The size of this so-called Rashba splitting [4] is given by the Hamiltonian $H_{Rashba} \sim (\vec{k} \times \nabla \vec{V}) \cdot \vec{\sigma} \sim B_{eff} \cdot \vec{\sigma}$. The geometrical relation between plane wave propagation vector (\vec{k}), interfacial potential gradient ($\nabla \vec{V}$) direction and the effective in-plane magnetic field (B_{eff}) is shown in Fig. 9.1e). The spin-splitting $E(k, \uparrow) \neq E(k, \downarrow)$ into up-spin, \uparrow , and down-spin, \downarrow for $k_{\parallel} \neq 0$, however, is only possible for a broken inversion symmetry, since otherwise the Kramers degeneracy dictates $E(k, \uparrow) = E(k, \downarrow)$. Due to the presence of inversion symmetry in bulk Mg and W, the respective bulk Bloch states are not spin-split. However, overlayer states and QWS, which do not couple to substrate Bloch states and nevertheless have strong weight at the interface, experience inversion symmetry breaking and are subject to this effective magnetic field in the vicinity of the strong potential around the tungsten cores. In a field effect transistor the Rashba spin splitting can be tuned with an applied gate voltage, which leads to the concept of the spin transistor of Datta and Das[5]. On the other hand, the degree of wavefunction localization, which is, e.g., different for Mg surface states and QWS of different order, should affect the splitting as well and is therefore of fundamental interest for spintronic applications employing the Rashba effect.

9.2 Results

Thin Mg films have been grown on W(110) at room temperature. The photoemission results were obtained with hydrogen Ly_{α} radiation ($h\nu=10.2$ eV) and the sample was rotated with a motorized 2-axis goniometer stage [6]. Mg grows in a layer-by-layer fashion over a large thickness range and supports well-defined quantum well states [7]. All films exhibit a narrow thickness spread since the observed discrete energy levels evolve continuously up to large thicknesses (see Fig. 9.1a). Layer-resolved films would exhibit discrete static features associated with the specific number of layers present in the film. The energetic position of the quantum well states can be understood in the framework of the phase accumulation model [7]. This model expresses the condition for constructive interference in terms of phaseshifts within the film of thickness d and at the surface ($\phi_{surface}$) and interface boundary ($\phi_{interface}$). A stationary state requires the total phaseshift to be an integer times 2π , which naturally selects

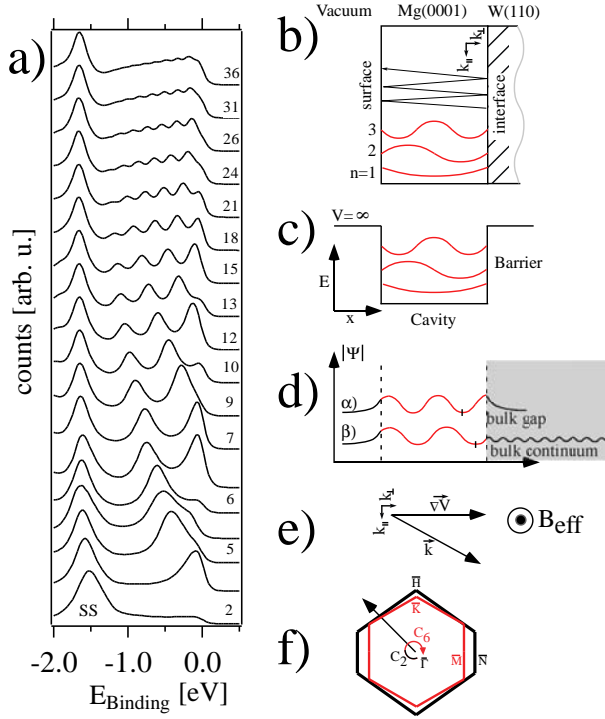


Figure 9.1: a) Quantum well states (QWS) as seen by ultraviolet (UV) photoemission (modified VG Escalab MkII with monochromatized hydrogen Ly_α ($h\nu=10.2$ eV) photon source) in normal emission geometry at $T=300$ K. States above the surface state (SS) energy at -1.7 eV are QWS. The film thickness for the spectra is given in units of unit cells (5.21 Å), comprising two atomic layers. b) Experimental cavity with surface and interface boundary and three cavity modes. An off-normal quantum well state, characterized by a wave vector component parallel to the surface, $k_{||}$, indicating a side-wards displacement. c) Ideal cavity with infinitely high walls. d) Difference between a confined quantum well state and a leaky quantum well resonance with a corresponding change in wavelength. e) Vectorial representation of the effective in-plane magnetic field, B_{eff} , at the Rashba interface. f) Brillouin zones with high symmetry points for the epitaxial relationship between the 6-fold symmetric (C_6) Mg(0001) thin film and the two-fold symmetric (C_2) W(110) substrate.

discrete k-vectors.

$$2 \cdot k \cdot d + \phi_{interface} + \phi_{surface} = n \cdot 2\pi \quad n \in integer. \quad (9.1)$$

These geometry enforced k-vectors correspond to energy values via the bulk band dispersion $E(k)$. For increasing well dimensions more states can be accommodated (Fig. 9.1) and the influence of the boundary conditions becomes less important, since the corresponding phase shifts are divided by the film thickness in order to obtain the allowed k-vector. A possible substrate influence on the cavity modes is therefore best detected for small cavities.

Mg grows epitaxially in [0001] direction with an in-plane orientation such that the $[11\bar{2}0]$ direction is aligned to the $[001]_{bcc}$ direction of the W substrate. This relation corresponds in reciprocal space to an alignment between the $\bar{\Gamma}$ \bar{M}_{hex} and $\bar{\Gamma}$ \bar{N}_{bcc} high symmetry directions of the respective Brillouin zones (see Fig.9.1f). The W(110) surface is a pseudo-hexagonal growth substrate [8, 9] but exhibits only a two-fold rotational axis. In this sense electronic overlayer states, which exhibit a reduction of symmetry from C_6 to C_2 reflect the influence of the reflectivity of the substrate[10]. Quite naturally such a substrate influence can be detected in a full hemispherical measurement as two-fold symmetric features.

In fact, the band dispersion of Mg is almost not affected by its weak hexagonal lattice potential and is almost free electron-like. Correspondingly, the k-resolved band structure is dominated by a parabolic dispersion relation with spheres as constant energy surfaces. The Γ MK plane of the Brillouin zone cuts the corresponding free electron parabolas in circles. The circular, isotropic in-plane dispersion relation is corroborated by *ab-initio* electronic structure calculations for a free-standing three unit cell thick Magnesium slab (see Fig. 9.2a). For this thickness the well-known Mg surface state (SS) is already apparent in the calculation and cuts the Fermi level in a ring-like fashion. In contrast to this, the experiment (Fig. 9.2b) displays clear deviations from this ideal behavior for a similarly small film thickness of ≈ 3 unit cells. The experimental film thickness supports already one ($n=1$) occupied quantum well state in addition to the aforementioned surface state. The Mg surface state is clearly not cutting the Fermi level isotropically, but instead a two-fold symmetry points directly to the substrate influence.

The surface state wavefunction probes the electronic structure of the underlying tungsten substrate and discontinuities are expected if the coupling regime

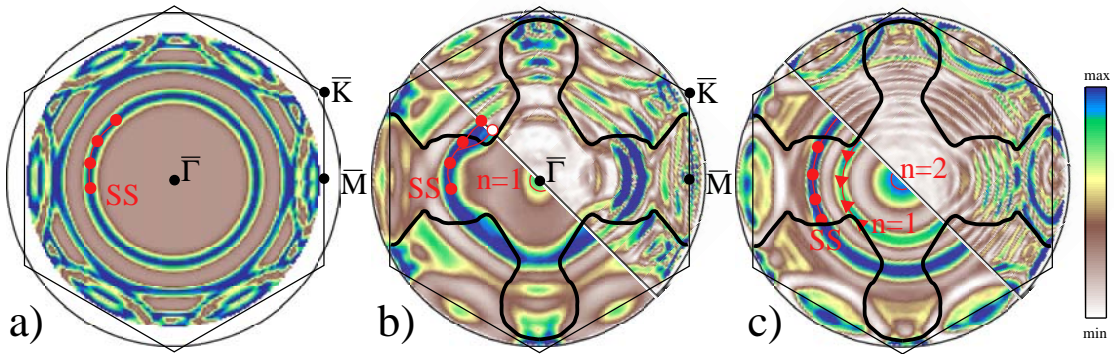


Figure 9.2: Fermi surface contours displayed as a function of k_{\parallel} . Marked is the hexagonal Mg Brillouin zone with high symmetry points $\bar{\Gamma}$, \bar{M} , \bar{K} ; SS labels free electron-like surface state and $n=1,2$ successive QWS; symbols are identical to the ones in Fig. 3. a) Theoretical Fermi surface for a 3 unit cell thick slab, obtained with the APW+lo code Wien2k [11]. b) and c) Experimental Fermi surface map for a three and eight unit cell thick film, respectively; experimental raw data are plotted in the lower part (i.e., below the 135° diagonal line) and asymmetry plots [12] in the upper part; the curved black line marks the border between the surface projected bulk states and surface projected bulk gap; it falls together with strong deviations from the circular symmetry, highlighted in the asymmetry plots (see upper part). The color bar (right side) indicates the intensity scale.

changes to the resonance case upon leaving the confining substrate band gap. These locations in k -space for the Fermi energy are indicated with thick black lines. If the gradient of deviations from isotropy is plotted [12] (upper part in Fig. 9.2b,c) one can clearly see that indeed the transition to the resonance case leads to discontinuities in the in-plane dispersion, which are especially pronounced at the band edges (drawn in black). If a similar measurement is inspected for a thicker, two quantum well state supporting film (Fig. 9.2c, with $n=2$), similar effects can be observed. However, in agreement to the phase accumulation model, the effects of the substrate are much weaker since the interface phase shift is less important for the total phase of a thicker film. Nevertheless, tracing the bulk band edges is still possible [13].

The electron reflection at the interface boundary might not only warp the one-electron band structure, it may have surprising effects on the spin structure as well. *Magnetic QWS on a ferromagnetic substrate* have already been reported [14]. However, for Mg on W(110) both, overlayer and substrate material are nonmagnetic, which points intuitively to spin-degeneracy. Nevertheless, it has recently been reported that the high atomic number (Z) material W(110) ($Z=74$) gives rise to a zero field, spin splitting of its surface state [15][16]. The Rashba effect [4] lifts the spin-degeneracy at the surface, where inversion symmetry is broken.

Fig. 9.3 shows a set of measurements obtained for increasing thicknesses, as it is reflected in the increasing number of QWS at $\bar{\Gamma}$ ($k_{\parallel}=0$). The scans were obtained for an azimuthal angle of 135° , which is indicated in Fig. 9.2b). Similarly as in the previously discussed Fermi surface measurements, we note the strong influence of substrate band edges on the energy dispersion. The surface state is perturbed in Fig. 9.3a) in regions close to the band edge labeled with one and two, due to coupling to specific bands. However, very striking is the appearance of additional bands (open symbols), which are split-off the original main quantum well peak and the surface state. The upper branch of the split surface state is clearly visible in Fig. 9.3a) (open and closed circles) and becomes more faint in Fig. 9.3b). The surface state splitting is only observed after the state is located in the substrate band gap and vanishes for higher thicknesses (Fig. 9.3c,d)).

The behavior of the QWS emission is similar except that it extends to higher thicknesses (triangles in Fig. 9.3a-d)) as expected, since the QWS travel across the entire film. The splitting is again only apparent in the substrate band gap.

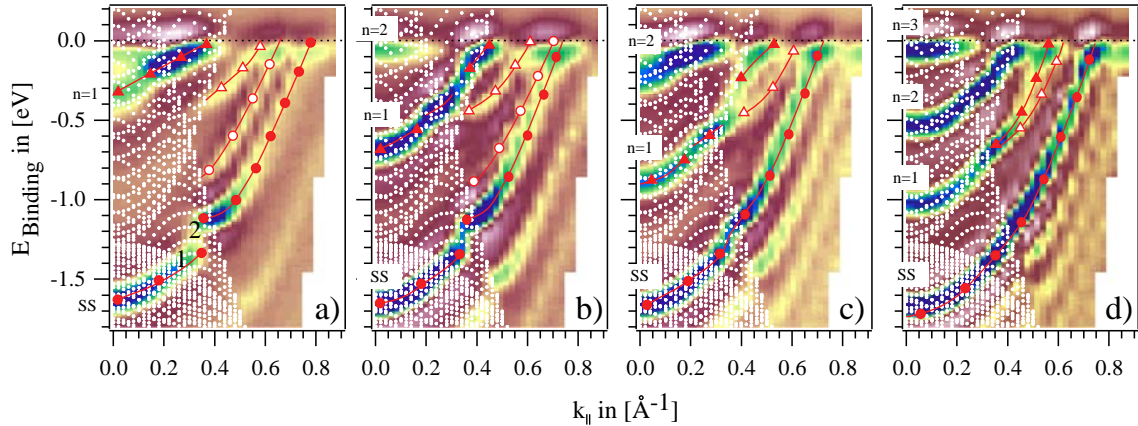


Figure 9.3: $E(k_{\parallel})$ dispersion plots for 4,6,8 and 11 unit cell thick films taken along the 135° diagonal line (Fig. 2) are displayed in a), b), c) and d), respectively. Consecutive QWS $n=1,2,3$ and the surface state (SS) are labeled. The second derivative of the measurements is shown to highlight the different features. The surface projected band structure of W(110) appears as an overlay of white dots. Empty and filled circles mark the surface state and its splitting; empty and filled triangles label the $n=1$ QWS and its splitting.

9.3 Discussion and Conclusion

The presented measurements bear interesting and important implications for one of the key parameters of the *particle in the box* model, namely the interfacial electron reflectivity. The leakage to the substrate is similarly low for both, truly confined quantum well states and partially confined quantum well resonances. This is probably due to unfavorable, symmetry-forbidden coupling between quantum well resonances and substrate states. Nevertheless, substrate band edges can be detected as perturbations in the in-plane dispersion. This demonstrates that the interfacial phase shift depends on the specific energy-, k -vector- and symmetry-dependent matching conditions. Present empirical models which compute the energy-dependent phase shift in terms of the distance to the band edge do not describe this system correctly. A scalar value for the interfacial phaseshift does not reproduce all properties of the involved matched wavefunctions.

Full hemispherical measurements, as shown here, are particularly advantageous for QWS spectroscopy on low symmetry substrates because a symmetry-breaking is directly observed in the measurements. Furthermore, the measure-

ments do not rely on the exact knowledge of the prepared thickness. This is especially important for not layer-resolved QWS.

The most important finding on the confined states is, however, the observed splitting. We would like to point out, that in contrast to Matsuda et al. for Ag/Si(001) [17], we observe a splitting primarily in gap regions of the substrate. Therefore, an explanation of the splitting as due to a partial confinement by the substrate continuum does not hold. Similarly a lattice mismatch between film and substrate [7] is not expected to yield discontinuities at substrate band edges. Instead, the high atomic mass of the W(110) substrate leads to relativistic effects expressed by the Rashba term. The lack of inversion symmetry across the interface or more appropriately the lack of inversion symmetry and a concomitant lifting of the Kramers degeneracy at the confining barrier leads to a spin-splitting. The effect is smaller or absent for states, which hybridize with substrate states. Hybridization implies loss of their surface (resp. interface) character and accumulation of bulk character with inversion symmetry (Fig. 1d)). On the other hand, only the potential of the tungsten nuclei gives rise to a sizeable spin splitting [18]. For this reason, the surface state is not spin split anymore for large thicknesses (Fig.3c,d). The surface state wavefunction decays exponentially towards the interface and therefore interface effects become less important for thick films. The magnitude of the observed splittings is with some hundred meV in the same range as the spin-orbit splitting of the W 5d band. The Rashba Hamiltonian predicts a vanishing spin splitting for $k_{\parallel}=0$ and an increase with increasing k_{\parallel} for a uniform gradient of the potential barrier. However in this case the barrier itself is profoundly k dependant and therefore simplified model calculations are not applicable. The position inside the gap of the projected W band structure might not only influence the size of the splitting, but might also be responsible for the observed intensity differences of the respective upper and lower branches.

The observation of such a spin splitting requires a heavy substrate with a large atomic spin-orbit splitting parameter (expressed by a strong potential gradient) (Fig. 1d),1e)), combined with inversion-symmetry breaking at the interface. These requirements might explain, why this relativistic effect has not been observed so far for quantum cavities. The presented data indicate, that a heteroepitaxially formed two-dimensional electron gas is subject to a spin-splitting due to the presence of an interface. The heteroepitaxial approach opens a completely new field for the study of differently deposited quantum wells.

The described system also bears a striking resemblance to spin-split final-state effects in photoemission, as they have been described by Kirschner et. al. [19]. They observed an inherent spin polarization of the photoemission signal due to the matching of the Bloch spinor wave function to the free electron spinor wave function of the outgoing photoelectron. In the present case the matching between the spin-orbit split spinor regime of the substrate and the free electron spinor regime of the quantum well cavity proceeds over the interface and appears to introduce a net spin-splitting as well.

The effects of a Rashba interface on QWS are crucial ingredient for spintronic devices, such as the spin transistor proposed by Datta and Das[5]. For this type of devices, the critical question is, how the change of carrier localization at the interface due to a gate voltage affects the channel spin separation. However, the present study indicates, that the spin splitting is inherently dependent on the detailed k-resolved electronic structure at the interface. Therefore a one-dimensional approximation of the involved materials bandstructures with essentially the upper band edge as parameter might not be sufficient for device design purposes. Instead a complete modelling of the interface electronic structure seems necessary to predict the k-resolved spin splitting. The bulk inversion-symmetry of both, Mg and W (in contrast to common semiconductors) opens up interesting new possibilities to study spin relaxation in these quantum well structures.

Last but not least, the discussed effect becomes only visible for $k_{\parallel} \neq 0$, therefore a splitting is not occurring in one-dimensional models. Hence, the effects of quantum confinement can be discussed in introductory quantum mechanics with the familiar particle in the box model without introducing the electron spin.

Acknowledgements We are greatly indebted to our workshop and electric engineering team. Financial support by the Fonds National Suisse pour la Recherche Scientifique is gratefully acknowledged. Valuable scientific discussions with P. Blaha are acknowledged.

Bibliography

- [1] J. Paggel, T. Miller, and T.-C. Chiang, *Science* **283**, 1709 (1999).
- [2] T.-C. Chiang, *Surf. Sci. Rep.* **39**, 181 (2000).
- [3] The wave vector vs wavelengths relation is given by $\lambda = \frac{2\pi}{|k|}$. The wave vector \vec{k} is decomposed into a component parallel to the film, (k_{\parallel}), and a component perpendicular to the film, (k_{\perp}). There is no lateral confinement for the film and k_{\parallel} is quasi-continuous. Due to reduced thickness, k_{\perp} is quantized. Each state is therefore characterized by the energy dispersion relation $E(k_{\perp\text{quantized}}, k_{\parallel})$.
- [4] E. Rashba, *Fiz. Tverd. Tela* **2**, 1109 (1960).
- [5] B. Datta and S. Das, *Appl. Phys. Lett.* **56**, 665 (1990).
- [6] P. Aebi, J. Osterwalder, P. Schwaller, L. Schlapbach, M. Shimoda, T. Mochiku, and K. Kadowaki, *Phys. Rev. Lett.* **72**, 2757 (1994).
- [7] F. Schiller, M. Heber, V. Servedio, and C. Laubschat, *Phys. Rev. B* **70**, 125106 (2004).
- [8] J. Hayoz, S. Sarbach, T. Pillo, E. Boschung, D. Naumovic, P. Aebi, and L. Schlapbach, *Phys. Rev. B* **58**, R4270 (1998).
- [9] L. A. Bruce and H. Jaegger, *Philos. Mag. A* **38**, 223 (1978).
- [10] A structural deformation of the film due to stress/strain can be excluded on the basis of Low Energy Electron Diffraction (LEED) and X-Ray Photoelectron Diffraction (XPD) measurements, which are not presented here.
- [11] P. Blaha, K. Schwarz, , G. Madsen, D. Kvasnicka, and J. Luitz (2001), *wien2k, An Augmented Plane Wave + Local Orbitals Program for Calculating Crystal Properties* (Karlheinz Schwarz, Tech. Univ. Wien, Austria) ISBN 3-9501031-1-2.
- [12] The anisotropy plot has been obtained from the measured data by subtracting and normalizing to the circular average and plotting the gradient.
- [13] L. Aballe, C. Rogero, P. Kratzer, S. Gokhale, and K. Horn, *Phys. Rev. Lett.* **87**, 156801 (2001).

-
- [14] J. E. Ortega, F. J. Himpsel, G. J. Mankey, and R. F. Willis, Phys. Rev. B **47**, 1540 (1993).
 - [15] E. Rotenberg, J. Chung, and S. Kevan, Phys. Rev. Lett. **82**, 4066 (1999).
 - [16] M. Hochstrasser, J. Tobin, E. Rotenberg, and S. Kevan, Phys. Rev. Lett. **89**, 216802 (2002).
 - [17] I. Matsuda, T. Ohta, and H. Yeom, Phys. Rev. B **65**, 085327 (2002).
 - [18] L. Petersen and P. Hedegård, Surf. Science **459**, 49 (2000).
 - [19] J. Kirschner, R. Feder, and J. Wendelken, Phys. Rev. Lett. **47**, 614 (1981).

Part IV
Appendix

Chapter 10

Growth of thin Bi films on W(110)

C. Koitzsch¹, M. Bovet¹, F. Clerc¹, D. Naumović¹, L. Schlapbach¹ and P. Aebi¹

¹*Département de Physique, Université de Fribourg, Pérolles, CH-1700 Fribourg, Switzerland*

Surf. Sci. 527 (2003) 51-56

Abstract: We report on the growth of single crystalline epitaxial Bi films on W(110). X-ray photoelectron diffraction (XPD) and low energy electron diffraction (LEED) reveal that Bi grows well ordered in the pseudocubic (001) orientation. The two-fold symmetric W(110) surface supports four different Bi(001) domains. The multi-domain nature is unambiguously detected via LEED showing a peculiar splitting of spots. It is shown that a preferential domain alignment along the $[001]_{tungsten}$ direction accounts for this observation and is in agreement with a two-fold XPD pattern.

10.1 Introduction

Bismuth is a semimetal of the group V in the periodic table of elements with an atomic electron configuration of $[Xe]4f^{14}5d^{10}6s^26p^3$. It re-attracted considerable interest in the last years due to three effects. The discovery of superconductivity in small granular clusters [1] despite the non-superconducting properties for bulk Bi opened the question of the surface electronic structure being responsible for the superconducting state. Secondly, the electronic properties of Bi make it almost an ideal candidate to study quantization phenomena, the Fermi wave vector with experimentally convenient dimensions of the order several nm. Quantum size effects should render thin films insulating due to a thickness induced quantization of the valence band [2] and a subsequent lifting of the overlap between electron and hole bands at E_F . Furthermore the large $Z=83$ should give rise to a considerable effect of the spin-orbit interaction on the valence band structure, namely the p-bands and surface localized states in the vicinity of the Fermi level[3][4][5].

In this work we report on the growth of thin Bi films on W(110). To our knowledge, this is the first time, that Bi growth on this substrate is reported. Tungsten was chosen as a substrate since it is a refractory metal, and hence does not alloy with Bi. Furthermore its large band gaps [6] of the projected bulk band structure in certain regions of the surface Brillouin zone make it a suitable substrate for studies of ultra thin films because a clear separation between substrate and film valence states is feasible. The present study shows that well ordered single crystalline films can be obtained via room temperature growth on W(110). It is demonstrated that these films grow in a multi-domain fashion in the pseudocubic [100]-orientation.

10.2 Experimental Details

The preparation of clean W(110) surfaces has already been described elsewhere[7]. The crucial step in order to deplete the crystal from C was a 125 h anneal at 1500 K under an oxygen partial pressure of 10^{-7} mbar. Subsequently an unreconstructed surface, free of surface contaminants can be obtained by flashing the crystal via e-beam heating up to 2500 K in ultra high vacuum. Bi was deposited at room temperature out of a water cooled home built evaporator at a rate of approximately $2\text{\AA}/\text{min}$, as measured by an oscillating quartz crystal. The pressure during deposition did not exceed $2\cdot 10^{-10}$ mbar. The crystal

structure was monitored by low energy electron diffraction (LEED), snapshots of the diffraction pattern were made with an 8-bit CCD camera.

The photoemission experiments were performed *in-situ* in a modified VG Mk II spectrometer equipped with a two-axis sample goniometer enabling sequential computer-controlled sample rotation [8][9]. For X-ray photoelectron diffraction (XPD) a twin anode was used delivering Mg-K α radiation ($h\nu=1253.6$ eV). The angular resolution was 1° full cone acceptance. It has been shown that full hemispherical XPD patterns (diffractograms) provide very direct information about the near surface structure. It's chemical sensitivity and the sensitivity to local order render it a powerful method for structural investigations [10]. At electron energies above 500 eV, the anisotropic scattering of photoelectrons by the ion cores leads to a forward focusing of electron flux along the emitter-scatterer axis. Prominent intensity maxima in diffractograms can often be immediately identified with near-neighbour directions. The chemical sensitivity arises from diffractograms of different core levels, allowing for the determination of local order around specific atomic species, for a review on XPD see [11]. Here XPD patterns from W and Bi 4f core levels are shown. The obtained angular distributions of intensities, projected stereographically, are plotted in a linear grey scale image.

Furthermore we present simulations of the aforementioned XPD pattern. These simulations are based on model clusters (see below), where for every constituent atom the corresponding forward focusing maxima arising from the surrounding atom ensemble are calculated. For a given example atom, intensity maxima are found in direct line of sight between the example atom, which can be viewed as emitter and the surrounding atoms, which are the scatterers. The dot-size for each forward focusing event is inversely proportional to the distance between emitter and scatterer.

10.3 Results and discussion

Since crystal growth is the main focus of the present paper a short insight into the lattice properties of bulk Bi is given. Bismuth has a reported bulk lattice constant of 4.75 Å. The crystal structure is rhombohedral with space group 166. This rhombohedral lattice can be understood as distorted cubic [12]. A rhombohedral unit cell with a shear angle of 60° and a two atom basis, where the second basis atom is centered can equally be described with a simple cubic lattice. Fig. 10.1(a) shows this relationship, while in Fig. 10.1(b) a (110)-plane

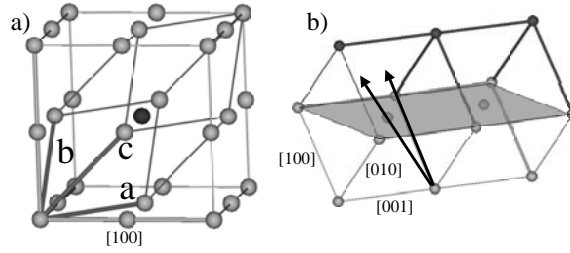


Figure 10.1: (a) Simple cubic lattice with rhombohedral unit cell inscribed, the second basis atom is shaded in black, the pseudo-cubic unit cell vectors are along the cube edges, the [100] growth direction is indicated. (b) Cut through a bcc tungsten unit cell, the (110) surface is shaded, principal forward focusing directions from one emitter atom are indicated by arrows. (see text)

of the tungsten crystal is depicted. For the present case of Bi, the shear angle is 57.35° and the basis atom positions are $(0,0,0)$ and $(0.474, 0.474, 0.474)$. This introduces small distortions, resulting for the (001) surface in a rectangular surface unit cell with the two unit cell vectors not equal and a two-atom basis [5]. The resulting lattice is called pseudocubic. In the following we will refer to the crystallographic directions in pseudocubic coordinates.

In Fig. 10.2 two LEED pictures are shown, which illustrate the changes, when thin bismuth films are deposited. The principal crystallographic directions for W(110) are indicated in (a) and the orientation of the W(110) crystal below the Bi film in (b) is identical.

Based on LEED, we can already derive the orientational relationship between the reciprocal lattices of substrate and film. The surface unit cell of bismuth films, indicated in Fig. 10.2(b), appears oriented approximately 45° off with respect to the W(110) surface unit cell (Fig. 10.2(a)). The lengths of the reciprocal unit cell vectors (Fig. 10.2(a)) yield the expected real space bulk values for W(110), which has a lattice constant of 3.165 \AA [13]. For the Bi film (Fig. 10.2(b)) a pseudo-cubic surface unit cell is obtained, which suggests a (001)-orientation. This symmetry excludes immediately the [111]-direction, since the [111]-direction is a trigonal axis. This is a somewhat surprising result, since a variety of other metals deposited on W(110) grow along the [111]-direction [14][15]. The length of the reciprocal unit cell vectors (Fig. 10.2(b)) translates into a rectangular real space unit cell with a length of $4.3 \pm 0.3 \text{ \AA}$ and $4.6 \pm 0.3 \text{ \AA}$. This is to be compared to Bi bulk values of 4.53 \AA and 4.75 \AA [13].

A peculiar doubling of spots (circled in Fig. 10.2(b)) appears for all ob-

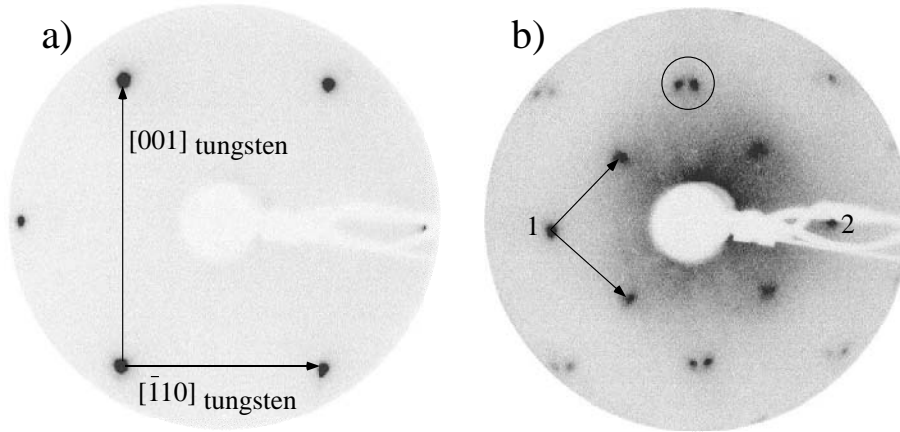


Figure 10.2: LEED pictures, $E_{Beam} = 61.3eV$, for (a) clean W(110), (b) a nominal Bi coverage of 70\AA .

served spots except the ones lying on a horizontal line across the center of the image. The diffraction spots without splitting are marked with numbers 1 and 2 in Fig. 10.2(b). In order to understand the origin of the observed spot splitting, the reciprocal surface lattice for the suggested (001) orientation was calculated and is shown in Fig. 10.3(a) with black dots. Additionally in Fig. 10.3(a) the same reciprocal lattice is shown but after a mirror operation (open circles in Fig. 10.3(a)) as explained below. The field of view, as indicated by the shaded circle is adapted to the experimental LEED geometry and the region, where no spot splitting occurs is marked by a black dotted line. Already one notices a very good agreement between the experimental LEED pattern and the combined pattern of the two reciprocal surface nets (black and open circles in Fig. 10.3(a)). The two reciprocal lattices are interrelated by mirror symmetry with mirror axis either the $[\bar{1}10]_{tungsten}$ or $[001]_{tungsten}$ -direction. The reason why only some spots appear split, is the alignment of the reciprocal unit cell diagonal along the $[\bar{1}10]_{tungsten}$ -direction. The $[\bar{1}10]_{tungsten}$ -direction is the alignment axis for the reciprocal unit cell diagonal and they both are found on the black dotted line in Fig. 10.3(a). All spots, which can be found on this alignment axis, will not appear split, for a mirror axis, which is either the alignment axis itself or an axis oriented perpendicular to the alignment axis (grey line in Fig. 10.3(a)). The observed LEED pattern therefore supports the existence of mirror domains, which are related to the original domain (black circles in Fig. 10.3(a)) via the $[\bar{1}10]_{tungsten}$ or $[001]_{tungsten}$ mirror axis.

Fig. 10.3(b) shows the corresponding real space atom ensemble, the topmost Bi layer is shown in black dots, a second layer deeper in the bulk is shown in grey dots. The crystal is aligned such that the corresponding reciprocal net is aligned in the aforementioned manner. One immediately notices that in real space the unit cell diagonal is aligned along the $[001]_{tungsten}$ direction (grey line in Fig. 10.3(b)), exactly perpendicular to the alignment direction in reciprocal space. The observed LEED pattern has to be therefore interpreted, such that the $[001]_{tungsten}$ is the principal alignment axis with the formation of atom rows as shown in Fig. 10.3(b) along this direction.

The formation of atom rows along the $[001]_{tungsten}$ -direction could suggest a particularly good match between substrate and film along this direction. Indeed it is comparable to the lattice matching for $[111]$ -oriented metals, which usually grow in the Nishiyama-Wassermann relation[16] on W(110). In this epitaxial relation one has an alignment between the $[001]_{tungsten}$ -direction and the hexagonal $[2\bar{1}10]$ direction with a possible supercell commensuration in this direction. Apparently for the case of Bi an arrangement in $[001]$ direction offers an advantage in terms of lattice match, one obtains based on the Bi bulk crystal structure a lattice misfit of only 3.6% in the $[001]_{tungsten}$ direction.

Fig. 10.3(c) shows a more global view of the crystallographic arrangement of a Bi cluster oriented in the aforementioned manner in (a) sideview and (b) top view. Note the formation of atom rows, which have a small tilt away from the $[100]$ surface normal (see below). This tilt is especially apparent in Fig. 10.3(c) as an opening angle between the $[001]$ direction (surface normal) and the atomic row right beside it.

The real space crystallographic structure can be determined by XPD. Here, additionally, the out-of-plane structure is accessible. We measured the angular dependence of the photoelectron signal for W and Bi 4f core level emission. The corresponding emission patterns in stereographic projection, are shown in Fig. 10.4 (a,b). For W(110) (Fig. 10.4(a)) we notice a two-fold symmetry with the strongest emission maxima at polar angles of 35° and 45° . Their relationship to the real space structure becomes obvious if emission from a sub-surface site (Fig. 10.1(b)), is considered. Here, forward focusing from this emission site due to scattering at the very surface layer is expected for polar angles with respect to the $[110]$ surface normal of 45° in $[100]$ -direction and 35° in $[111]$ -direction. All resulting forward focusing maxima, based on a cluster are shown as an overlay in the lower half of the W 4f emission pattern. Note, that densely packed crystallographic planes appear as high intensity bands, known

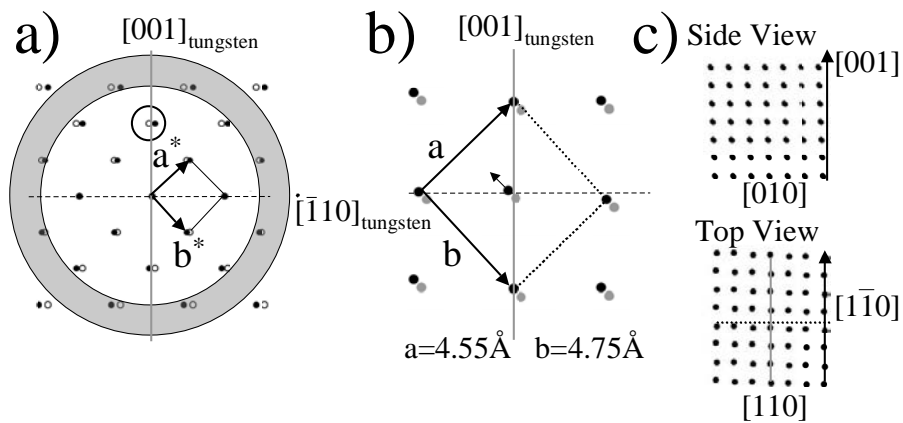


Figure 10.3: (a) reciprocal Bi(001) surface net shown in black dots, mirror domain shown in open circles; the circle illustrates the field of view for the LEED experiments; reciprocal unit cell vectors are denoted as a^* and b^* . (b) Real space surface net drawn in black dots; shown in grey is a buried Bi layer illustrating the pseudo-cubic stacking; the second basis atom (marked by an arrow) is shifted away from the center. (c) Global view on the resulting cluster; the top view shows the alignment to the $[001]_{\text{tungsten}}$ direction and the sideview illustrates the formation of atomic rows, which are tilted away from the surface normal.

as Kikuchi bands [17]. In a stereographic projection planes appear as circular segments or straight lines for the ones containing the sample normal.

Regarding the *a priori* unknown crystalline orientation of the Bi film one has to rely on already known crystal structure data and the symmetry of the pattern (Fig. 10.4b) in order to simulate the experimental situation. The pattern is nearly fourfold symmetric, with slightly differently shaped straight (circled features in Fig. 10.4b numbered one and two) Kikuchi bands along the $[001]_{tungsten}$ and $[\bar{1}10]_{tungsten}$ direction, rendering it two-fold symmetric. Primary forward-focusing peaks are marked by a circle in Fig. 10.4(b) and labeled with numbers three and four. In order to facilitate a more in-depth understanding of the diffractogram, forward focusing directions based on a (001) oriented pseudo-cubic Bi cluster (Fig. 10.3(c)) were determined. The calculation bases on a cluster which is rotated such that the real space unit cell diagonal (Fig. 10.3b) is aligned to the $[001]_{tungsten}$ direction, in accordance with the LEED spot splitting.

The resulting forward focusing directions (overlay in Fig. 10.4(b)) are in very good agreement with the experimental pattern, which in general confirms the [100] growth direction. Nevertheless the calculated pattern is not two-fold symmetric, a fact which is easily seen for forward focusing around the surface normal. In this region the calculation yields two features, which render the diffractogram one-fold symmetric. The reason for this low symmetry is the crystal structure of Bi itself (Fig. 10.3(c)). The pseudo-cubic nature of Bi leads to atom rows slightly tilted away from the pseudo-cubic [100]-direction, which is the wobble away from the surface normal (Fig. 10.3c). The two-fold symmetry must then originate from different domains, an assumption which has already been used to explain the LEED spot splitting. Fig. 10.4(c) shows again the stereographic projection of forward focusing directions, but in addition the results from mirror clusters. Now the two-fold symmetry is nicely reproduced, the stronger Kikuchi line along $[001]_{tungsten}$ is clearly visible (circled features in Fig. 10.4(c)), again confirming the multi-domain nature of Bi films on W(110)

10.4 Conclusions

It has been shown that the combination of LEED and XPD allows for an in-depth determination of the crystal structure of Bi thin films on W(110). Four different growth domains, along with a diagonal alignment of the Bi surface unit cell parallel to $[001]_{Tungsten}$ direction, explains both the doubling of LEED

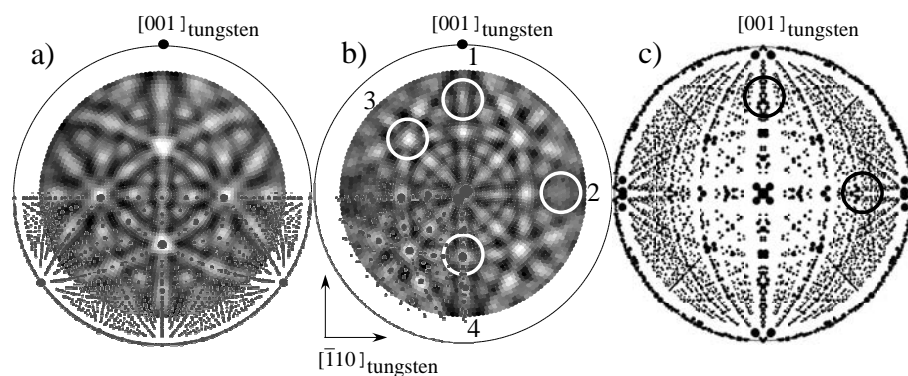


Figure 10.4: Mg $K\alpha$ excited XPD, the center corresponds to normal emission, while the outer circle corresponds to an emission angle of 90° with respect to the surface normal. The diffractograms are plotted in a linear grey scale with high intensity shown in white (a). Diffractogram from the clean W(110) substrate showing the angular dependence of the W 4f level $E_{kinetic}=1222$ eV and the result of a cluster calculation as overlay. (b) Bi 4f diffractogram, $E_{kinetic}=1097$ eV, and forward focusing direction for one domain as overlay; circled regions one and two render the XPD pattern twofold symmetric, circled regions three and four are primary forward focusing peaks centered at polar angles of 56.2° (feature three) and 45.8° (feature four). The observed forward focusing peaks are within the experimental error at their theoretical position of 56.4° and 45° . (c) Forward focusing directions based on a pseudo-cubic cluster and three mirror domains

spots and the two-fold symmetry of the XPD pattern. The obtained good crystalline quality of the films on W(110) render subsequent investigations of e.g. quantum size effects, spin-orbit coupling etc. with various techniques very promising.

Acknowledgements We are greatly indebted to our workshop and electric engineering team. Financial support by the Fonds National Suisse pour la Recherche Scientifique is gratefully acknowledged.

Bibliography

- [1] B. Weitzel and H. Micklitz. *Phys. Rev. Lett.*, 66:385, 1991.
- [2] V. de Renzi, M. G., Betti, and C. Mariani. *Phys. Rev. B*, 48:4467, 1993.
- [3] M. Hengsberger, P. Segovia, M. Garnier, D. Purdie, and Y. Baer. *Eur. Phys. J. B*, 17:603, 2000.
- [4] C. R. Ast and H. Hoehst. *Phys. Rev. Lett.*, 87:177602, 2001.
- [5] S. Agergaard, C. Sondergaard, H. Li, M. B. Nielsen, S.V. Hoffmann, Z. Li, and Ph. Hofmann. *New J. of Phys.*, 3:15.1., 2001.
- [6] A.M. Shikin, D.V. Vyalikh, G. V. Prudnikova, and V.K. Adamchuk. *Surf. Sci.*, 487:135, 2001.
- [7] J. Hayoz, Th. Pillo, A. Zuettel, S. Guthrie, P. Aebi, and L. Schlapbach. *J. of Vac. Sci. Techn. A*, 18:2417, 2000.
- [8] J. Osterwalder, T. Greber, A. Stuck, and L. Schlapbach. *Phys. Rev. B*, 44:13764, 1991.
- [9] D. Naumović, A. Stuck, T. Greber, J. Osterwalder, and L. Schlapbach. *Phys. Rev. B*, 47:7462, 1993.
- [10] Th. Pillo, J. Hayoz, P. Schwaller, H. Berger, P. Aebi, and L. Schlapbach. *Appl. Phys. Lett.*, 75:1550, 1999.
- [11] C.S. Fadley. *Synchrotron Radiation Research: Advances in Surface Science*, volume 1. Plenum, New York, 1990.
- [12] F. Jona. *Surf. Sci.*, 8:57, 1967.
- [13] Pearson. *Pearson's Handbook of Crystallographic Data for Intermetallic Phases*. American Society for Metals, Metals Park, OH 44073, 3000.
- [14] J. Hayoz, S. Sarbach, E. Boschung, D. Naumović, P. Aebi, and L. Schlapbach. *Phys. Rev. B*, 58:R4270, 1998. e.g. YH_x .
- [15] A. M. Shikin, D. V. Vyalikh, Yu. S. Dedkov, G. V. Prudnikova, V. K. Adamchuk, E. Weschke, and G. Kaindl. *Phys. Rev. B*, 62:R2303, 2000. e.g. Au and Ag.

- [16] E. Bauer. *Appl. Surf. Sci.*, 11/12:479, 1982.
- [17] R. Trehan, J. Osterwalder, and C.S. Fadley. *J. of Electr. Spectr. and Rel. Phenomena*, 42:187, 1987.

Danksagung

Diese Doktorarbeit wurde in der Elektronen Spectroskopie Gruppe von Prof. Philipp Aebi an der Universität Neuchâtel und der Festkörperphysik Gruppe (FK) von Prof. Louis Schlapbach an der Universität Fribourg ausgeführt.

An erster Stelle bedanke ich mich bei Prof. Philipp Aebi für seine immer währende Unterstützung und offene Art mit der er meine Arbeit begleitet hat. Seine professionelle Detailgenauigkeit etwa bei der Analyse von Messergebnissen sind für mich beispielgebend. Meinen Kollegen in der Gruppe Corsin Battaglia, Marc Bovet, Florian Clerc, Laurent Despont, Gunnar Garnier und Oliver Gallus danke ich für ihren Teamspirit und diverse Segel Törns - let's keep in touch!

Der Standardsatz eines jeden Vortrages "This work is a group effort" wird auch bei der Verteidigung dieser Arbeit nicht fehlen. Auch meine Arbeit hat sehr von der Vorarbeit meiner Vorgänger profitiert. An dieser Stelle danke ich besonders Joseph Hayoz (all this hydride stuff), Oliver Gröening (für die diversen Oli.test Programme), Roman Fasel (XPD-Plot, Wien-Plot und AutoSSC) und Thorsten Pillo (Know-How ARPES) sowie Dusanka Naumovic.

Speziell gilt mein Dank den Fribourgern Michael Biemann (als Kollege und vor allem guter Freund), Pascal Ruffieux und Christoph Nützenadel (Euch auch für das Warten bei den Skitouren).

Während der Dissertation hatte ich das Vergnügen und die Herausforderung beim Bau einer Plasmakammer meine kreativen Vorstellungen mit der professionellen Werkstatt Equipe in Fribourg in rostfreien Stahl umsetzen zu können. Oswald Raetzo, Elmar Moser, Roger Vonlanthen und Roland Schmid nochmals herzlichen Dank für die Geduld beim Lesen kryptischer CAD Zeichnungen aus denen Ihr diese vielen super-dringenden Teile für mich gebaut habt.

Danke auch an viele Freunde, die diese Zeit mitbegleitet haben. Stellvertretend seien hier Rene Rauch, Michi Vogt, Christian Hirte, Daniel Nettels und Lars Nilsson genannt.

Trotz und wegen des Wintersports haben mich meine Schwester Daniela und mein Cousin Florian häufig besucht, auch in Zürich werdet ihr immer willkom-

men sein.

Der Versuch die Unterstützung meiner Eltern an dieser Stelle entsprechend zu würdigen ist aussichtslos. Viele Jahre war ich mir gar nicht bewusst, dass der eigene Weg teilweise auch von den Eltern mitgepflastert wurde und somit gangbar war. Trotz teils grosser räumlicher Entfernung seid Ihr mir stets zur Seite gestanden und sind wir uns nah.

Annaleta, Du bist ein Teil meines Lebens und hast die Zeit meiner Promotion wahrhaftig geprägt.

Curriculum vitae

Personal details

Family name	Koitzsch
First name	Christian
Date of birth	June 27, 1975
Place of birth	Eisenhüttenstadt, Germany
Nationality	German
Status	Single

Education

1991 - 1994	High School, Städtisches Gymnasium, Bad Salzungen Degree: Abitur
1994 - 1997	Studies of Electrical Engineering, Technische Universität Ilmenau, Germany
1998 - 1999	Studies of Physics, North Carolina State University Raleigh, USA
2000	Degree as Dipl. Ing. in Electrical Engineering: “Waferbonding of Sic Surfaces for electronic applications” under the direction of Prof. Dr. Knedlik, TU Ilmenau, Germany
2000- 2002	Graduate student in the Solid State Physics Group of Prof. Dr. Louis Schlapbach, University of Fribourg, Switzerland
2002- 2004	Graduate student in the Solid State Physics Group of Prof. Dr. Philipp Aebi, University of Neuchâtel, Switzerland

